Reduced-Complexity RF Chain and Antenna Designs for Massive MIMO Transmitters

by

Ferhad Kasem

A thesis submitted in partial fulfillment of the requirements for the degree of
Doctor of Philosophy

in

Electromagnetics and Microwaves

Department of Electrical and Computer Engineering

University of Alberta

Abstract

The amount of mobile data handled by wireless broadband cellular networks is increasing explosively. Multiple-input multiple-output (MIMO) systems have gained a significant importance in modern wireless communication systems. MIMO offers many dimensional advantages that can be utilized to boost capacity and coverage without utilizing more bandwidth or transmit power. The introduction of MIMO systems with large antenna arrays (also known as massive MIMO) and the use of millimeter wave (mmWave) frequency bands are considered some of the key enabling technologies in the 5^{th} generation of cellular systems to satisfy high data rate demands. However, when it comes to hardware implementation, massive MIMO systems with a large number of antennas face some challenges. Each antenna element is driven by a dedicated RF-chain; therefore, the RF-cost increases with the number of antennas. Each RF chain in a MIMO transmitter includes a power amplifier (PA), a mixer and a digital-to-analog converter (DAC). These components are expensive and power-consuming. Consequently, the cost will increase if the number of antennas grows.

Reduced-cost MIMO systems have been drawing attention lately. In this dissertation, the hardware of a reduced-complexity and cost MIMO transmitter utilizing a single RF chain is presented. The RF chain includes a linear, low-cost, and energy-efficient PA and without the need for a mixer or DAC. This MIMO transmitter can convert digital signals in the baseband to the RF domain. In this MIMO transmitter, antennas are fed by two-port networks

called load modulators. Load modulators are diode-based RF circuits that generate the desired outputs. The MIMO transmitter is designed at 3 GHz. The MIMO transmitter is capable of generating 64-QAM constellations at its output ports. This MIMO transmitter is perfectly suitable to operate with current MIMO receivers.

Preface

This thesis contains content that appears in the following publications. In Chapter 3, the design of a 64-QAM I/Q modulator based on load modulation has been presented. The modulator is designed to operate at 3 GHz. The 64-QAM load modulator has been realized using microstrip lines and a diode-based switching circuit. It is demonstrated that this modulator can be integrated into the MIMO system's transmitter, eliminating the need for a dedicated RF chain per antenna and making it ideal for alleviating the hardware complexity challenges associated with massive MIMO systems. The content of Chapter 3 has been published in the following journal paper:

- F. Kasem, R. Winter, R. Feghhi, K. Rambabu and W. A. Krzymień, "Design of a Low-Cost Low-Profile Energy Efficient 64-QAM Load Modulator," in *IEEE Transactions on Microwave Theory and Techniques*, vol. 70, no. 4, pp. 2246-2257, April 2022.

In Chapter 4, the design of a four-branch, reduced-complexity, load-modulated MIMO transmitter is presented. Each branch can independently generate and transmit 64-QAM symbols at its output by changing the physical length of the stubs in the load modulators connected to the antennas. A single RF chain drives the four branches instead of four dedicated RF chains, bringing substantial savings in cost, complexity, and energy consumption. The proposed load modulated approach can be expanded straightforwardly to a more significant number of branches making it promising to adopt in 5G massive MIMO transmitting arrays. The content of Chapter 4 has been submitted to IEEE Transactions on Circuits and Systems II: Express Briefs.

- F. Kasem, A. K. Iyer, K. Rambabu and W. A. Krzymień, "A Reduced-

Complexity Load-Modulated MIMO Transmitter Readily Scalable in 5G Massive MIMO Transmitters," (under review).

Acknowledgements

First and foremost, I would like to express my deepest gratitude to my supervisors, Prof. Rambabu Karumudi and Prof. Witold Krzymień. Their patience, encouragement, and immense knowledge were key motivations throughout my PhD. I have been extremely lucky to have supervisors who cared so much about my work. Their immense knowledge and ongoing guidance helped me tremendously. The truth is that this work could not have been done without their support on both the technical and personal levels.

I would also like to thank the members of my candidacy examination committee Prof. Ashwin Iyer, Prof. Kambiz Moez, and Prof. Masoud Ardakani for their insightful feedback.

I would also like to express my thanks to my close friend and lab mate, Dr. Rouhollah Feghhi. Our discussions and his immense knowledge in hardware and implementation were essential during my PhD journey.

I would like to express my gratitude for the financial support that I received from the Natural Sciences and Engineering Research Council (NSERC) of Canada and from TELUS Communications.

Finally, I would like to thank my family for their wise counsel and sympathetic ear. You are always there for me. I could not have completed this dissertation without your support.

Table of Contents

List of Tables

List of Figures

List of Acronyms

1G First Generation

2G Second Generation

3G Third Generation

4G Fourth Generation

5G Fifth Generation

ADC Analog-to-Digital Converter

ADS Advanced Design System

AMPS Advanced Mobile Phone System

AWGN Additive White Gaussian Noise

BPSK Binary Phase-Shift Keying

BS Base Station

CDMA Code Division Multiple Access

CSI Channel State Information

DAC Digital-to-Analog Converter

DC Direct Current

DEA Differential Evolution Algorithm

DoF Degrees of Freedom

EDGE Enhanced Data Rates for GSM Evolution

eMBB Enhanced Mobile Broadband

ESPAR Electronically Steerable Passive Array Radiator

EVM Error Vector Magnitude

FAP Femto Access Point

FDD Frequency-Division Duplex

FSPL Free Space Path Loss

GA Genetic Algorithm

Gbps Giga bit per second

GHz Giga Hertz

GPRS General Packet Radio Service

GSM Global System for Mobile Communication

HD High Definition

HSPA High-Speed Packet Access

HSPA+ evolved HSPA

HSDPA High-Speed Downlink Packet Access

HSUPA High-Speed Uplink Packet Access

ICT Information and Communication Technologies

IFFT Inverse Fast Fourier Transform

IMT International Mobile Telecommunications

IoT Internet of Things

IP3 Third-Order Intercept Point

ITU International Telecommunication Union

ITU-R ITU Radio-Communication

Kbps Kilo bit per second

KHz Kilo Hertz

LM Load Modulator

LMSRF Load-Modulated Single-RF

LO Local Oscillator

LOS Line of Sight

LTE Long-Term Evolution

LTE-A LTE Advanced

LUT Lookup Table

MHz Mega Hertz

MIMO Multiple-Input Multiple-Output

MMS Multimedia Messaging Service

MMSE Minimum Mean Square Error

mMTC Massive Machine-Type Communications

mmWave Millimeter Wave

MU-MIMO Multi-User MIMO

NMT Nordic Mobile Telephone

NR New Radio

NTT Nippon Telegraph and Telephone

OBO Output Back-OFF

OFDM Orthogonal Frequency Division Multiplexing

PA Power Amplifier

PAPR Peak-to-Average Power Ratio

PC Pilot Contamination

PCB Printed-Circuit Board

QAM Quadrature Amplitude Modulation

QPSK Quadrature Phase Shift Keying

RF Radio Frequency

RMS Root Mean Square

SINR Signal-to-Interference-plus-Noise Ratio

SIR Signal-to-Interference Ratio

SMS Short Message Service

SNR Signal-to-Noise Ratio

SU-MIMO Single-User MIMO

TDD Time-Division Duplex

TD-SCDMA Time-Division-Duplex Synchronous CDMA

UE User Equipment

UMTS Universal Mobile Telecommunications System

URLLC Ultra-Reliable and Low Latency Communications

VNA Vector Network Analyzer

VSWR Voltage Standing Wave Ratio

W-CDMA Wideband Code Division Multiple Access

WPD Wilkinson Power Divider

ZF Zero Force

Chapter 1

Introduction

Mobile broadband services are currently experiencing a period of rapid growth. The growing number of smart phones and other handheld devices has led to an explosion in mobile data demand in the last decade. According to a mobility report released by Ericsson [1], the global mobile data traffic reached around 33 exabytes per month by the end of 2019, with expectations to reach 164 exabytes per month in 2025. This massive mobile data traffic puts pressure on the wireless network operators to deliver increased coverage, capacity, and throughput to the end users. A technology shift in the design of the cellular network, both in hardware and software, is needed to respond to these ever-increasing demands.

Wireless communication technology has evolved over several decades. The timeline from the first generation of mobile networks, 1G, to the most recent one, the 5G, took over 40 years since the introduction of wireless cellular technology [2]. To give a historical background, the first generation (1G) systems employing analog transmission were introduced in a few countries worldwide in the 1980s, and they were limited to voice service. Several incompatible 1G cellular system standards were introduced in different countries, beginning with the NTT system in 1979 in Japan and followed by the NMT (Nordic Mobile Telephone) system in 1981 in Nordic countries. In North America the AMPS (Advanced Mobile Phone System) was introduced in 1983.

The second generation (2G) cellular systems employing digital transmission gained much more popularity and played a critical role in the evolution of mobile technology from the 1990s to early 2000. The most wide-spread worldwide among 2G systems became the Global System for Mobile Communication (GSM) standard. GSM enabled data transfer on top of voice communication by introducing new forms of communications represented by the Short Message Service (SMS) and the Multimedia Messaging Service (MMS). Two upgrade versions of this generation were introduced later to provide higher data speeds, namely the General Packet Radio Service (GPRS) which provided data rates

of 35-171 Kbps and the Enhanced Data Rates for GSM Evolution (EDGE) which provided data rates of 120-384 Kbps.

The third generation of mobile technology, 3G, was introduced commercially in the early 2000s under the three incompatible standards using code-division multiple access (CDMA) for signal channelization: Universal Mobile Telecommunications System (UMTS, deployed world-wide), CDMA2000 (deployed primarily in North America) and Time-Division-Duplex Synchronous CDMA (TD-SCDMA, deployed in China). UMTS, also known as W-CDMA, can support peak data rates of up to 384 kbit/s for both uplink and downlink. The efforts to improve UMTS data rates resulted in the introduction of two upgraded standards: the High-Speed Packet Access (HSPA), sometimes called 3.5G, and the evolved HSPA (HSPA+). In HSPA, the High-Speed Downlink Packet Access (HSDPA) enables peak data rates of 14 Mbit/s in the downlink, and the High-Speed Uplink Packet Access (HSUPA) enables peak data rates of 5.8 Mbit/s in the uplink. HSPA+ can theoretically achieve up to 337 Mbit/s in the downlink and 34 Mbit/s in the uplink.

The speed of 3G quickly became insufficient as technology and smartphones evolved, demanding higher data rates. To meet this demand, the fourth generation of broadband cellular network technology, 4G, was developed and commercially deployed in 2009 under the Long Term Evolution (LTE) and LTE-Advanced standards. Although it is debatable whether LTE should be considered a 4G standard since it does not meet the International Mobile Telecommunications Advanced (IMT-Advanced) requirements, LTE is often branded as a 4G standard. 4G enriched users' experience with high-quality video streaming, HD videos, and online gaming. LTE provides theoretical peak data rates up to 300 Mbit/s in the downlink and 75 Mbit/s in the uplink, while LTE-A provides theoretical peak data rates up to 3 Gbit/s in the downlink and 500 Mbit/s in the uplink.

The 5^{th} generation of mobile broadband networks, 5G, came after 4G as an evolution in mobile broadband technology. 5G networks promise to deliver high multi-Gbps peak download/upload speeds, ultra-low latency, superior network security, massive network capacity, less energy consumption, and uniform user experience regardless of the location inside the cell. According to 3GPP, the standardization of 5G has been completed in Release 15 updated in June 2018. Further releases (e.g., Release-16, finalized in 2020, and Release-17, expected to be finalized in 2022) have added additional features to the 5G standard.

The vision of 5G is to deploy what is called sliced network systems where the network is adaptive in enabling independently the three major use cases of 5G [3], [4]:

- **Enhanced Mobile Broadband (eMBB):** support for the hugely increased data rates, mostly due to the streaming and downloading of 3D and ultra high definition (UHD) content, adaptability to virtual reality (VR) and augmented reality (AR) applications, and more uniform data rates for users in crowded locations.

- **Ultra-Reliable and Low Latency Communications (URLLC):** for mission-critical communications such as remote medical surgeries, industrial robot control, self driven vehicles, and cloud gaming.

- **Massive Machine-Type Communications (mMTC):** requiring low data rates, narrow bandwidth, low power consumption, and seamless connectivity for a very large number of devices, machines, objects and sensors to enable what is called the internet of things (IoT), which is the foundation of smart cities [5].

The 3GPP submitted the 5G New Radio (NR) system specifications to the International Telecommunication Union (ITU) as a candidate 5G mobile communication system [6]. The ITU Radio-communication Sector (ITU-R) of the ITU issued in its ITU-R M.2410-0 set of requirements report the International Mobile Telecommunications-2020 (IMT-2020) for 5G networks, devices, and services. According to the report, the minimum technical performance requirements of 5G networks are:

- **Downlink peak data rate:** 20 Gbit/s.

- **Uplink peak data rate:** 10 Gbit/s.

- **Downlink peak spectral efficiency:** 30 bit/s/Hz.

- **Uplink peak spectral efficiency:** 15 bit/s/Hz.

- **Downlink user-experienced data rate:** 100 Mbit/s.

- **Uplink user-experienced data rate:** 50 Mbit/s.

- **User plane latency:** 4 ms for eMBB, 1 ms for URLLC.

- **Connection density:** 1000000 devices per km^2.

- **Mobility:** up to 500 km/h.

- **Bandwidth:** at least 100 MHz and up to 1 GHz for operation in higher frequency bands (mmWave range).

On the other hand, the energy consumption of wireless mobile networks is comparably growing by the same order of increase as the data rates [7]. The carbon footprint for information and communication technologies (ICT) is already globally significant and becoming unsustainable. According to [8], ICT

is estimated at 1.8%–2.8% of global Greenhouse gas emissions in 2020. The ICT carbon emission is likely to increase with the expected massive increase in data rates and the advent of the IoT concept in 5G, where billions of devices are talking to each other. Therefore, energy efficiency is a major theme of interest in 5G networks, as equally important as the three primary use cases of 5G mentioned earlier.

After knowing the technical specifications of 5G networks, the main question is how such networks are realized; how these high data rates, ultra-low latency, and massive connectivity of devices will be achieved. There are three main key enabling technologies to achieve data rates in the Gbps range.

(**a**) **Massive MIMO:** Multiple-input multiple-output (MIMO) systems are one of the most critical technological breakthroughs in advanced digital wireless communication systems. MIMO offers a substantial improvement in wireless capacities by exploiting the space dimension. It has been proven that through the mere use of physically-separated multi-antenna elements at both the transmitter and the receiver, enormous capacities can be achieved through multi-path propagation without utilizing more transmit power or channel bandwidth. This pioneering technology translates into better spectral and power efficiency in addition to higher data rates [9]. The most known MIMO techniques are diversity and spatial multiplexing. Diversity uses multiple antennas to send many copies of the data stream. It aims to enhance wireless link quality [2]. In spatial multiplexing, data is divided into multiple sub-streams, and each substream is independently transmitted on a different transmit antenna to offer higher peak throughput [10]. In a single-user MIMO (SU-MIMO) system, also known as point-to-point MIMO, both the transmitter and the receiver are equipped with multiple antennas. The maximum number of spatial streams in SU-MIMO is limited by the lesser number of antennas at the transmitter or receiver. Hence, the order of increase in capacity (bits per channel use) is also bound by the lesser number of antennas at the transmitter or receiver. Since the SU-MIMO relies heavily on the spacing between the antennas in both the transmitter and the receiver, it becomes unfeasible for handsets that are constrained by space, and thus cannot allow for enough antenna spacing. Additionally, multiplexing gains may diminish near the edges of the cell where SIR is low, or if the environment is not sufficiently rich in scatterers. Due to the limitations of SU-MIMO and as part of an ongoing effort in further expanding potential network capacity, an evolved version of the system has emerged, namely the multi-user MIMO (MU-MIMO). In MU-MIMO, the base station, equipped with many antennas, serves multiple users over the same time-frequency resource [11]. MU-MIMO allows spatial multiplexing gain to be achieved at the base station without requiring multiple antennas at the user equipment (UE). However,

this advantage comes at the cost of needing advanced signal processing techniques at the transmitter, known as precoding, which requires the availability of channel state information (CSI) at the transmitter. In both SU-MIMO and MU-MIMO, the larger the number of antennas in both the transmitter and the receiver, the more significant the channel matrix entries are, thanks to spacing and cross-polarization, allowing for enhanced spectral efficiency.

Thomas Marzetta, a pioneer researcher in the area of MIMO, envisioned in [12] that by equipping base stations with many antennas, much more than the number of active users per time-frequency symbol, an enormous enhancement in spectral and energy efficiency could be achieved upon the availability of perfect CSI. This idea is considered an extension of MU-MIMO to a much larger number of antennas at the BS. It was initially named large-scale antenna systems but is now more widely referred to as massive MIMO. In massive MIMO, the number of antennas at the base station is typically $4 - 10$ times larger than the number of users. The large number of antennas deployed in massive MIMO transmitters, when utilized in the sub-6 GHz frequency range, achieves high data rates due to the spatial multiplexing gain. To accomplish that, precoding schemes at the transmitter are essential [13].

On the other hand, the high number of antennas in massive MIMO transmitters operating in the mmWave range generates high-gain narrow beams. These high-gain pinpointed beams help to focus the transmission and reception of signal energy into smaller regions in space, targeting specific users through beamforming. Thus, overcoming the high path loss in the mmWave frequencies and bringing vast improvements in coverage and energy efficiency [14]. Moreover, the capacity in mmWave systems is high due to the availability of large bandwidths in the mmWave range. These benefits have elevated massive MIMO to a major critical enabling technology of 5G [15]. The antennas in massive MIMO transmitters can be deployed in many forms; linear, planar, cylindrical, or distributed, as shown in Fig. 1.1.

A research group at Lund University in Sweden introduced a real-time testbed for massive MIMO in 2016 [17]. The system consists of a planar T-shaped antenna array at the base station with 160 dual-polarized $\lambda/2$ patch elements. Up to 100 base station antennas have been deployed to serve 12 UEs using the orthogonal frequency-division multiplexing (OFDM) and time-division duplex (TDD) schemes. The research team tested the system and conducted indoor and outdoor measurements. The purpose of the experiment was to prove the concept that massive MIMO can simultaneously serve multiple users using the same time/frequency

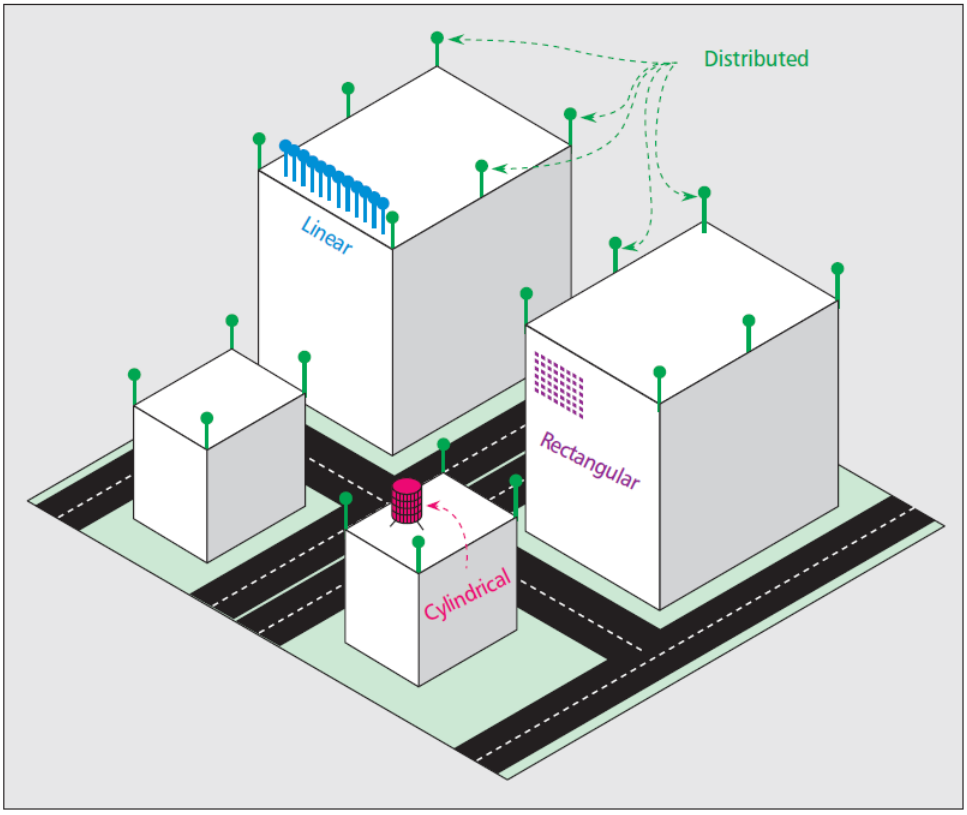

Figure 1.1: Antenna deployment scenarios in massive MIMO base stations. Adapted from [16].

resource block and provide a flexible platform for testing algorithms.

(b) **Millimeter Wave (mmWave) systems:** Another solution to increase the capacity of wireless systems is to increase the operational bandwidth. Many current and past generations of wireless systems have operated on microwave frequencies ranging from several hundred MHz to a few GHz, corresponding to wavelengths of a few centimeters to about a meter [18]. Despite the spectrum being limited, expensive, and already occupied by most carriers today in the sub-6 GHz spectrum range, many advanced resource allocation algorithms and techniques effectively utilize the available bandwidth to its maximum potential. However, the introduction of mmWave systems has been crucial for increasing network capacity, thanks to the availability of a broader bandwidth alongside the advanced resource allocation schemes [19]. Fortunately, large parts of the relatively unused radio spectrum are available in the mmWave range. The specifications for 5G NR (New Radio) consider two frequency ranges for operation: The first range is (410 MHz to 7.125 GHz), known as the sub-6 GHz, and the second range is (24.25 GHz to 52.6 GHz), known as

the mmWave range.

While the mmWave spectrum offers an excellent opportunity to increase channel capacity, the main reason mmWave frequencies remained unused for mobile communication is that, until recently, they had been considered unsuitable for mobile communications due to the difficult radio channel propagation characteristics at mmWave frequencies. The free space path loss (FSPL), which can be derived from Friis transmission formula [20], is given by:

$$FSPL = \left(\frac{4\pi d f_c}{c}\right)^2 \tag{1.1}$$

where d is the distance between the transmitter and the receiver, f_c is the carrier frequency, and c is the speed of light. As can be deduced from the equation, the FSPL is proportional to the frequency squared. Meaning that if the carrier frequency increased by order of magnitude (e.g., from 3 GHz to 30 GHz), the power of the transmitted RF signal will incur a loss of 20 dB regardless of the distance between the transmitter and the receiver. Additionally, there are other concerns about the relatively harsh propagation qualities of frequencies in mmWave systems, mainly due to oxygen and rain absorption and poor penetration through objects [21].

However, the path loss caused by the increase in the carrier frequency f_c can be compensated. Since the wavelength in the mmWave range is shorter, it will enable the packing of many antenna elements within the original area, providing very high-gain and narrow beams. The high-gain narrow-beamwidth provided by large antenna arrays in the mmWave range can increase the signal-to-noise ratio (SNR) and counter the free-space pathloss. Moreover, it will result in reduced co-channel interference to steer these narrow beams selectively toward desired groups of users. The narrow beams generated by massive antenna arrays in the mmWave regime can substantially overcome path loss by increased antenna gain. Beamforming is a crucial aspect of modern wireless systems. High-gain, focused beams are essential in combating path loss and increasing the coverage.

Despite the historical use of the (8 - 12 GHz) range for satellite communications, mmWave frequencies were limited to long-range point-to-point communications and military applications. Their viability in utilization for communications in cellular systems is explored in [22]. Moreover, coverage of cells with 200 m radii at mmWave frequencies was reported in [23]. However, there are many other non-trivial hurdles, other than the propagation issue, facing the adoption of mmWave frequencies. Chief

among these challenges is the very large power consumption of hardware components like the analog-to-digital converters (ADC) and the digital-to-analog converters (DAC) that will be operating on large bandwidths. Additionally, large antenna arrays are needed to be implemented to achieve high-gain narrow beams. Driving such large antenna arrays will introduce a new set of challenges in hardware implementation and power consumption.

(**c**) **Network Densification:** An extremely effective way to increase the cell capacity while using less transmit power, is to shrink the cell size. Picocells (in the range of 100 m - 300 m) and femtocells (in the range of 10 m - 30 m) are promising candidates for adoption in 5G mobile networks [24]. Picocells are more suitable for outdoor hotspots (e.g., parks, stadiums), while femtocells are more catered to indoor locations (e.g., homes, offices, etc.) [25]. Since the aggregate throughput from a cell is the same regardless of the size of the cell, dividing a macrocell, a microcell, or a picocell into many femtocells will increase the total capacity [26]. Moreover, shrinking the cell footprint reduces the number of users contending for resources at each low-cost, low-power Femto access point (FAP). Additionally, the abundance of line-of-sight and high signal-to-interference ratio (SIR) allow user equipment (UE) devices to utilize low power for communication with FAPs, leading to saving energy and allowing for longer battery life [27]. Nevertheless, at some point, ultra-dense networks can hit a plateau and stop achieving significant throughput gains. Therefore, massive MIMO and mmWaves have gained more attention as enabling technologies of 5G.

Although MIMO systems, massive MIMO in particular, have theoretically shown the potential to achieve remarkable gains in capacity and coverage, some practical issues may limit these gains. There are two severe challenges to the realization of massive MIMO systems. The first challenge is related to the overall cost of the system. The current MIMO transmitters deploy a dedicated RF chain per antenna element. Each RF chain consists of a Local Oscillator (LO), power amplifier (PA), mixer, and DAC. Hence, the more antenna elements are, the higher the RF cost of the system. This linear relationship between antennas and the RF chains is a significant challenge in massive MIMO base stations because they are expected to be equipped with tens or hundreds of antenna elements. In typical macro base stations, it has been estimated that PAs consume a significant portion of the total energy (about 57%) and the cooling/air conditioning components consume another 10% of the total energy [28].

The second challenge that impairs the deployment of massive MIMO transmitters is the size issue. Conventionally, antenna arrays must have the antenna elements spaced half a wavelength apart to avoid the negative effects of mutual

coupling [29]. This requirement leads to the size issue, which can be more pronounced in large antenna arrays that are expected to be deployed in massive MIMO transmitters.

This dissertation aims to reduce the cost and complexity of MIMO transmitters to overcome the challenges of deploying massive antenna arrays. This dissertation shows that a different design approach to analog hardware makes low-cost, low-profile, and energy-efficient MIMO transmitters possible.

In the current chapter, Section 1.1 introduces the contributions in this dissertation briefly. The structure and outline of the next chapters are given in Section 1.2.

1.1 Contributions

- **A 64-QAM load modulator:** A low-cost, low-profile, and energy-efficient 64-QAM load modulator is presented. The modulator is designed to operate at 3 GHz. The load modulator generates 64-QAM constellations by changing its internal parameters. The load modulator is implemented using microstrip transmission lines and p-i-n diodes. The load modulator circuit uses the serial concatenation of several L-section microstrip lines. An optimization algorithm has been used to find the design parameters of the load modulator circuit. A microcontroller system provides bias voltages to the p-i-n diodes in the load modulator representing the baseband data. The proposed architecture does not require a digital-to-analog converter (DAC) for modulation, and the signal generator remains fixed all the time. The proposed modulator has been fabricated, and measurements have been taken to verify its performance.

- **A reduced-complexity energy-efficient load modulated MIMO transmitter:** A single-RF four-branched MIMO transmitter is designed. The four antenna elements are connected to a single RF chain through the proposed 64-QAM load modulator. The proposed MIMO transmitter shows excellent potential in reducing the cost and saving energy compared to the current state of the art of MIMO transmitters. The load modulator is responsible for generating the desired outputs on the antenna. Thus, the PA in the RF chain is constantly amplifying a fixed input signal and does not have to be linear. Additionally, there is no need for DACs and mixers. The proposed transmitter can be easily scaled up and integrated with large antenna arrays making it a promising candidate for adoption in massive MIMO base stations.

1.2 Structure and Dissertation Outline

Chapter 2 explains the required background for the next chapters. In Chapter 2, a general system model for MU-MIMO is presented. Furthermore, the issues and existing solutions in MIMO systems are discussed.

Chapter 3 comprehensively presents the theoretical analysis, design procedure, fabrication steps, and performance evaluation of the low-cost, low-profile, and energy-efficiency 64-QAM load modulator.

In Chapter 4, the load modulator designed in Chapter 3 is integrated into the design of a reduced-complexity single-RF four-branched load-modulated MIMO transmitter. Furthermore, the potential for scaling up this MIMO transmitter for use in massive MIMO transmitters is presented. A discussion about energy saving and efficiency enhancement of load modulated MIMO transmitters is provided.

Finally, Chapter 5 summarizes the contributions of this dissertation, presents some directions for possible future work, and concludes the dissertation.

Chapter 2

Background

In this chapter, a general system model for MU-MIMO is presented. Massive MIMO will also be described. Then, the existing issues in massive MIMO systems will be explained, including the cost and the size issue.

2.1 MIMO Systems: Definitions and General System Model

MIMO is based on the idea that by employing multiple antennas at both the transmitter and receiver, very high data rates can be achieved under the condition of deployment in a rich-scattering propagation medium. This interesting property of MIMO systems made it very popular in adoption in modern wireless communication technologies.

Consider a BS equipped with N_t antennas. This BS serves L users located around the BS, and each of these users equipped with N_r antennas, as shown in Fig. 2.1. In the downlink channel, the baseband signals of user 1, user 2, and user L are denoted by u_1, u_2, and u_L, respectively. Each user's signal passes through the precoder block resulting in signals v_1, v_2, and v_L for user 1, user 2, and user L, respectively. The signals at the output of the precoder v_1, v_2, and v_L are transmitted via antennas N_1, N_2, and N_t, respectively. The channel matrix between the base station and the l-th user is described by an $(N_t \times \mathrm{N}_r)$ matrix and denoted by $\mathbf{H}_\ell$.

The output-input relationship in the downlink can be described as

$$r = \mathbf{H}v + n \tag{2.1}$$

where

$$r = [r_1^T, ..., r_L^T]^T \tag{2.2}$$

$$\mathbf{H} = [\mathbf{H_1^T}, ..., \mathbf{H_L^T}]^T \tag{2.3}$$

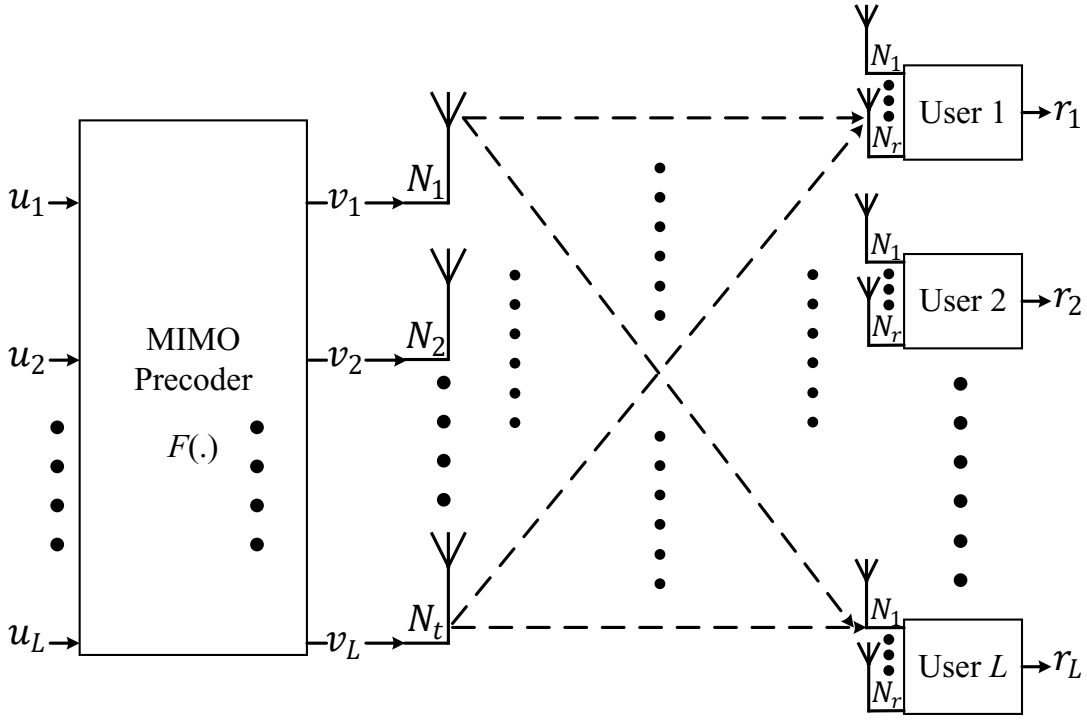

Figure 2.1: The block structure of a MU-MIMO system.

$$v = [v_1^T, ..., v_L^T]^T \tag{2.4}$$

$$n = [n_1^T, ..., n_L^T]^T \tag{2.5}$$

where r and n are the received signal vector by the antennas and n is the additive noise vector. The precoder function is defined as

$$v = \mathbf{F}(u) \tag{2.6}$$

where

$$u = [u_1^T, ..., u_L^T]^T \tag{2.7}$$

and $\mathbf{F}(.)$ is the precoder function. The point-to-point MIMO channel can be obtained by reducing the number of users to 1 ($L = 1$).

In the uplink channel, all users transmit their signals to the BS. The signals transmitted by user 1, user 2, and user L are denoted by x_1, x_2, and x_L, respectively. The signals received by the BS from user 1, user 2, and user L are y_1, y_2, and y_L. The channel model in the uplink can be described as

$$y = \mathbf{G}x + z \tag{2.8}$$

where

$$x = [\hat{x}_1^T, ..., \hat{x}_L^T]^T \tag{2.9}$$

$$\mathbf{G} = [\mathbf{G_1}, ..., \mathbf{G_L}] \tag{2.10}$$

and $z \in \mathbb{C}^{N\times 1}$ is the Additive White Gaussian Noise (AWGN) with variance σ^2 The point-to-point MIMO channel can be obtained by reducing the number of users to 1 ($L = 1$)

2.2 Capacity Enhancement in MIMO Systems

The goal of point-to-point MIMO systems deployed in the sub-6 GHz range is to improve the capacity of the system without utilizing more bandwidth or power. A point-to-point MIMO system consisting of N_t transmit antennas and N_r receive antennas is taken into consideration. Moreover, perfect CSI knowledge is assumed to be available for the transmitter via pilot sequences sent in each coherence time. For simplicity, a point-to-point single antenna link with an average transmit power P is considered. The channel model is given by

$$y = hx + n \tag{2.11}$$

where y is the received signal, h is the channel coefficient, x is the transmit signal, and n is the AWGN with variance σ^2. The maximum achievable spectral efficiency for a given channel coefficient h, can be calculated from the Shannon formula as

$$C = \log_2\left(1 + h^2\frac{P}{\sigma^2}\right) \tag{2.12}$$

The spectral efficiency is defined as the number of bits per second per Hertz. The channel coefficient h models the fading effect. For a MIMO system with an output-input relationship as the one given in (2.1), and by considering the singular value decomposition of the channel $\mathbf{H}$, the received signal can be written as

$$r = \mathbf{U}\mathbf{D}\mathbf{V}^{\dagger}v + n \tag{2.13}$$

where U and V are unitary matrices and D is the diagonal matrix that contain the singular channel values. The squared singular values are the eigenvalues of $\mathbf{H}\mathbf{H}^{\dagger}$. The non-zero eigenvalues of $\mathbf{H}\mathbf{H}^{\dagger}$ are the relevant ones and are limited by the by the lesser number of N_t and N_r. If we define

$$\tilde{r} = \mathbf{U}^{\dagger}r \tag{2.14}$$

$$\tilde{v} = \mathbf{V}^{\dagger}v \tag{2.15}$$

$$\tilde{n} = \mathbf{U}^{\dagger}n \tag{2.16}$$

The considered MIMO channel can be converted to single point-to-point communication links as

$$\tilde{r}_i = \lambda_i\tilde{v}_i + \tilde{n}_i \tag{2.17}$$

where λ_i are the eigenvalues of the matrix $\mathbf{H}\mathbf{H}^{\dagger}$, and $i = 1, 2, ..., \min(N_t, N_r)$. The spectral efficiency of the MIMO system is then equal to the sum of the spectral efficiencies of the equivalent point-to-point links. The water-filling

method can be applied to find the channel capacity [30]. Hence, the spectral efficiency is given by

$$C = \sum_{i=1}^{min(N_t,N_r)} \log_2 \left(1 + \frac{P_i^* \lambda_i^2}{\sigma^2}\right) \tag{2.18}$$

where P_1^*, P_2^*, ..., and $P_{min(Nt,Nr)}^*$ are the water-filling power allocation given by:

$$P_i^* = \left(\mu - \frac{\sigma^2}{\lambda_i^2}\right) \tag{2.19}$$

where μ is chosen to satisfy the total power constraint $\sum_i P_i^* = P$.

Let n be the number of non-zero eigenvalues in the channel matrix $\mathbf{HH}^\dagger$. The original MIMO link can thus be treated as n of the (2.17) parallel single-antenna links. Thus, the capacity can be enhanced by a factor of n. It is worth mentioning again that n is upper bounded by the lesser of the number of antennas at the transmitter and the receiver.

It is clear that the capacity in a MIMO system improves by having as many non-zero eigenvalues in the channel matrix as possible. These non-zero eigenvalues can be become more abundant in scatter-rich environments. For example, in line-of-sight (LOS) MIMO links, there will be only one non-zero eigenvalue in the channel matrix; therefore, the only benefit in this case is the SNR enhancement. However, in a multi-path environment, the capacity can be enhanced by a factor equal to the minimum number of antennas at the transmitter and the receiver. Although perfect CSI knowledge was assumed in the analysis above, the channel matrix is not completely known and one needs to consider the effect of channel estimation and pilot sequence length when deriving the total capacity.

The above analysis shows that MIMO systems in environments with rich scatters can boost the data rate by a factor of the minimum of the number of transmit and receive antennas. This means that without utilizing more power and bandwidth, the data rate in cellular networks can be increased just by increasing the number of antennas.

2.3 Massive MIMO

The previous section explained the benefits of employing multi-antenna arrays at both the transmitter and the receiver. It has been shown that the throughput of the system increases by a factor of the lesser of the number of antennas deployed at either the transmitter or the receiver. Typically, the user end has fewer antennas deployed on their UEs. However, increasing the number of

antennas at the transmitting BS can improve both capacity and coverage of the system. Multiple antenna elements at the transmitter can be coherently used to concentrate the transmit power at selected users reducing the overall transmit power considerably [31]. This concept motivated the introduction of massive MIMO systems. Massive MIMO is a MU-MIMO system with a central BS deployed with a large number of antennas serving K number of users in each cell. This K number of users in the cell can be served simultaneously at same frequency and time slots by the spatial multiplexing created by the base station. The gain achieved by this configuration is called the multiplexing gain of MIMO systems. Theoretically, the sum rate capacity of a massive MIMO system grows with $\min(N_t, K)$, where N_t is the minimum of the number of antennas at the BS and K is the number of users. When both N_t and K increase, the number of non-zero eigenvalues in the channel matrix $\mathbf{HH}^{\dagger}$ increases, which results in an increase in the sum rate capacity of the systems, as shown in the previous subsection.

Moreover, in massive MIMO, the number of antennas N_t at the transmit BS is significantly larger than the number of users served inside the cell. This configuration offers some degree of freedom (DoF) to the transmit BS to focus the transmit power to the selected users, as shown in Fig. 2.2.

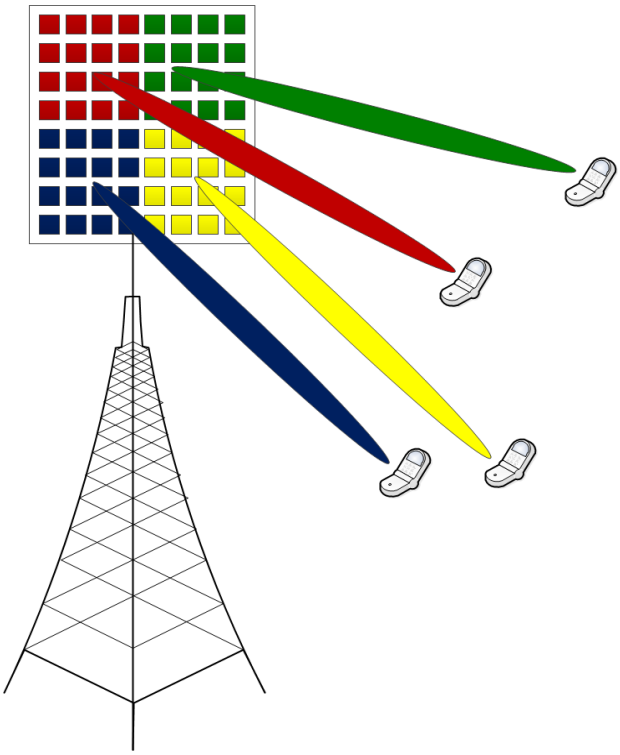

Figure 2.2: Illustration of a massive MIMO BS serving multiple users simultaneously.

The gain achieved through directing beams towards users chosen is called the diversity gain [32]. The realized diversity gain is crucial in wireless systems operating in low-power regimes. Additional to the benefit of utilizing less transmit power when directing narrow beams towards selected users, the inter-user interference is significantly reduced; resulting in a larger achievable sum rate capacity.

To explain the idea of massive MIMO, consider for a moment the uplink channel model introduced in the previous subsection. The users are assumed to be equipped with single-antenna UEs, and they do not initially have access to CSI. In each symbol time of the channel, the users communicate with the BS via some predefined pilot sequences. The BS can estimate the channel matrix for all users from these pilots. The BS uses the estimated channel matrix $\hat{\mathbf{H}}$ to detect the signal of users. Many types of detectors have been introduced in the literature, both linear and non-linear, including matching filters, zero force (ZF), and Minimum Mean Square Error (MMSE) [33], [34].

The realized gains are even more pronounced if the BS have access to CSI. In the presence of perfect CSI, the signal-to-interference-plus-noise ratio (SINR) realized after the detector increases by a factor proportional to the ratio of the number of antennas at the transmitter to the number users served [35]. On the other hand, one of the bottlenecks that massive MIMO systems face is when users from other cells reuse the same orthogonal pilots. Due to the finite coherence time, bandwidth, and length of the pilot sequence, the number of orthogonal codes in a codebook is limited. To minimize the overhead of the channel estimation, two or more users must share the same pilot sequence. However, when two adjacent cells use the same pilot sequence it leads to inter-user-interference in the channel estimation, which is known as the pilot contamination (PC) phenomenon [36]. In fact, in the presence of pilot contamination from other cells, the interference caused by using linear detectors does not diminish by increasing the number of antennas [12]. Many techniques have been introduced in the literature to alleviate the severe consequences of pilot contamination [37]. It has been shown that increasing the number of antennas at the BS can mitigate pilot contamination by using complicated non-linear detectors. Nevertheless, pilot decontamination is not in the scope of this dissertation.

Since CSI is only required to be known by the transmit BS, all the precoding processing is done in the baseband by the BS. Thus the UEs in massive MIMO systems do not need to be complicated as they do not require any complex processing. To do precoding in the BS, the channel matrix is required. Two methods of multiplexing have been introduced: Time-Division Duplex (TDD) and Frequency-Division Duplex (FDD) [38]. The uplink and downlink channels in TDD are separated by different time intervals in the

same frequency band. For example, if the first time interval is allocated for the uplink channel, users transmit pilots to the BS. The BS estimates the channel matrix from these pilots and detects the uplink data. The next time interval is allocated for the downlink transmission. Suppose the two time intervals occur in the same coherence time duration of the channel. In that case, the BS uses the same estimated channel matrix in the uplink to perform precoding on users' data in the downlink, thanks to the reciprocity of the channel.

In FDD, both the uplink and downlink channels are in different frequency bands. Hence, leveraging channel reciprocity is impossible, and downlink pilots are typically needed. However, in a brute-force implementation of FDD in massive MIMO cellular networks, the main drawback is the need for CSI feedback from UEs for downlink transmission because BS cannot estimate its downlink CSI. Hence, a brute-force implementation of massive MIMO in the FDD mode is challenging. The CSI feedback needed from the UEs would be enormous and would consume practically all available UL radio resources leaving next to nothing for the UL transmission of data [39].

2.4 Existing Challenges in Massive MIMO

The theoretical advantages of massive MIMO represented by the higher achievable data rates and the ability to overcome high path loss, when deployed in the mmWave range, through very narrow beamforming are key elements of 5G networks. However, several challenges must be first addressed and overcome for massive MIMO to become a reality. The challenges associated with implementing massive MIMO systems will be discussed in this section.

2.4.1 Cost issues

Conventional MIMO transmitters deploy a dedicated RF chain per antenna element [40]. Each RF chain consists of a local oscillator (LO), power amplifier (PA), a mixer, and a DAC/ADC. Massive MIMO BSs are equipped with many antenna elements (e.g., tens or hundreds). With a brute-force approach, each antenna element within this large antenna array would be expected to be driven by a dedicated RF transceiver chain. However, it is very challenging to scale up the number of RF chains by the same order due to cost, energy consumption, interference, and physical footprint. Antennas are typically the cheapest component in the RF transceiver. Therefore, the number of antennas at the transmit BS can be increased without cost concern. However, the cost of the system increases vastly if a dedicated RF chain is deployed for each antenna element. Moreover, the high energy consumption of these RF circuits may cancel out, or even dominate, the energy savings achieved through the significant array gains of massive MIMO, diminishing a key feature of massive MIMO.

2.4.2 Hardware complexity

In addition to their high cost, PAs are among the most power-consuming components in wireless communication systems [28]. The efficiency of PAs is mainly determined by the peak-to-average ratio (PAPR) of the input signal. High spectral efficiency multi-carrier modulation schemes, such as the Orthogonal Frequency Division Multiplexing – Quadrature Amplitude Modulation (OFDM-QAM), are used extensively in modern wireless data transmission systems (e.g., LTE, LTE-Advanced and 5G NR) due to their robust transmission under frequency selective fading channel conditions. OFDM signals are generated using inverse fast Fourier transform (IFFT) signals and are equivalent to the summation of signals on multiple sub-carriers. OFDM signals are highly non-constant envelope modulation signals that exhibit relatively large dynamic fluctuations in the envelope, some of which are above the linear amplification region and distorted through a nonlinear amplifier. The inherent problem of OFDM signaling is the generation of output signals with high PAPR, which cannot be transmitted efficiently. For high PAPR signals, the PA must be linear to support amplitude and phase modulation and avoid inter-channel interference and detection errors, driving its cost while reducing its efficiency [41].

Class-A, Class-B, and Class-AB PAs are commonly used in wireless transmitters since they are linear and support high PAPR signals [42]. In addition to the high cost of Class-A and Class-B PAs, the transmission of high PAPR signals requires the PA in the RF transmitter to operate in its back-off region most of the time. Therefore, the overall performance of the RF transmitter is compromised since the PA has low power efficiency in its back-off region [43]. For example, to amplify a Rayleigh-distributed signal with 7.5 dB PAPR, the maximum efficiency of the Class-A PA will drop from what is conventionally 50% to 8.7%. In contrast, the peak efficiency of linear Class-B PAs is 78.5%. However, the efficiency of Class-B PAs drops down by half for every 6 dB output back-off (OBO). In OFDM, the PAPR is typically in the range of 8 dB to 13 dB. Therefore, the theoretical efficiency of an ideal Class-B PA can drop to around 20% when transmitting OFDM signals. Practically, the efficiency will drop even more [44], [45]. The story is the same for Class AB PAs. For an OFDM signal with 8dB to 12dB PAPR, the power efficiency of Class AB PAs is about 31% to 20%, respectively.

Many PAPR reduction techniques have been extensively investigated for multi-carrier transmission, including amplitude clipping and filtering, coding, partial transmit sequence, and interleaving [46]–[49]. However, PAPR reduction is usually achieved at the cost of a loss in the data rate, increased transmitted signal power, increased bit error rate, and advanced computational complexity [48]. PAPR reduction techniques are not within the scope of this

dissertation.

2.5 Existing Solutions for RF Cost Reduction

The concept of load modulation has been introduced in the literature to overcome the challenges associated with the high cost and the linearity demand of the PA in the RF transmitter [50]–[53]. In standard RF transmitters, the voltage source output is changed in proportion to the transmitted signal amplitude. As mentioned earlier, this modulation type requires a linear amplifier with large back-off (e.g., Class-AB) to drive the antenna. In load modulation, the PA amplifies a constant sinusoidal signal all the time and does not need to operate in the back-off region. At the same time, the antenna is driven by a two-port network called the load modulator. Load modulators are RF microwave circuits that contain high-speed RF switches [54]. The desired voltages and phases representing the transmitted signal can be produced at the input of the antennas without tuning the output of the voltage source but rather by changing the internal parameters of the load modulator (e.g., changing the RF switch state in the load modulator).

The earlier works on load-modulated MIMO transmitters focused primarily on their integration in the design of conventional MIMO systems and analog beamformers. For example, the works in [55]–[63] revolved around building antenna arrays consisting of a single active antenna element connected to a voltage-modulated power source and a group of passive antenna elements surrounding the active element and terminated by variable reactive loads. Such systems are referenced in the literature as electronically steerable passive array radiators (ESPARs). The active element inductively feeds the passive elements, and the currents on the passive elements are controlled by changing their reactive load impedances [61], as shown in Fig. 2.3. The overall radiation beam generated by the antenna array can be steered in the desired directions by generating the proper input currents on the passive elements. These currents are generated through the careful selection of the impedances of the tunable loads attached to the parasitic antenna elements. These systems were more compatible with the design of standard compact MIMO transmitters at a reduced cost. However, these systems are not compatible with massive MIMO due to the fact the antenna elements should be around the active element which limits the number of antenna elements in the system.

An interesting electronic beam steering array with reactive elements was introduced in [59]. The architecture consisted of a circular array of six parasitic elements and an active radiator at the center, as shown in Fig. 2.4. Each element consists of a quarter-wavelength monopole and a variable capacitor. The central monopole is connected to the voltage source and acts as the active radiator. By fine-tuning the value of the capacitances on all monopoles,

the main transmitting beam is steered to desired directions. The design was promising since it solved the problem of employing a dedicated radio receiver per antenna.

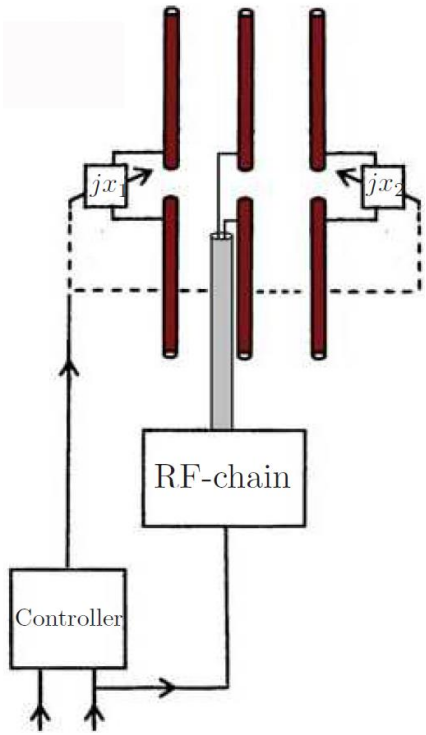

Figure 2.3: Schematic of an ESPAR system. Adapted from [61].

Another proof-of-concept load-modulated MIMO transmitter was presented in [64]. The prototype consists of three printed dipoles, a central active dipole surrounded by two parasitic dipoles, as depicted in Fig. 2.5. The two parasitic dipoles are connected to variable loads. The loads on the parasitic elements are controlled using PIN diodes. The prototype achieved over-the-air transmission of BPSK signals at a rate of 820 kbps at 2.6 GHz. However, the system is not applicable at higher modulation orders because of the purely imaginary loads connected to the parasitic elements.

Another prototype was designed to transmit multiple signals using a single RF chain [65]. The prototype was suitable for integration in small wireless devices, as shown in Fig. 2.6. A comparison between the performance of ESPAR antennas and load modulated antennas in terms of power consumption and bit error rate reduction was presented in [66].

Six-port correlators are also popular in the literature in utilizing the concept of load modulation [67]–[72]. They consist of one power divider, three 90° branch-line couplers, one input port, one output port, and four ports terminated by variable loads. By carefully selecting the variable terminating loads, the incident wave at the input port experiences various phase shifts when trav-

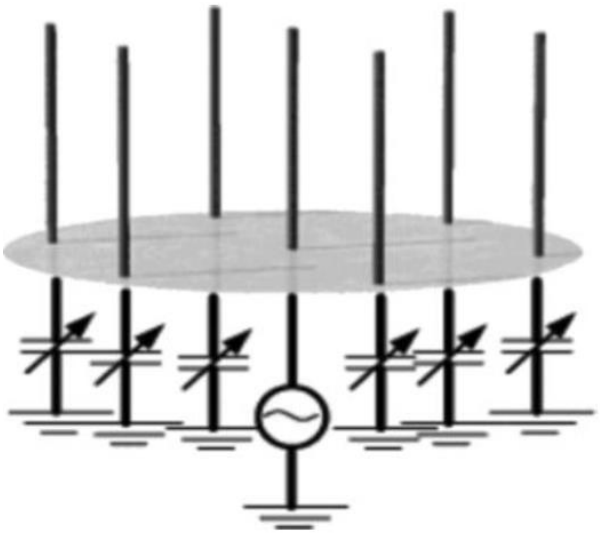

Figure 2.4: Antenna configuration for electronic beam steering. Adapted from [59].

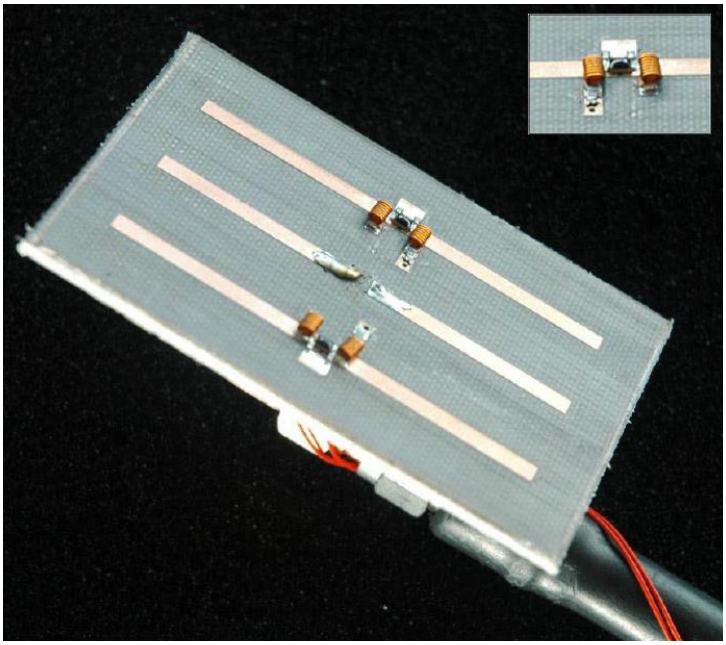

Figure 2.5: Fabricated prototype of a compact switched parasitic array. Adapted from [64].

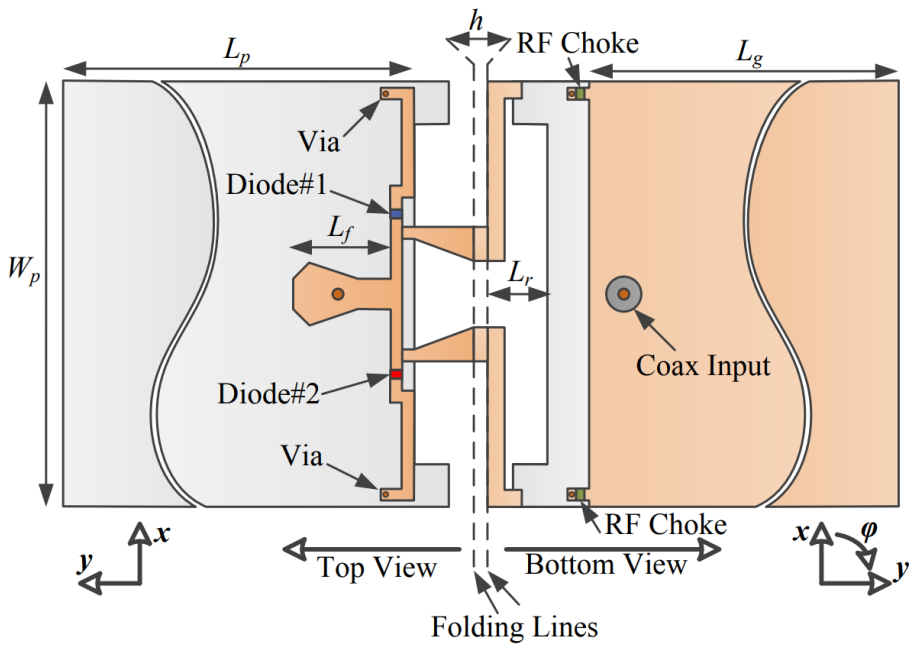

Figure 2.6: A compact single RF frequency tunable antenna. Adapted from [65].

eling along the six-port modulator's transmission lines and getting reflected by the variable terminating loads. Thus, a desired modulated signal can be generated at the output port. For example, the work in [67], proposed a six-port modulator used as a single antenna and was realized with Schottky diodes as variable load impedances, as shown in Fig. 2.7.

The final prototype was able to generate load-modulated 16-QAM signals at a data rate of 1.2 Gbps. In addition to the performance limitation imposed by the non-linearity of Schottky diodes, the prototype was limited to only the 16-QAM modulation scheme since only four ports of the load modulator were connected to variable loads allowing only 16 possible states of the terminating loads.

The work in [72] presented an upgraded design of the six-port modulator that is capable of generating 64-QAM signals. Instead of terminating the four ports directly by variable loads, each of these four ports was instead connected to a three-way power divider, as illustrated in Fig. 2.8.

The output ports of the power dividers were connected to variable load impedances allowing for more degrees of freedom and generating higher-order modulated signals. The upgraded design generated 64-QAM signals; however, the complexity and cost to achieve that were high. It needed 12 variable terminating loads to produce 64-QAM signals. In addition to that, having a three-way power divider at the output of the four ports of the correlator added

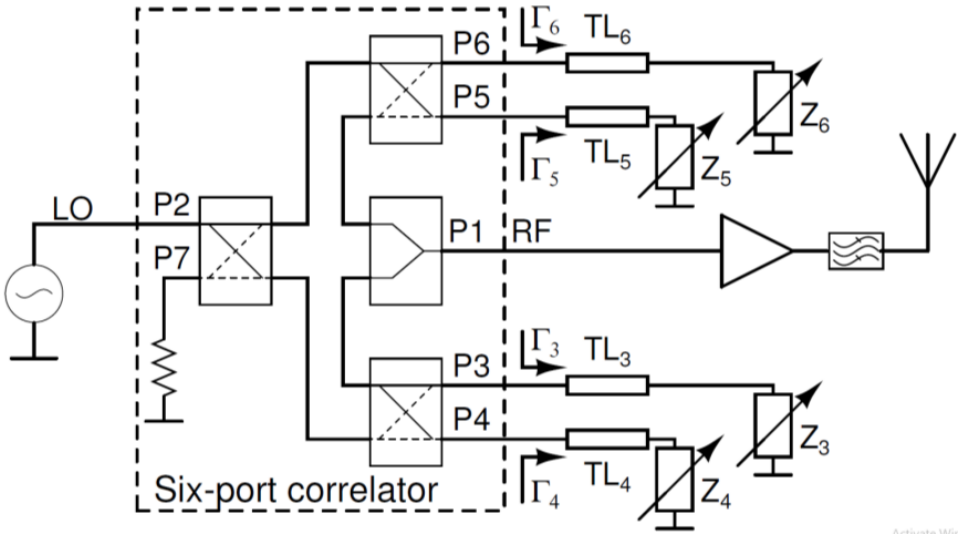

Figure 2.7: Schematic of a 16-QAM six-port modulator. Adapted from [67].

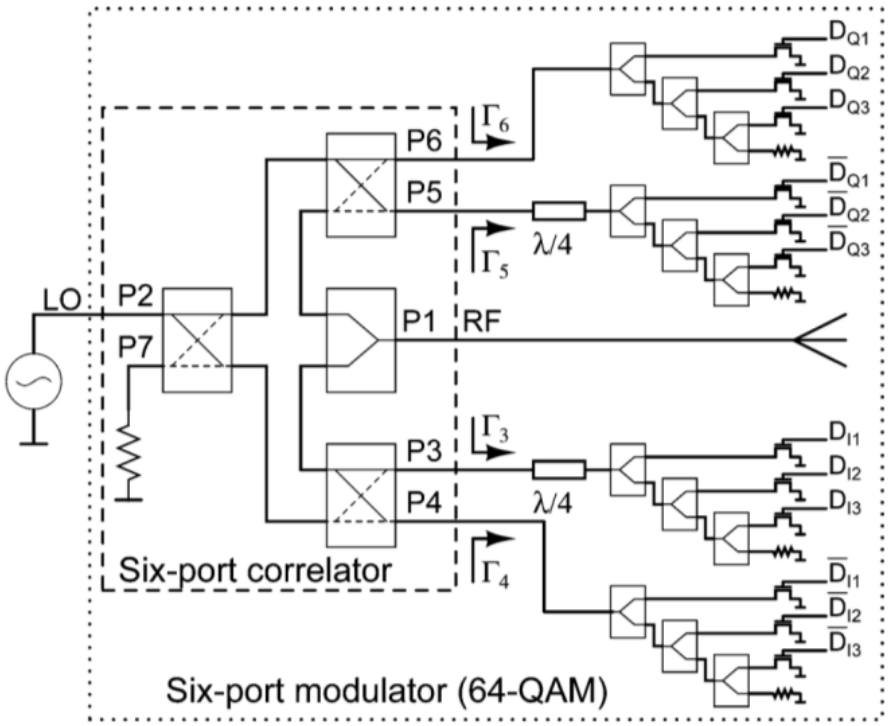

Figure 2.8: Schematic of a 64-QAM six-port modulator. Adapted from [72].

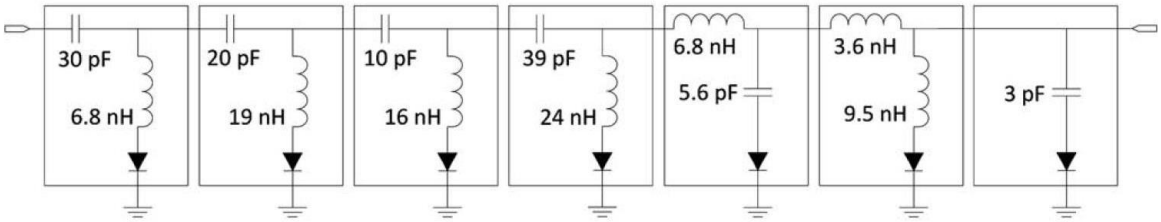

Figure 2.9: Schematic design of a load-modulated tunable matching network. Adapted from [73].

significant complexity to the overall design.

The use of load modulators was not limited to the generation of M-QAM signals and analog beamformers. In [73] a digitally controlled, tunable matching network was presented. The design consists of serially connected two-element L-section grounded through PIN diodes, as shown in Fig. 2.9. Each L-section consists of capacitors, inductors, and a PIN diode that provides tunability. Upon careful selection of the values of the lumped elements through an optimization process and depending on the PIN diodes state, a tunable matching network is realized, allowing for nearly 66% coverage of the Smith chart.

Progress in the area of massive antenna array architectures with reduced front-end hardware complexity was reported in [74]–[78]. For example, a novel load-modulated single-RF (LMSRF) MIMO transmitter was presented in [77], [78]. It comprises a single power amplifier connected directly to a set of antenna elements through load modulators without requiring a mixer and a DAC. Data modulation on the antennas was performed using adjustable PIN-diode-based load modulators that controlled the input voltages of the antenna, as depicted in Fig. 2.10. The proposed transmitter showed great potential in supporting arbitrary types of modulation.

Further progress in the area of load modulated arrays was reported in the literature. For example, the work in [79] investigated random phase modulation that improved performance when used in load-modulated antennas. Other recent works use the load modulated array framework to implement multi-user precoding techniques in the baseband suitable for large antenna arrays [80]–[83]

The scope of this dissertation is confined to the hardware architecture of load-modulated transmitters. The transmitter reported in [77], [78] was only simulated and did not progress into actual prototyping, nor did it address practical measurement challenges. Furthermore, each of the RF switches embedded in the load modulator circuitry consists of two PIN diodes, which add to the cost and the complexity of the load modulator circuit in the case of

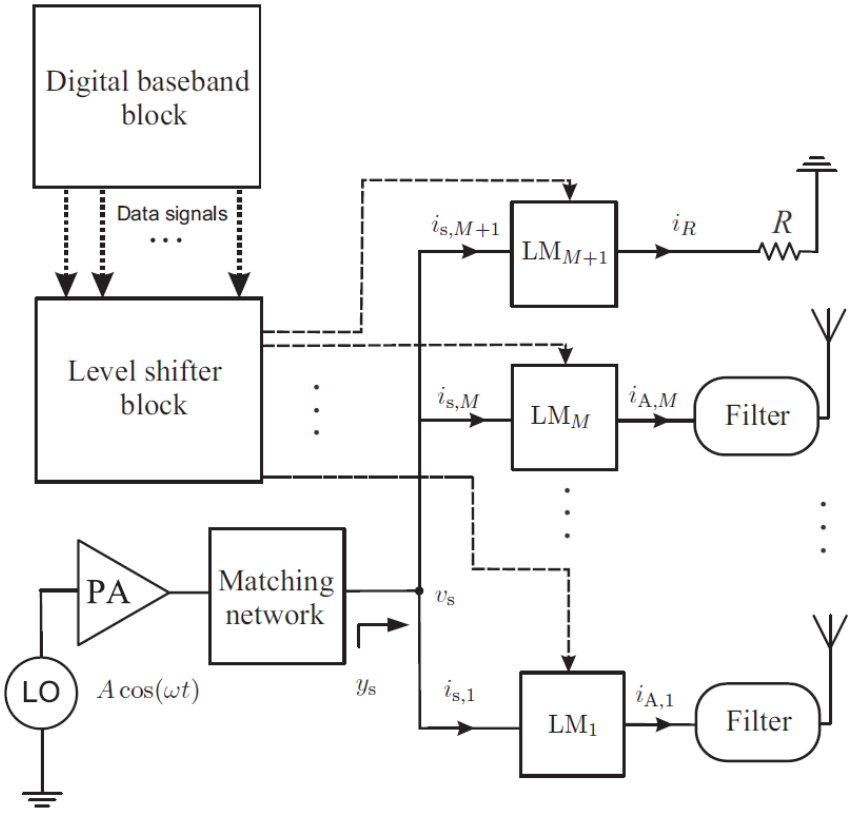

Figure 2.10: Architecture of the LMSRF MIMO transmitter. Adapted from [78].

prototyping considerations. Earlier work on load-modulated I/Q transmitters did not fully cover details in the design procedure and did not address manufacturing and measurement challenges. This dissertation aims to provide a comprehensive roadmap for designing, implementing, and measuring a low-cost, low-profile, and energy-efficient 64-QAM load modulator. Additionally, this work addresses reducing the hardware complexity by introducing a low-cost, simple, and easy-to-manufacture switching system embedded in the load modulator circuit.

2.6 Conclusion

This chapter presented a general system model for the MU-MIMO system. The concept of massive MIMO was also presented. Next, some existing issues in small-scale MIMO systems were discussed and how these issues become critical in massive MIMO. The available solutions in the literature were presented.

Chapter 3

Design of a Low-Cost Low-Profile Energy Efficient 64-QAM Load Modulator

This chapter presents the design of a 64-QAM I/Q modulator based on load modulation. The modulator is designed to operate at 3 GHz. In any standard M-QAM modulation, the RF circuitry of the voltage source generates currents on the antenna corresponding to the transmitted signals. With load modulation, the waveforms of the M-QAM constellation points are generated by changing the impedance parameters of the load modulator connected to the antenna. At the same time, the voltage source is kept constant. Thus, the power amplifier amplifies a constant signal and does not need to operate in the back-off region. An optimization algorithm is developed to find the design parameters of the load modulator circuit. The design parameters obtained from the algorithm have been used in the Advanced Design System (ADS) software to design, simulate, and fully characterize the RF load modulator circuit. The hardware prototype of the load modulator circuit is realized using microstrip lines and a diode-based switching circuit. The measurements show that the load modulator can generate outputs on the S_{21}-parameter complex plane matched to the 64-QAM constellation diagram. A microcontroller is programmed to provide the required bias voltages to the PIN diodes in the load modulator based on a predetermined lookup table (LUT). The proposed architecture does not require a digital-to-analog converter (DAC). A credible agreement between the simulation results and measurements is obtained. This modulator shows great potential in integration with load-modulated MIMO transmitters. Antenna elements will be driven by these load modulators, eliminating the need for a dedicated RF chain per antenna, which make it ideal for alleviating the challenges associated with massive MIMO systems.

3.1 Block Structure of the Reduced-Complexity Load-Modulated 64-QAM Modulator

The RF circuitry of the load-modulated 64-QAM modulator consists of a local oscillator (LO) generating a sinusoidal wave with a constant amplitude. The LO is followed by a Class-F PA that amplifies a constant envelope. An isolator is connected to the output port of the PA to protect it from any power reflections in the system. The antenna is connected to the RF circuit through a load modulator. The load modulator is a two-port network that contains tunable components (e.g., PIN diodes or varactors). The modulated signals on the antenna (the I and Q components of the QAM signals) are generated by varying the impedance of the load modulator. A filter is used to limit the spectral bandwidth on the antenna to the desired frequency range. A programmable microcontroller generates the required bias voltages for the active components of the load modulator based on a lookup table (LUT) that contains mapping data. This modulator does not require a mixer nor a DAC. Hence, it is simpler, less complicated, cheaper, and more efficient than conventional voltage-modulated RF transmitters. Fig. 3.1 shows the reduced-complexity load-modulated 64-QAM modulator.

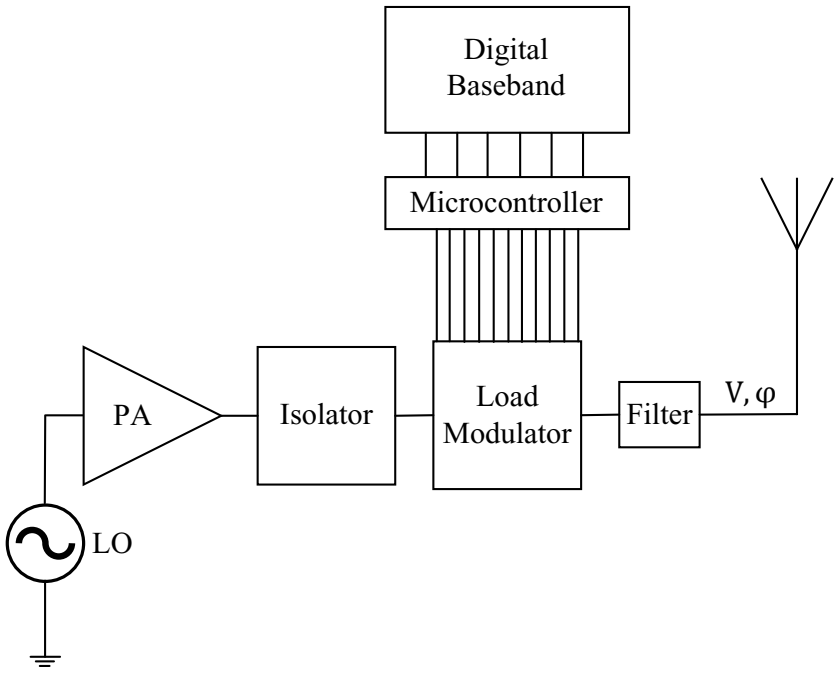

Figure 3.1: Block diagram of the reduced-complexity load-modulated 64-QAM Modulator.

3.1.1 Theoretical analysis

To explain the idea of the load-modulated RF transmitter, a simple circuit model is considered, as shown in Fig. 3.2. It consists of a sinusoidal voltage

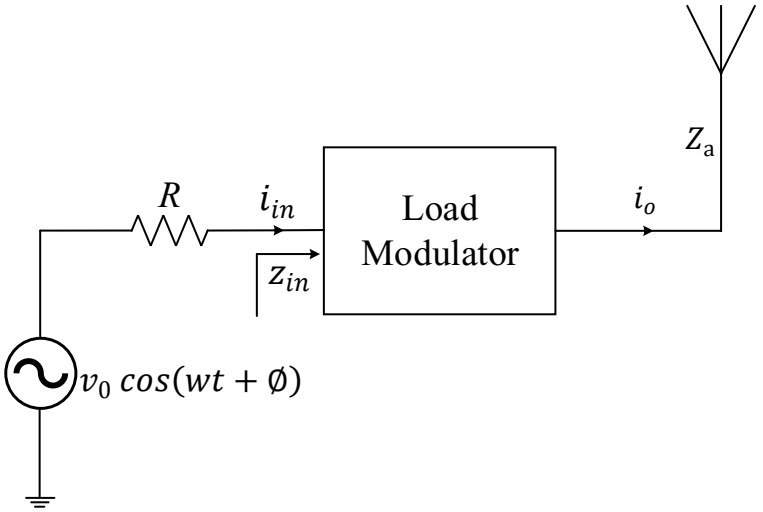

Figure 3.2: Circuit model of the load-modulated RF transmitter.

source with its internal resistance R connected to the antenna through a two-port load-modulator network. A load impedance of Z_a represents the input impedance of the antenna. The idea is to change the input impedance of the load modulator to get the desired current i_o at the input of the antenna while the power source is supplying a fixed input voltage $v_0 cos(wt + \phi)$. The complex phasor I_o representing the output current i_o can be set arbitrarily in the complex plane on a circle with a radius determined by the maximum power of the source. The output current's phasor I_o is a function of the impedance parameters (Z_{11}, Z_{12}, Z_{21}, Z_{22}) of the two-port load modulator network. The phasor I_{in} representing the input current i_{in} is given by

$$I_{in} = \frac{V_0 e^{j\angle\phi}}{R + Z_{in}} \tag{3.1}$$

where V_0 is the peak voltage of the source and Z_{in} is the input impedance of the two-port load-modulator network, which is given by

$$Z_{in} = Z_{11} - \frac{{Z_{12}}^2}{Z_a + Z_{22}} \tag{3.2}$$

Equivalently, the output impedance of the proposed two-port network is given by

$$Z_{out} = Z_{22} - \frac{{Z_{12}}^2}{R + Z_{11}} \tag{3.3}$$

The output current's phasor I_o is given by

$$I_0 = \frac{Z_{12}}{Z_a + Z_{22}} I_{in} = \frac{Z_{12}}{Z_a + Z_{22}} \frac{V_0 e^{j\angle\phi}}{R + Z_{in}} \tag{3.4}$$

Since part of the supplied power is consumed by the resistor R and the remaining power is delivered to the load modulator circuit, the power equation can be written as

$$\frac{1}{2}\left[V_0 * {I_{in}}^*\right] = \frac{1}{2}\left[R * |I_{in}|^2 + \Re(Z_{in}) * |I_{in}|^2\right] \tag{3.5}$$

The maximum power transfer is achieved when the source impedance R is matched to the input impedance of the load modulator ($R = \Re(Z_{in})$). Hence, the maximum output current can be written as

$$I_o(max) = \frac{V_0}{2\sqrt{R}\sqrt{\Re(Z_{in})}} \tag{3.6}$$

An example of a two-port load modulator network, shown in Fig. 3.3, is chosen to clarify the concept through numerical analysis.

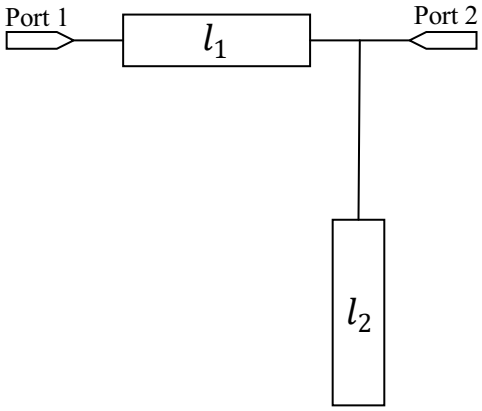

Figure 3.3: Schematic of an L-section two-port network.

It consists of two transmission lines l_1 and l_2 forming an L-section network. The L-section topology is chosen since it is easier to fabricate and analyze. The ABCD parameters of the L-section network are obtained by the direct multiplication of the ABCD parameters of the line l_1 and the ABCD parameters of the open-circuit stub l_2. For simplicity, the lines l_1 and l_2 are assumed to be lossless. The final ABCD parameters of the L-section network is given by

$$\begin{bmatrix} A & B \\ C & D \end{bmatrix} = \begin{bmatrix} A & B \\ C & D \end{bmatrix}_{l_1} \begin{bmatrix} A & B \\ C & D \end{bmatrix}_{l_2} = \\ \begin{bmatrix} cos(\beta l_1) & Z_0 sin(\beta l_1) \\ Y_0 sin(\beta l_1) & cos(\beta l_1) \end{bmatrix} \begin{bmatrix} 1 & 0 \\ Y_0 tan(\beta l_2) & 1 \end{bmatrix} \tag{3.7}$$

where $\beta = 2\pi/\lambda$ is the propagation constant at the frequency of interest, Z_0, and Y_0 are the characteristic impedance and the characteristic admittance of

the transmission line, respectively. As can be deduced, the ABCD parameters of the L-section network depend on the lengths l_1 and l_2. Consequently, the S_{21} parameter of the L-section network also depend on the lengths l_1 and l_2. The S_{21} parameter of a two-port network can be deduced from the ABCD parameters through the following equation [84]

$$S_{21} = \frac{2}{A + B/Z_0 + CZ_0 + D} \tag{3.8}$$

It can be shown numerically that any value of the transmission parameter S_{21} can be achieved on the S_{21} complex plane by varying the lengths l_1 and l_2. Fig. 3.4 shows the numerical result of the S_{21} parameters of the L-section network for various values of l_1 and l_2 between 0 and $\lambda/2$. It can be observed that the S_{21} complex plane can be fully covered when l_1 and l_2 are swept through a large sample size of values between 0 and $\lambda/2$.

3.2 Load Modulator Circuit Model and Design Method

In this work, the proposed load modulator circuit is based on the serial concatenation of the L-section cells in Fig. 3.5. Each L-section consists of a microstrip transmission line, a PIN diode, and an open-circuited shunt stub. The PIN diode controls the physical length of the open-circuited shunt stub based on its OFF/ON state. The schematic of the primary single L-section cell is depicted in Fig. 3.5.

3.2.1 RF switch

RF and microwave switches are critical elements in microwave systems as they control the path of RF signals between instruments and devices. Moreover, they allow many tests to be conducted within the same setup without circuit alteration. In this work, the M/A-COM MA4AGBLP912 PIN diode has been employed in each L-section cell as a switching element to control the physical length of the open-circuited shunt stub. This PIN diode is characterized by its low resistance (4 Ω), low capacitance (28 fF), and extremely fast switching speed of (5 ns). The ultra-low junction capacitance C_f makes it suitable to operate at up to 40 GHz when used in the shunt configuration. The low profile of the PIN diode makes it suitable to be utilized in microwave switch designs, where low insertion loss and high isolation are necessities. The PIN diode has been biased using +/-5Vdc bias signals. However, according to the datasheet, this PIN diode can be forwardly biased by biasing voltages equal, or more, than 1.2 V. The RF switch has been designed, simulated, and fabricated on a 1.27 mm Rogers TMM 10i substrate with a dielectric constant of 9.9, as shown in Fig. 3.6.

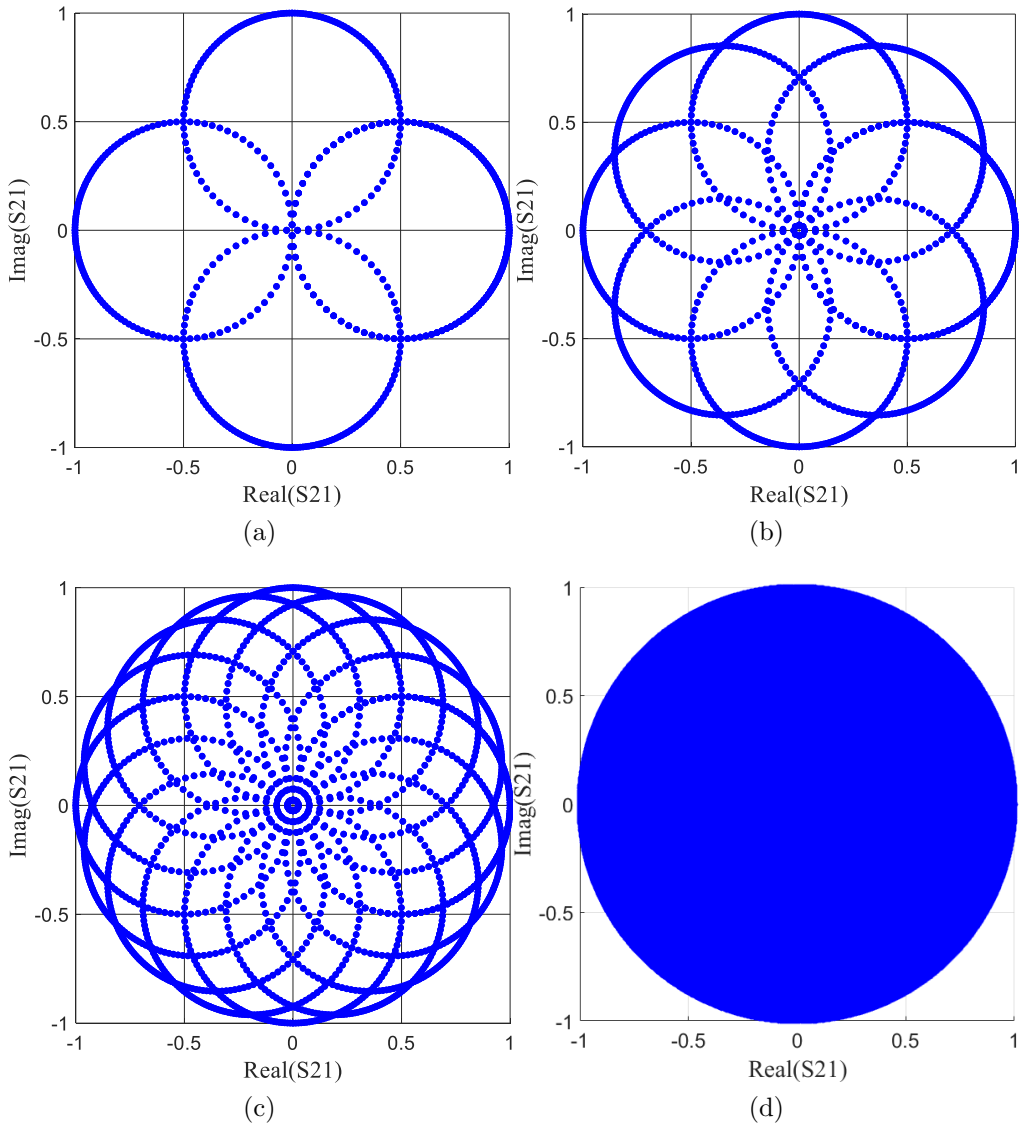

Figure 3.4: The numerical values of the transmission parameter S_{21} at the output of the L-section network when l_1 and l_2 are varied between 0 and $\lambda/2$. a) 4 unique values of l_1 and 2500 unique values of l_2. b) 8 unique values of l_1 and 2500 unique values of l_2. c) 16 unique values of l_1 and 2500 unique values of l_2. d) 2500 unique values of l_1 and 2500 unique values of l_2.

The switch is fabricated using microstrip transmission lines and lumped elements. The bias circuit consists of a series capacitor $C = 80\ pF$ at port 1 acting as a DC blocker and a short-circuited quarter-wavelength shunt stub at port 2 acting as an RF choke and controlling the frequency response of the switch around the frequency of interest, 3 GHz.

As shown from the layout of the switch, the quarter-wavelength shunt stub is curved for fabrication considerations and the space constraint when incorporating the switch later on in the load modulator circuit design. An

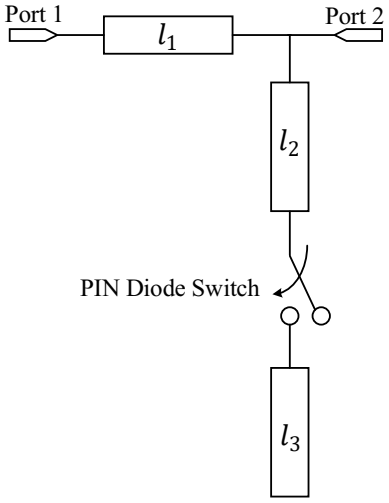

Figure 3.5: Simplified schematic of a single reconfigurable L-section unit cell.

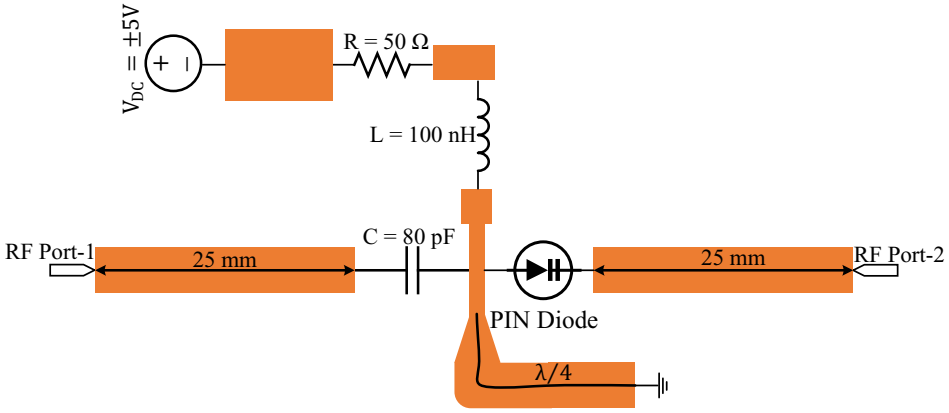

(a)

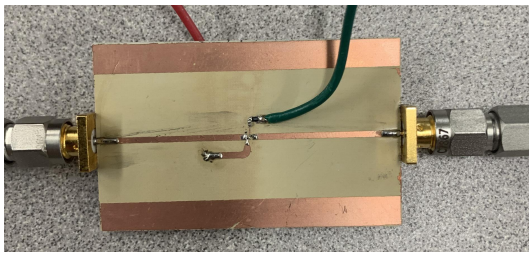

(b)

Figure 3.6: RF switch. a) Schematic design of the switch and its bias circuit. b) Fabricated prototype of the same switch.

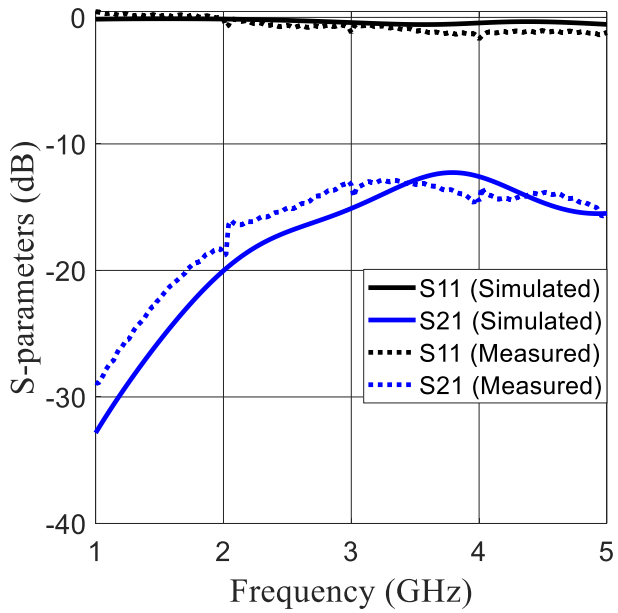

Figure 3.7: S-parameters of the RF switch when it is open (OFF state).

inductor $L_1 = 100\ nH$ is in series with the *dc* voltage source acting as an RF blocker and only passes *dc* signals to bias the PIN diode.

The proposed RF switch is designed and simulated in momentum ADS. The performance of the proposed RF switch is shown in Figs. 3.7 and 3.8. An ideal RF switch acts as an open circuit in the OFF state. Fig. 3.7 shows the performance of the switch in its OFF state. It can be observed that S_{11} is -0.4 dB, while S_{21} is -16 dB at the frequency of interest, 3 GHz. The proposed RF switch is then fabricated and measured. Measurement of the switch in the OFF state shows a credible agreement with the simulation performance. Compared to the simulation performance in the OFF state, the measured S_{11} at 3 GHz is -1 dB while the measured S_{21} is -14 dB. The performance of the switch in the ON state is shown in Fig. 3.8. An ideal RF switch will act as a short circuit when it is in the ON state. Fig. 3.8 shows that the reflection coefficient S_{11} at port 1 is -21 dB while the insertion loss S_{21} is -0.15 dB at 3 GHz. Again, measurement shows a credible agreement with the simulation performance. Compared to the simulation performance in the ON state, the measured S_{11} at 3 GHz is -20 dB while the measured S_{21} is -1 dB.

The simulated switching speed of the proposed RF switch is shown in Fig. 3.9. The transient output voltage of the switch is shown in Fig. 3.9(a) when switched from OFF to ON. It can be seen that the reverse to forward switching time is 0.003 μs. The transient output voltage of the switch is shown in Fig. 3.9(b) when switched from ON to OFF. It can be seen that the forward to reverse switching time is 0.006 μs.

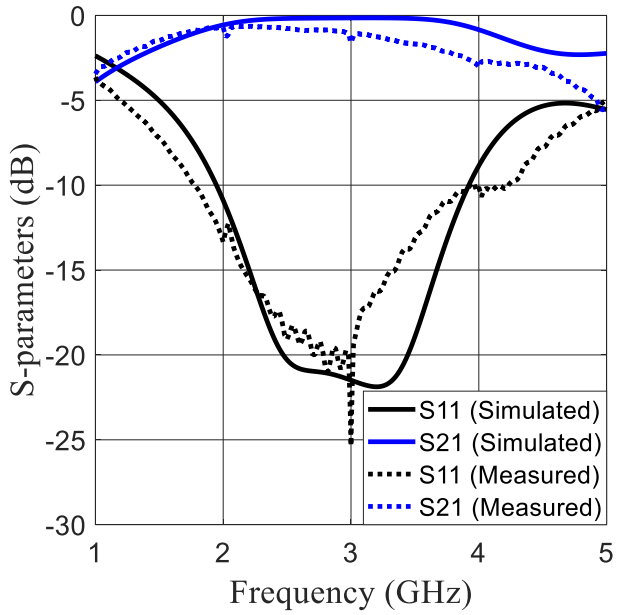

Figure 3.8: S-parameters of the RF switch when it is closed (ON state).

The RF switch will be placed in the shunt branch of the L-section cell, as depicted in Fig. 3.5. Hence, the L-section cell will have two different states depending on the bias condition of the PIN diode. By scaling the load modulator circuit based on the repetition of N number of L-section cells, the number of different states of the final load modulator will be 2^N.

3.2.2 Load modulator circuit design

The final load modulator circuit is realized by the serial concatenation of the previously-described L-section cells, as shown in Fig. 3.10.
Each L-section cell can be characterized by its ABCD transmission parameters. Each cell has two possible ABCD matrices corresponding to the selected switch state. For example, the ABCD matrix of cell 1 of the circuit in Fig. 3.10, when the switch is in the OFF state, is given by the product of the ABCD parameters of the transmission line $l_{1\text{-}1}$ and the ABCD parameters of the shunt stub $l_{2\text{-}1}$

$$\begin{bmatrix} A & B \\ C & D \end{bmatrix} = \begin{bmatrix} A & B \\ C & D \end{bmatrix}_{l_{1\text{-}1}} \begin{bmatrix} A & B \\ C & D \end{bmatrix}_{l_{2\text{-}1}} = \tag{3.9}$$

$$\begin{bmatrix} cosh(\gamma l_{1\text{-}1}) & Z_0 sinh(\gamma l_{1-1}) \\ Y_0 sinh(\gamma l_{1\text{-}1}) & cosh(\gamma l_{1-1}) \end{bmatrix} \begin{bmatrix} 1 & 0 \\ Y_0 tanh(\gamma l_{2\text{-}1}) & 1 \end{bmatrix}$$

where $\gamma = \alpha + j\beta$ is the complex propagation constant and Z_0, Y_0 are the characteristic impedance and the characteristic admittance of the transmission line, respectively.

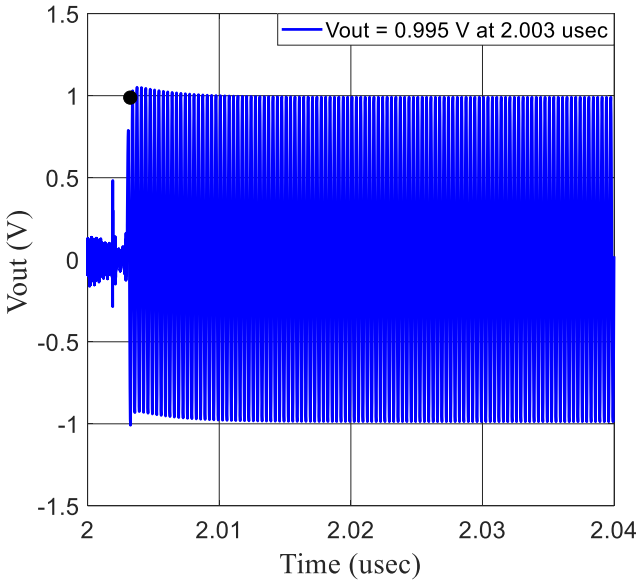

(a)

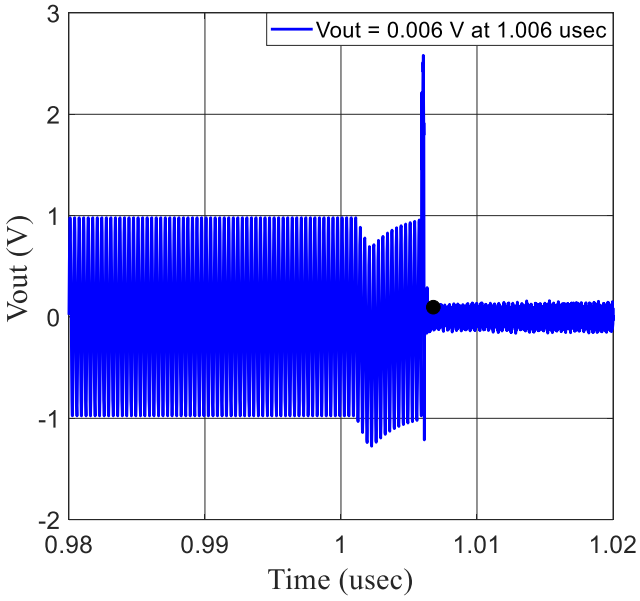

(b)

Figure 3.9: Switching speed (simulated) of the RF switch. a) Rise time of the RF switch when biased reverse to forward (OFF to ON state). b) Fall time of the RF switch when biased forward to reverse (ON to OFF state)

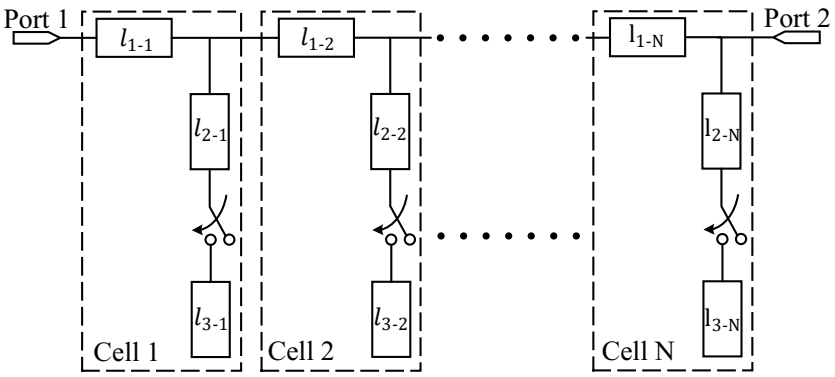

Figure 3.10: Simplified schematic of the load modulator based on N number of L-section cells.

The ABCD matrix of cell 1 when the switch is in the ON state is given by the product of the ABCD parameters of the transmission line $l_{1\text{-}1}$ and the ABCD parameters of the shunt stub $l_{2\text{-}1} + l_{3\text{-}1}$

$$\begin{bmatrix} A & B \\ C & D \end{bmatrix} = \begin{bmatrix} A & B \\ C & D \end{bmatrix}_{l_{1\text{-}1}} \begin{bmatrix} A & B \\ C & D \end{bmatrix}_{l_{2\text{-}1}+l_{3\text{-}1}} = \tag{3.10}$$

$$\begin{bmatrix} cosh(\gamma l_{1\text{-}1}) & Z_0 sinh(\gamma l_{1\text{-}1}) \\ Y_0 sinh(\gamma l_{1\text{-}1}) & cosh(\gamma l_{1\text{-}1}) \end{bmatrix} \begin{bmatrix} 1 & 0 \\ Y_0 tanh(\gamma(l_{2\text{-}1} + l_{3\text{-}1}) & 1 \end{bmatrix}$$

The critical advantage of transmission matrices is that the concatenation of many L-section cells will be the direct multiplication of the arrays. For example, assuming that the load modulator circuit comprises an N number of L-section cells, there will be 2^N different possible transmission matrices. Once all possible transmission matrices are obtained, the transformation into S-parameters is straightforward and can be calculated based on [84].

3.3 Circuit Optimization

The optimization process of the load modulator circuit is as follows. For a load modulator circuit constructed based on the repetition of N number of L-section cells (see Fig. 3.10), this circuit has 2^N different states. The switching element in each L-section cell has only two possible states (ON or OFF state). As shown in Fig. 3.10, the number of microstrip transmission line lengths that need to be optimized is $3 \times N$, where N is the number of L-section cells that constitute the final load modulator circuit. For practical design considerations and to minimize the optimization processing complexity, the space of possible values of the physical length of these lines is selected between $\lambda_g/10$ to $\lambda_g/2$, where λ_g is the guided wavelength at 3 GHz. Since all the 2^N possible states of the load

modulator circuit will be examined in the optimization process, the complexity of the problem grows exponentially as N, the number of L-section cells, grows. However, the number of optimization variables grows linearly as N increases. The goal is to find the best physical lengths of the lines ($l_{1\text{-}1}$ to $l_{3\text{-}N}$) of the load modulator. The final load modulator circuit should generate outputs that can be mapped to the theoretical 64-QAM constellation diagram. The optimization problem is nonlinear. The sample size of all possible solutions is a vector of size $[0.4\lambda_g/\text{Step Size}]^{3N}$.

As can be deduced, this sample size is a function of the number of the L-section cells N and the step size chosen between $\lambda_g/10$ to $\lambda_g/2$. The processing time required to solve the problem by evaluating all possible solutions using the brute force method is not feasible since the vector size of all possible solutions is huge. Moreover, for any moderately large number of cells (e.g., $N = 4$ or more), the vector of possible solutions cannot be evaluated readily. The work in [78] attempted to use a genetic algorithm (GA) to find a sub-optimal solution for the problem. GA is a heuristic search algorithm useful in finding an approximate global optimum of an optimization problem. However, the design parameters of the load modulator circuit obtained by the GA in [78] did not yield the generation of constellations resembling QAM constellation diagrams, and large parts of the S_{21} complex plane were uncovered. In this work, another evolutionary computational algorithm, the differential evolution algorithm (DEA), has been implemented using the optimization toolbox in MATLAB to solve this nonlinear problem [85]. The DEA is a population-based algorithm that optimizes a problem by repeatedly trying to improve a candidate of solutions based on an evolutionary process [86]. Like the GA, the DEA is a meta-heuristic search algorithm that does not guarantee an optimal solution to an optimization problem. However, DEA is more tailored to solve numerical optimization problems like this one since the goal here is to find the physical line lengths of the microstrip-based load modulator circuit. The main parameters of the algorithm are summarized in Table 3.1. A flow chart

Table 3.1
DEA optimization parameters

Parameter	**Value**
Population Size	20
Population generation	Uniform
Crossover Rate	0.6
Mutation Rate	0.4
No. of Iterations	5000

indicating the optimization process and the steps to find the solution is shown in Fig. 3.11.

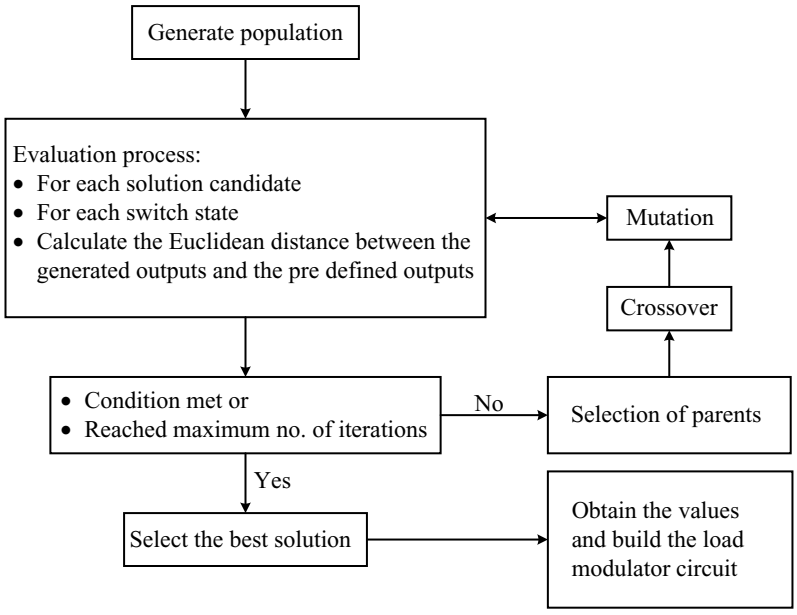

Figure 3.11: Flow chart of the DEA used to find the design parameters of the load modulator.

The aim is to design a load modulator circuit that generates outputs that match the ideal 64-QAM constellations on the S_{21} complex plane. It has been discovered that a load modulator with eleven L-section cells ($N = 11$) is needed to generate outputs with minimal deviation from the ideal 64-QAM constellation locations. Having eleven stages of the L-section cells in the load modulator allows more degrees of freedom in the optimization process. The schematic of an eleven-stage load modulator circuit is shown in Fig. 3.12.

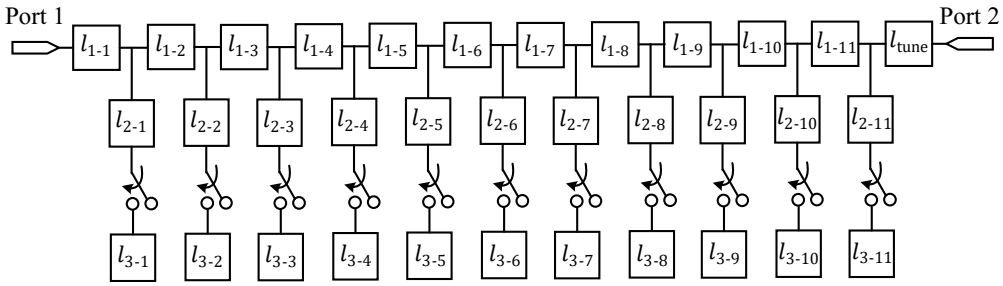

Figure 3.12: Schematic of the load modulator circuit based on eleven L-section cells.

The number of optimization elements is ($3 \times 11 = 33$). Specifically, the line lengths ($l_{1\text{-}1}$ to $l_{3\text{-}11}$). The additional fixed-length l_{tune} is added to the structure of the load modulator for practical design considerations and phase correction, as will be discussed later. The number of the states of this load modulator circuit is $2^{11} = 2048$. Since there are 2048 different states of the circuit, there is a possibility to generate 2048 different outputs. Each candidate solution is

a vector of $3 \times 11 = 33$ and a potential solution for the problem. The purpose of the optimization algorithm is to find the best values for ($l_{1\text{-}1}$ to $l_{3\text{-}11}$) that can guarantee to generate outputs on the S_{21} complex plane at the exact location as those of the ideal 64-QAM constellation. The fitness function in the DEA is the most crucial part of the optimization process. First, the transmission line lengths ($l_{1\text{-}1}$ to $l_{3\text{-}11}$) will be selected arbitrarily to generate all 2048 possible S_{21} outputs at the output port of the load modulator. Second, a pre-defined modulation scheme will be chosen (e.g., 64-QAM). It is important to emphasize that the number of degrees of freedom should be higher than the minimum required number of switches for the targeted modulation scheme. For example, to support 64-QAM modulation, it theoretically requires the serial concatenation of six L-section cells, where the load modulator circuit can potentially generate $2^6 = 64$ outputs. That means that at least six RF switches are needed in the structure of the load modulator. However, having only six RF switches will not practically lead to load modulator outputs at the desired locations on the S_{21} complex plane due to the limited degrees of freedom in the circuit. Therefore, more RF switches than this bare minimum should be embedded in the circuit to generate a larger sample size of possible outputs. For this reason, the number of L-section cells needed in the structure of the load modulator must be higher than the modulation order. For example, eleven L-section cells (eleven RF switches) have been used in the load modulator structure to generate enough outputs. You can guarantee that the load modulator circuit generates a unique output for each ideal 64-QAM constellation point. The resulting S_{21} outputs on the complex plane are obtained. For each point in the ideal pre-defined 64-QAM modulation, the closest constellation point (S_{21}) generated by the algorithm is found. At each step of the optimization process, the transmission line lengths will be updated until the Euclidean distance between the outputs generated by the load modulator and the pre-defined 64-QAM modulation is minimized. The minimized value R is the summation of this Euclidean distance squared for each point in the ideal constellation. It can be represented as:

$$R = \sum_{i=1}^{64} = |{S_{21}}^{i} - {\hat{S}_{21}}^{i}|^2 \tag{3.11}$$

where S_{21} is the complex value of the ideal 64-QAM constellation point, and $\hat{S}_{21}$ is the complex value of the constellation point generated by the load modulator. The algorithm converges when the successful solution has a unique switch state for the load modulator that generates an output that can be mapped to each point in the constellation diagram of the pre-defined 64-QAM modulation. The line lengths ($l_{1\text{-}11}$ to $l_{3\text{-}11}$) of the load modulator are determined after the convergence of the algorithm. After obtaining the design parameters, these parameters were plugged into the Advanced Design System (ADS) software to design, simulate, and fully characterize the load modulator circuit.

The load modulator circuit is designed on Rogers TMM 10i substrate with the following parameters.

- Substrate Height $H = 1.27mm$
- Dielectric Constant $\epsilon_r = 9.9$
- Conductor Cladding $T = 35\mu m$
- Dielectric Loss $\delta_d = 0.002$

The layout design of the final load modulator circuit is shown in Fig. 3.13. The design parameters of the load modulator are given in Table 3.2.

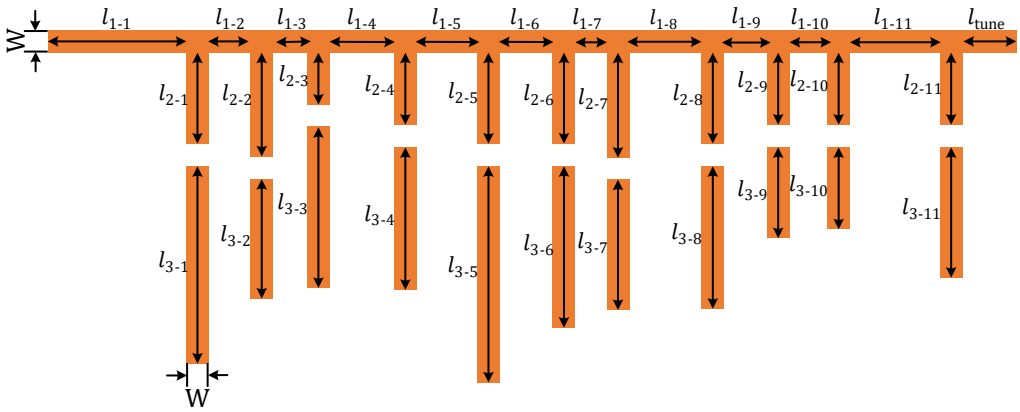

Figure 3.13: Layout of the eleven-stage load-modulator circuit.

3.4 Simulation Results

After obtaining the circuit design parameters from the DEA implemented in MATLAB and applying them in the ADS momentum simulation, the generated circuit outputs have slightly deviated from the computed circuit outputs. It can be attributed to the different methodology the ADS solver uses when computing electromagnetic fields. Therefore, another minor fine-tuning stage of the line lengths of the load modulator was performed in ADS. Fig. 3.14 shows the simulated 64-QAM constellations at 3 GHz, generated by six, seven, eight, nine, ten, and eleven L-section stages in the load modulator circuit.
It can be observed from Fig. 3.14 that by increasing the number of stages in the load modulator circuit, the error between the ideal 64-QAM constellations and the constellations generated by the load modulator circuit is minimized. A figure of merit, like the error vector magnitude (EVM), is defined to quantify this error. The EVM at the transmitter measures the error between the ideal constellation points and the constellations generated by the load modulator

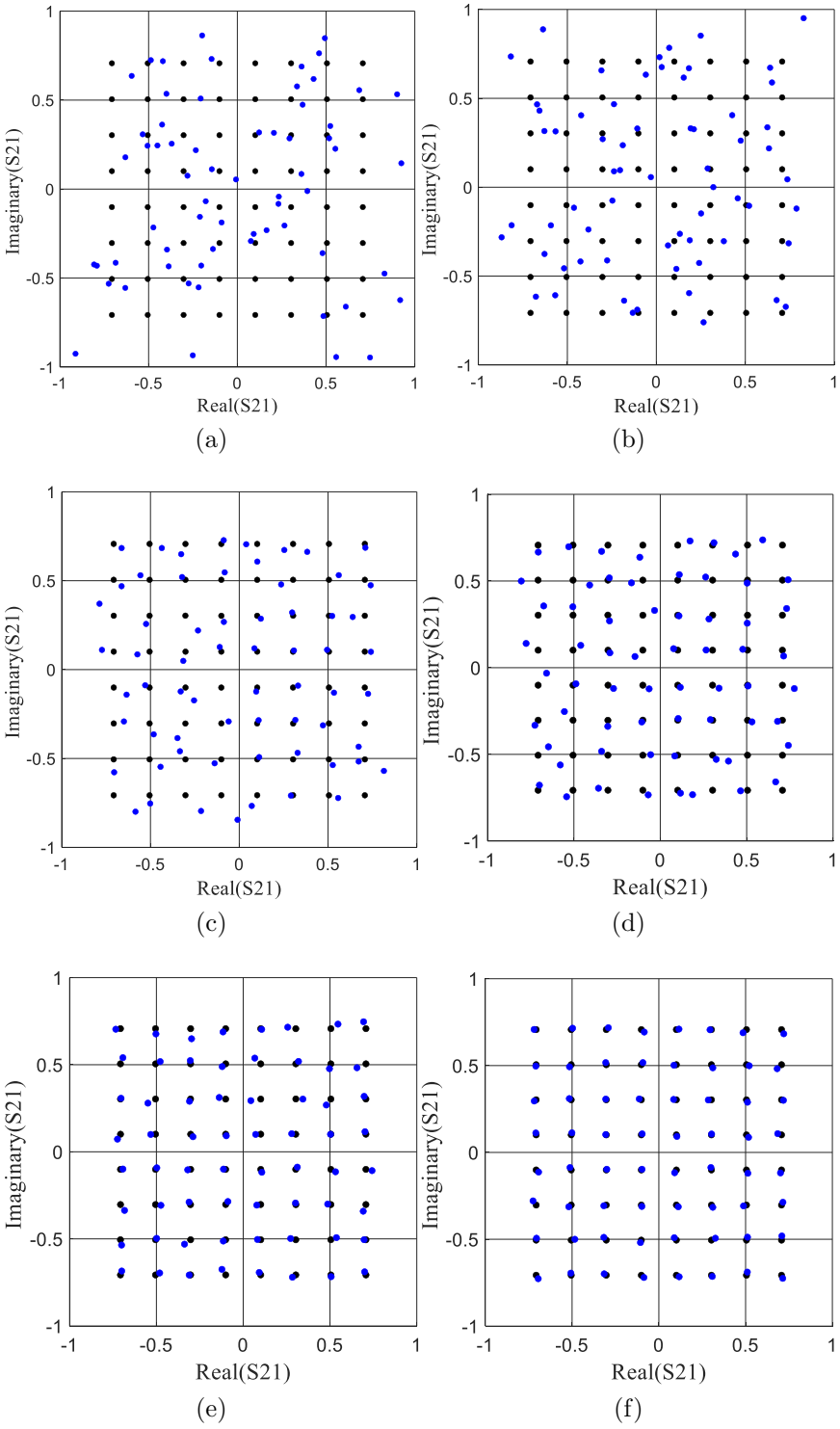

Figure 3.14: Comparison between the ideal 64-QAM constellations (black dots) and the simulated constellations generated by the load modulator circuit (blue dots) at 3 GHz. (a) Six-stage load modulator. (b) Seven-stage load modulator. (c) Eight-stage load modulator. (d) Nine-stage load modulator. (e) Ten-stage load modulator. (f) Eleven-stage load modulator.

Table 3.2
Design parameters of the load modulator circuit

Parameter	**Value [mm]**	**Parameter**	**Value [mm]**
W	1.2	$l_{3\text{-}6}$	11.7
$l_{1\text{-}1}$	14.7	$l_{1\text{-}7}$	2.2
$l_{2\text{-}1}$	7.2	$l_{2\text{-}7}$	4.1
$l_{3\text{-}1}$	15.6	$l_{3\text{-}7}$	9.2
$l_{1\text{-}2}$	3.8	$l_{1\text{-}8}$	7.7
$l_{2\text{-}2}$	8.1	$l_{2\text{-}8}$	6.1
$l_{3\text{-}2}$	7.1	$l_{3\text{-}8}$	11.2
$l_{1\text{-}3}$	3.6	$l_{1\text{-}9}$	3.0
$l_{2\text{-}3}$	4.5	$l_{2\text{-}9}$	4.8
$l_{3\text{-}3}$	12.1	$l_{3\text{-}9}$	10.3
$l_{1\text{-}4}$	9.6	$l_{1\text{-}10}$	2.0
$l_{2\text{-}4}$	5.1	$l_{2\text{-}10}$	5.1
$l_{3\text{-}4}$	10.6	$l_{3\text{-}10}$	7.9
$l_{1\text{-}5}$	7.3	$l_{1\text{-}11}$	12.4
$l_{2\text{-}5}$	6.5	$l_{2\text{-}11}$	4.9
$l_{3\text{-}5}$	16.3	$l_{3\text{-}11}$	9.8
$l_{1\text{-}6}$	5.1	l_{tune}	4.0
$l_{2\text{-}6}$	6.1		

circuit. Fig. 3.15 shows the simulated EVM as a function of the number of stages in the load modulator circuit.
It can be observed that the EVM decreases as the number of the unit cell stages in the load modulator circuit increases. Fig. 3.16 shows the S_{21} magnitude and phase over a frequency range of 1 GHz for all 64-QAM outputs generated by the eleven-stage load modulator. It can be observed that S_{21} remains reasonably constant over a significant frequency range around the operating frequency, 3 GHz.

Fig. 3.17 shows the constellations generated by the eleven-stage load modulator at four different frequencies around the center frequency, 3 GHz. It can be observed that the generated constellations strongly resemble the reference 64-QAM constellation diagram.

The load modulator works as follows. First, each symbol in the digital baseband domain will be mapped to one of the pre-defined 64-QAM constellations. The microcontroller will then find the unique switch state corresponding to this digital symbol through its lookup table and serve the proper biasing voltages to the RF switches in the load modulator circuit. The desired wave-

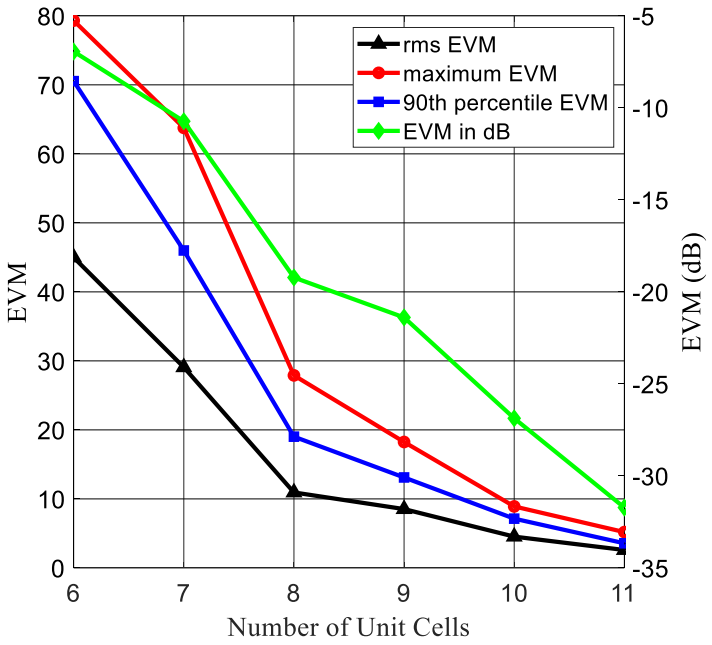

Figure 3.15: EVM as a function of the number of L-section unit cells implemented in the load modulator circuit.

forms representing the digital constellation will be generated at the output of the load modulator, hence, at the input of the antenna. Since the waveforms are generated by configuring the load, the PA in the RF front-end always amplifies a fixed-amplitude input signal and does not have to be linear. Thus, it can be a Class-F PA with an efficiency of 80%. With clipping considerations, the efficiency of the Class-F PA can drop to 70%. Table 3.3 summarizes some of the related works in the literature and compares efficiency with the work in this dissertation.

It can be observed that the proposed 64-QAM load modulator supports a higher modulation order compared to the works in [64], [65], [69], and [78]. The work in [72] is similar to the presented work in this thesis regarding the constellation size, the reported EVM, and the reported efficiency. However, the work in [72] utilized 12 switches to generate 64-QAM outputs. Moreover, the design complexity is higher in [72], as the modulator consists of two stages; a six-port correlator followed by four three-way Wilkinson power dividers leading to a higher profile and increased circuit size.
The final prototype of the eleven-stage load modulator is realized using microstrip lines and switches. Fig. 3.18 shows the fabricated version of the load modulator circuit, including 11 switches.

Measurements of the transmission parameter S_{21} corresponding to the 64-QAM constellations at 3 GHz were conducted using a Vector Network Analyzer (VNA). A credible agreement between simulation and measurement was obtained after considering some correction methods, as illustrated in Fig. 3.19.

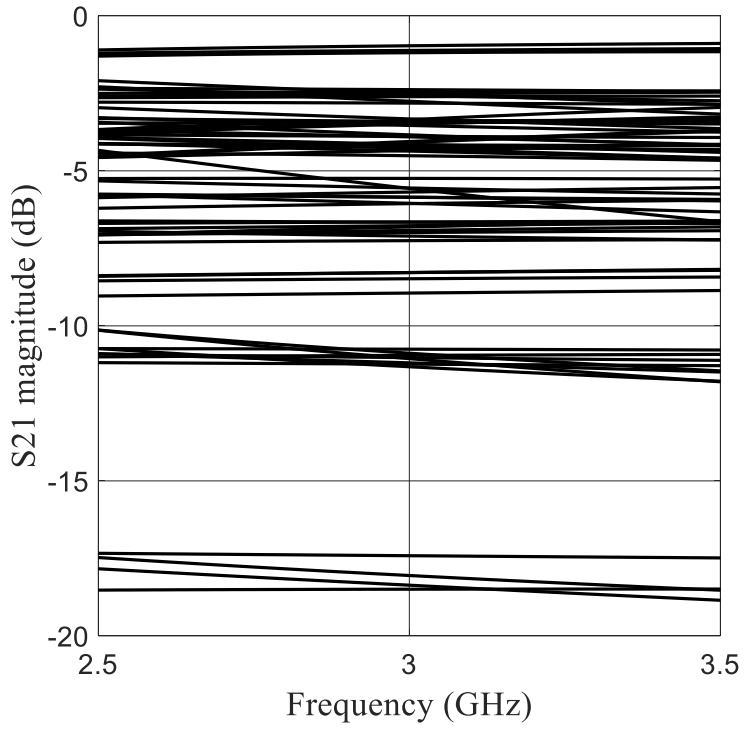

(a)

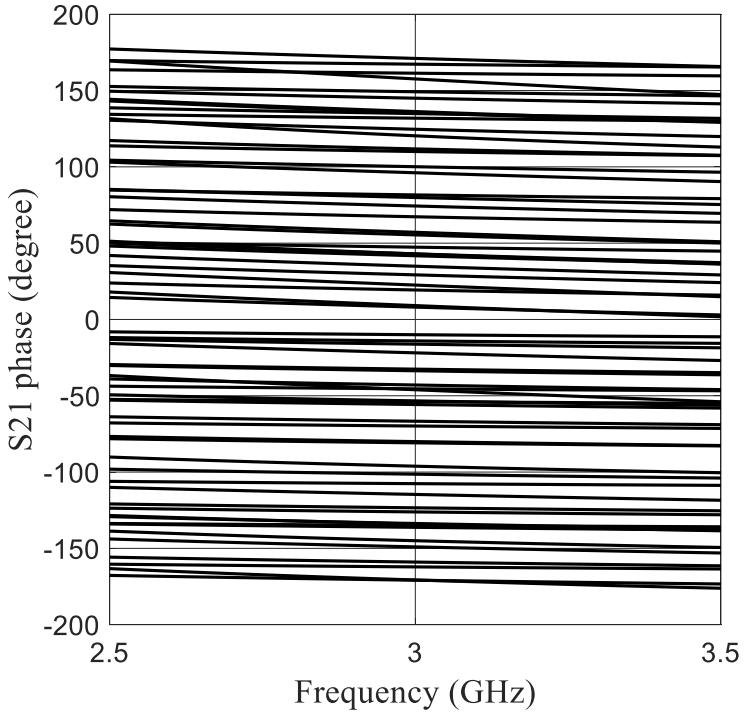

(b)

Figure 3.16: Simulated 64-QAM constellations generated by the load modulator over a 1 GHz bandwidth centered around 3 GHz. a) S_{21} magnitude. b) S_{21} phase.

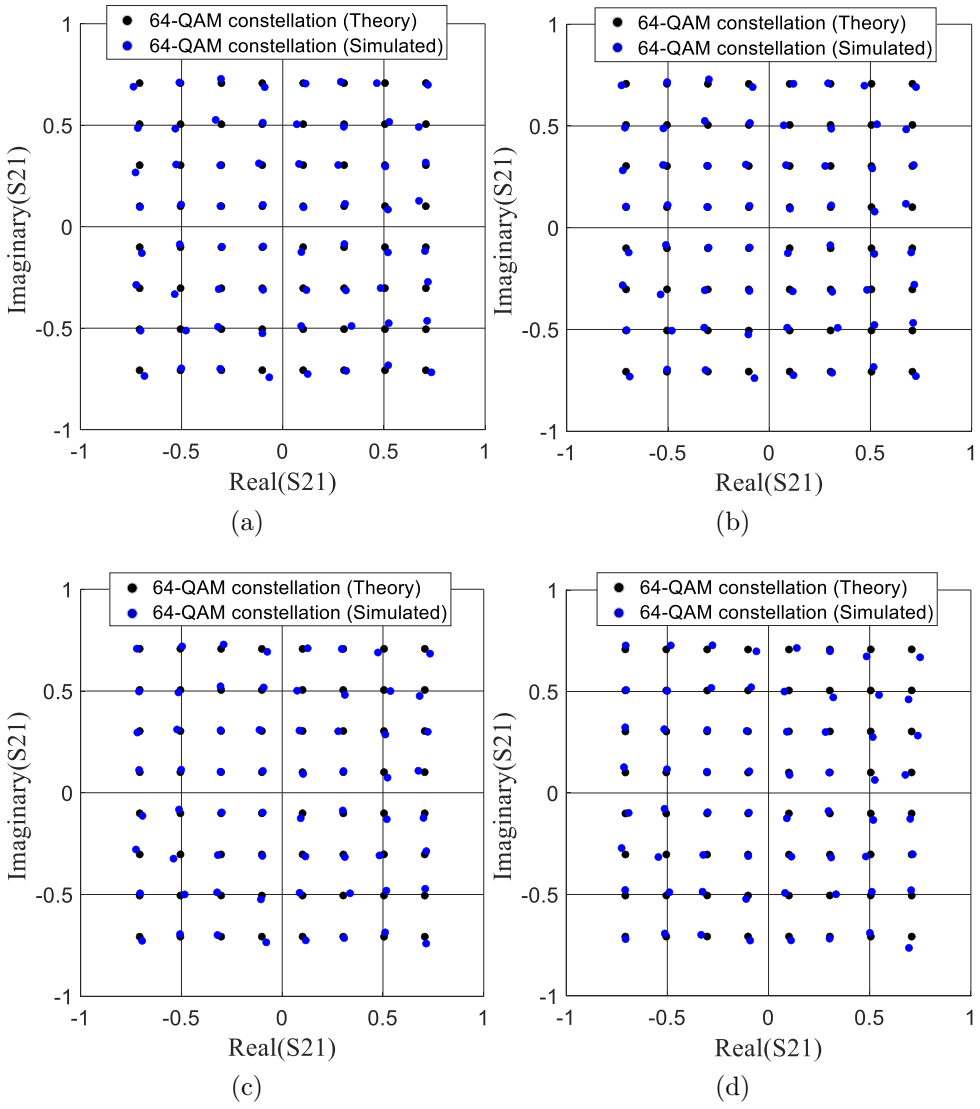

Figure 3.17: Comparison between the ideal 64-QAM constellations (black dots) and the simulated constellations generated by the load modulator circuit (blue dots) at four different frequencies. (a) 2.9 GHz. (b) 2.95 GHz. (c) 3.0 GHz. (d) 3.1 GHz.

Table 3.3
Summary of related work and efficiency comparison

Ref.	**Proposed System**	**Constellation Size**	**Fig. of Merit**	**No. Switches**	**Efficiency**
[54]	Switched parasitic array	2	BER vs. SNR	2	95%
[55]	Single RF MIMO	2	capacity vs. SNR	2	N/A
[59]	Serial & Parallel six-port modulator	4	EVM (4% parallel, 13% series)	4	100% serial, 50% parallel
[62]	M-QAM six-port modulator	64	EVM (8%)	12	75%
[63]	Tunable matching network	N/A	60% Smith chart coverage	7	40% back-off, 70% peak
[67]	Single RF MIMO transmitter	N/A	N/A	N/A	60% - 70%
[68]	QPSK/16-QAM load modulator	4 & 16	17.8 dB signal-to-distortion ratio	8	N/A
[This Paper]	64-QAM load modulator	64	EVM (3.6% simulated, 15.5% measured)	11	70% - 77%

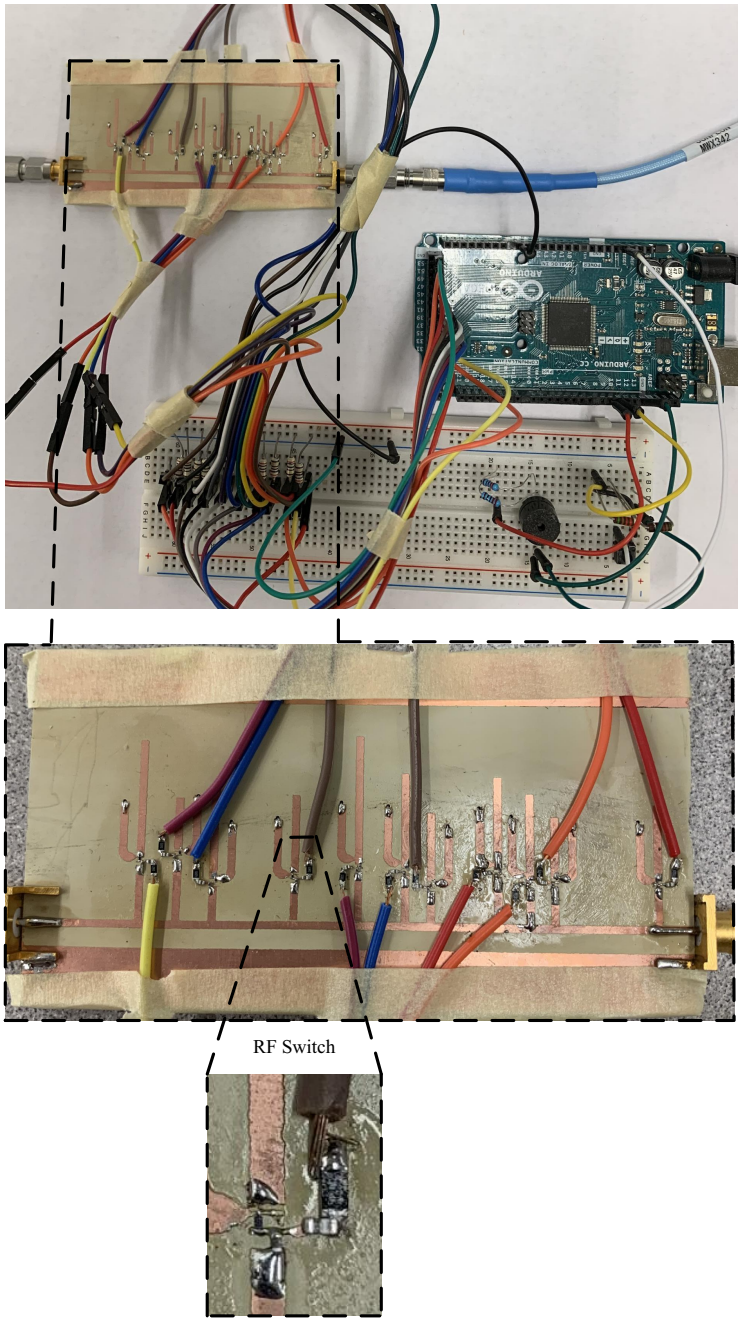

Figure 3.18: Fabricated prototype of an eleven-stage load modulator circuit including eleven switches and the measurement setup.

It has been observed through measurements that the amplitudes of the output signals of the load modulator at 3 GHz incurred a loss ranging between 0.5 and 1 dB, as shown in Fig. 3.19(a). This loss can be attributed to several factors. For example, the substrate used in the load modulator circuit design may possess a dielectric constant slightly different from what is reported in its datasheet. Moreover, the fabricated switch introduced a slightly higher

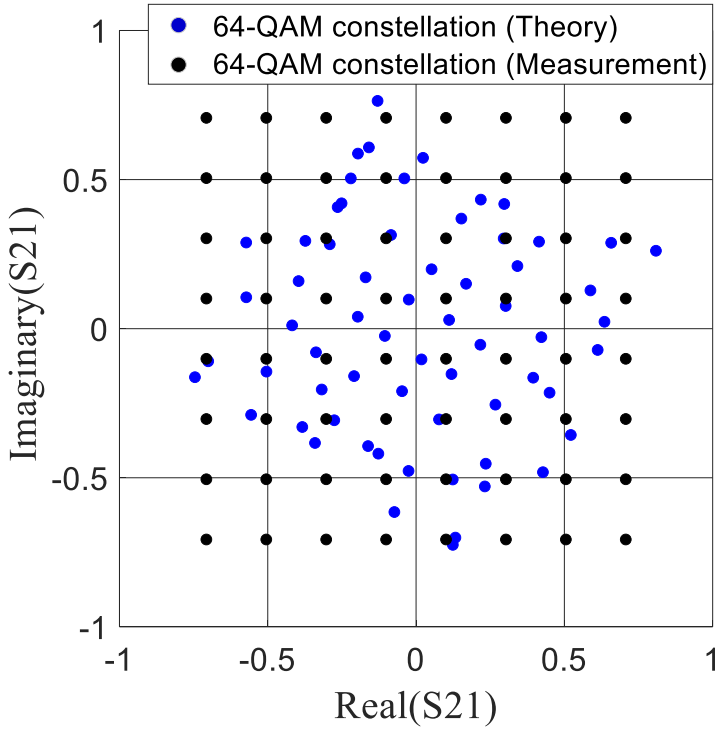

(a)

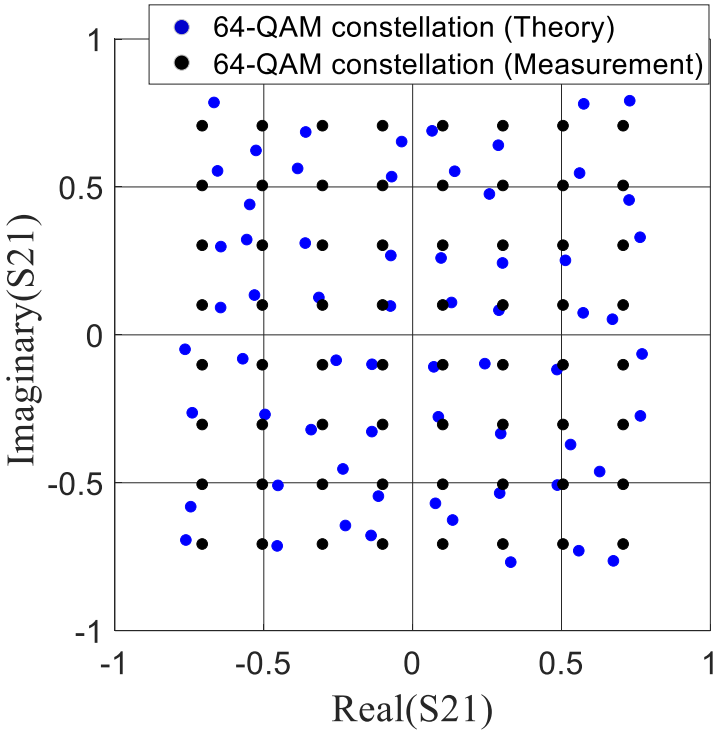

(b)

Figure 3.19: Measured 64-QAM constellations at 3 GHz. a) Before applying correction steps. b) After applying correction steps.

insertion loss than what was achieved in simulations, as shown earlier in Fig. 3.7 and Fig. 3.8.

Additionally, the SMA connectors installed at the input and the output of the two-port load modulator network introduce losses. An increase of about 20%, on average, of the amplitude of the signal generator can compensate for the loss sources. Another observation from the measurement was that the phases of the output signals were shifted by 25° to 30°. This phase shift is owed to the additional length of the final circuit product incurred by adding the SMA connectors at the input and output ports and incorporating the RF switches. To account for this phase shift, the length of the final line segment in the load modulator structure (line l_{tune}) can be changed and used as a phase tuner. The line l_{tune} slightly impacts the amplitude of the generated constellations but controls their phases. After averaging the shift in the phases of all 64-QAM constellations, a retroactive fine-tuning stage is performed to determine the length l_{tune} that will restore the phases of the outputs generated from the original design process. The line l_{tune} can be changed to correct the phase error resulting from fabrication. The measured 64-QAM constellations at 3 GHz after applying the correction steps are shown in Fig. 3.19(b). After applying the correction steps, the measured EVM of the fabricated eleven-stage load modulator circuit is as follows. The RMS EVM is 11.58%, the maximum EVM is 27.55%, the 90th percentile EVM is 15.51%, and the RMS EVM in dB is -18.73 dB.

To assess the linearity of the load modulator, two unique constellation points generated by the load modulator were considered in two different instances. For example, the switches of the load modulator were biased such that the load modulator generated the constellations shown in Fig. 3.20 (the constellation points in the red circle). After that, two spectrally pure tones were applied to the load modulator. The output signal power and the relative amplitude of the third-order product were plotted as a function of the input signal power, as illustrated in Fig. 3.20. It can be observed that the third-order intercept points (IP3) for these two specific constellations are 48.14 dBm and 47.57 dBm, respectively. Moreover, the 1-dB compression points of the load modulator when generating the constellation points shown in Fig. 3.21 are 22.7 dBm and 22.37 dBm, respectively.

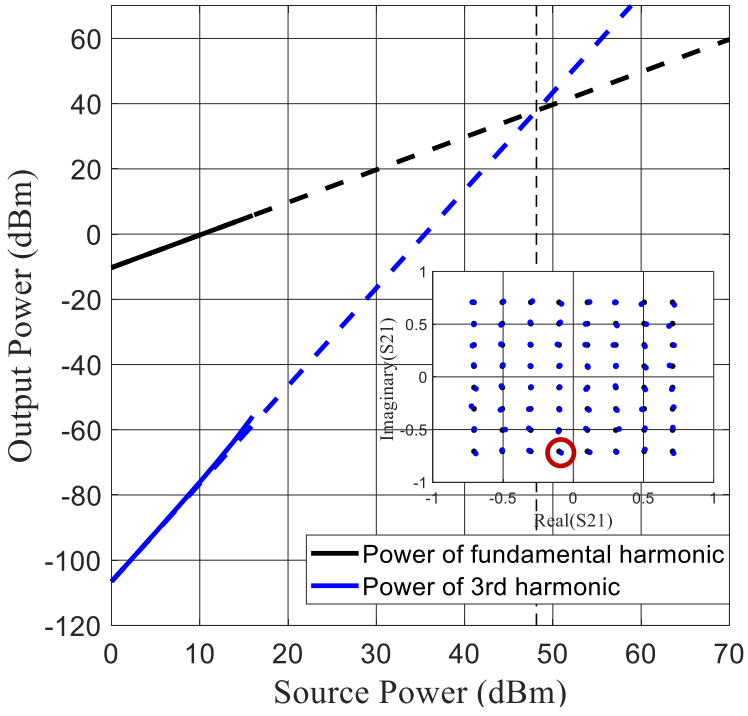

(a)

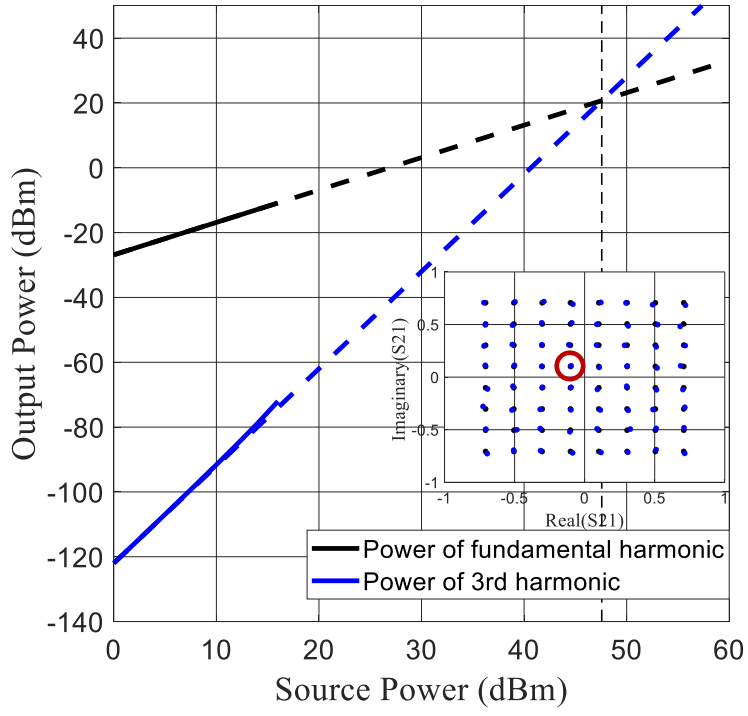

(b)

Figure 3.20: IP3 point of the load modulator. a) When the load modulator generates the constellation in the red circle. b) When the load modulator generates the constellation in the red circle.

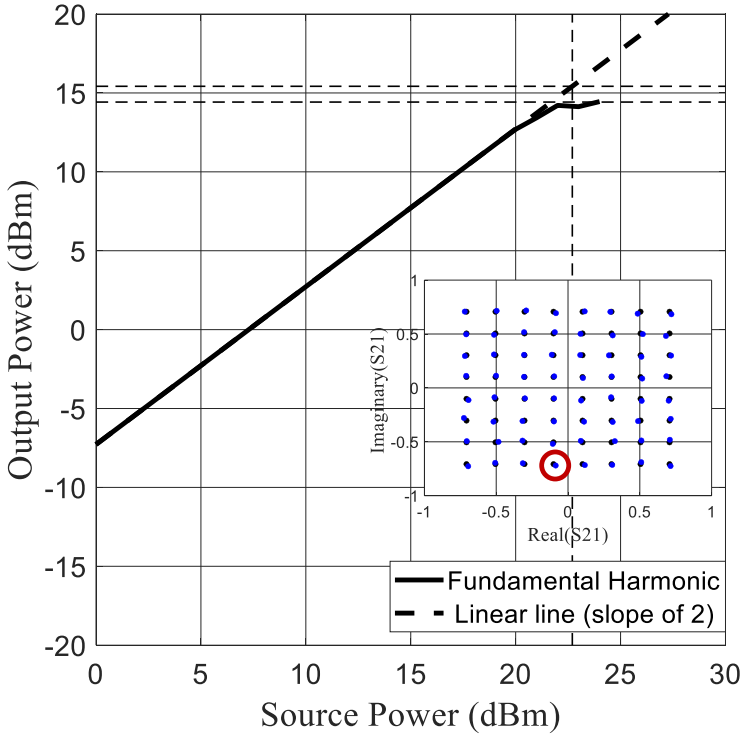

(a)

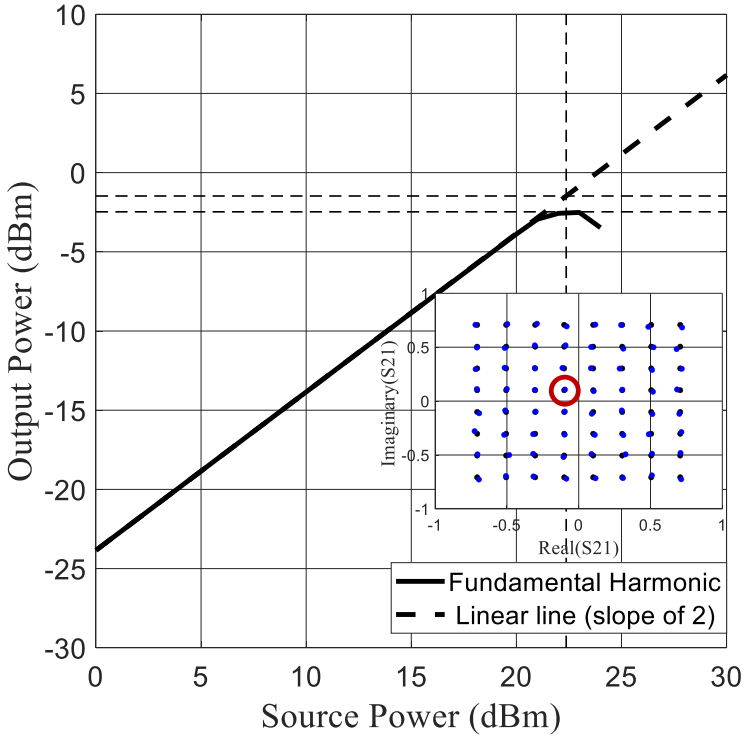

(b)

Figure 3.21: 1-dB compression point of the load modulator. a) When the load modulator generates the constellation in the red circle. b) When the load modulator generates the constellation in the red circle.

3.5 Conclusion

The design of a 64-QAM load modulator has been presented. The modulator is designed to operate at 3 GHz. A two-port network called the load modulator is connected to the antenna. The load modulator generates outputs by changing its internal parameters. The load modulator is implemented using microstrip transmission lines and PIN diodes. The load modulator circuit uses the serial concatenation of several L-section microstrip lines. The PIN diodes are used to make the passive microstrip-based structure of the load modulator circuit into a configurable one. Hence, the same structure will generate different outputs by only changing the state of the PIN diodes. An optimization algorithm has been used to find the design parameters of the load modulator circuit. The results show that the load modulator generates outputs that match the constellation of the 64-QAM. A microcontroller system provides bias voltages to the PIN diodes in the load modulator representing the baseband data. The proposed architecture does not require a digital-to-analog converter (DAC) for modulation, and the signal generator remains fixed all the time. Measurements of the fabricated prototype have shown a close agreement with the simulation after applying a few correction steps.

Chapter 4

Design of a Four-Branch Load-Modulated MIMO Transmitter

This chapter presents the design of a four-branch reduced-complexity MIMO transmitter based on load modulation. The transmitter can independently generate 64-QAM constellations at the input of the radiating elements. The waveforms of the 64-QAM constellations are generated by changing the impedance parameters of the load modulator circuits connected to antennas. At the same time, the output oscillator is kept constant. Thus, a single RF chain can drive the entire transmitter where the power amplifier amplifies a constant signal all the time and does not need to operate in the back-off region. A four-way Wilkinson power divider is used to split the power to the four branches of the transmitter. Microstrip patch antennas have been connected to the load modulators to transmit the desired outputs. RF isolators are connected to the input of load modulators to absorb reflections from each branch, allowing branches to generate desired outputs independently and maintaining the system matched at the input all the time. The proposed transmitter does not require mixers and digital-to-analog converters (DACs). The transmitter has been fabricated, and the over-the-air transmission of 64-QAM signals has been tested. The architecture can be scaled to larger array sizes, making it suitable for adoption in 5G massive MIMO systems. High cost, energy, and RF complexity savings can be achieved if the transmitter is scaled to a greater number of branches.

4.1 Block Diagram of the Reduced-Complexity Load-Modulated MIMO Transmitter

The block diagram of the four-branch load-modulated MIMO transmitter is shown in Fig. 4.1.

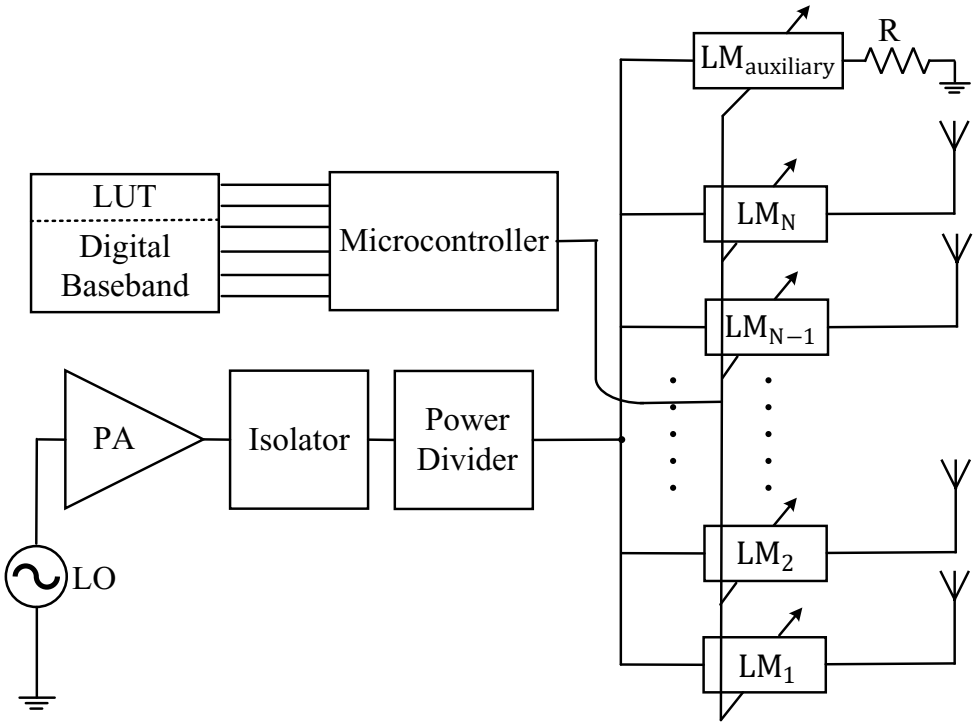

Figure 4.1: Block diagram of the load-modulated MIMO transmitter.

The RF circuitry of the reduced-complexity load-modulated MIMO transmitter consists of an LO generating a sinusoidal wave with a constant amplitude. The LO is followed by a Class-F PA that amplifies a constant envelope. An isolator is connected to the output port of the PA to protect it from any power reflections in the system. The antennas are connected to the single RF chain through load modulator (LM) circuits. The LM is a two-port network generating desired QAM constellations on the antennas. A power divider is used to split the transmit power to the N branches. An auxiliary LM branch is connected to a resistor R to absorb reflections from all other branches, allowing the branches to generate the desired outputs independently and to maintain matching conditions at the input of the power divider. The transmitter works as follows. The modulated signals on the antennas (e.g., the I and Q components of the 64-QAM constellations) are generated by varying the impedance of the load modulator (e.g., changing the state of the RF switches embedded in the load modulator). A programmable microcontroller generates the required bias voltages for the RF switches in the load modulator based on a look-up table (LUT) that contains mapping data. The LUT stores the switch states that generate the 64-QAM constellations at the output of the load modulator. This transmitter does not require a mixer, ADC, nor a DAC. Hence, it is simpler, less complicated, cheaper, and more efficient than conventional MIMO transmitters and can achieve substantial cost, complexity, and energy savings

if utilized in massive MIMO systems.

4.1.1 Load Modulation

The purpose of the RF chain in a communication transmitter is to generate a current on the antenna proportional to the desired transmit signal. The impedance of the RF circuitry is kept constant while the voltage is changed proportionally to the baseband signal. This mechanism is referred to in standard RF transmitters as voltage modulation. The advantage of voltage modulation is the near-perfect matching of the RF-chain circuitry to the antenna. However, the disadvantage is the large back-off needed to drive the PA. In load modulation, the RF-chain circuitry generates the complex baseband representation of the transmit signal on the antenna. At the same time, the voltage source at the PA is a fixed sinusoidal carrier signal. Thus, the PA does not require linearity with a large back-off but can be a simple, highly efficient nonlinear PA that amplifies a constant envelope. However, the disadvantage of load modulation is the severe mismatch between the load modulator and the rest of the RF chain. The input impedance seen by the analog source voltage varies in every update of the load modulator in each symbol time as a function of the desired current on the antennas in consecutive signaling periods. Hence, novel, albeit complicated, tunable impedance matching techniques are required to reduce the power loss due to the reflections generated by the load modulators at every symbol time.

Another solution has been adopted in this work to solve the matching problem. The mismatch problem can be solved simply by connecting an RF isolator at the input of each load modulator circuit. The commercial UIYSI20A surface-mount-type RF isolators were utilized in the design of the transmitter. These isolators have an insertion loss of 0.2 dB, isolation of 25 dB, VSWR of 1.10, forward power of 60 W, and reverse power of 10 W. The reflections generated by the load modulator will be absorbed by the isolator allowing the branches to operate independently. The block diagram presented in Fig. 4.1 has been modified to reflect the circuitry change needed to solve the mismatch problem of load-modulated MIMO transmitters, as shown in Fig. 4.2. As can be noticed, the auxiliary impedance matching branch is no longer needed. Additionally, the isolator connected to the PA is no longer needed as the isolators absorb reflections generated by load modulators in each branch.

4.1.2 Power Divider

Power dividers are passive microwave components used for power division. The Wilkinson power divider (WPD) is a common microstrip-based microwave power splitter. The WPD is a specific class of power divider circuits that can achieve isolation between the output ports while maintaining a matched con-

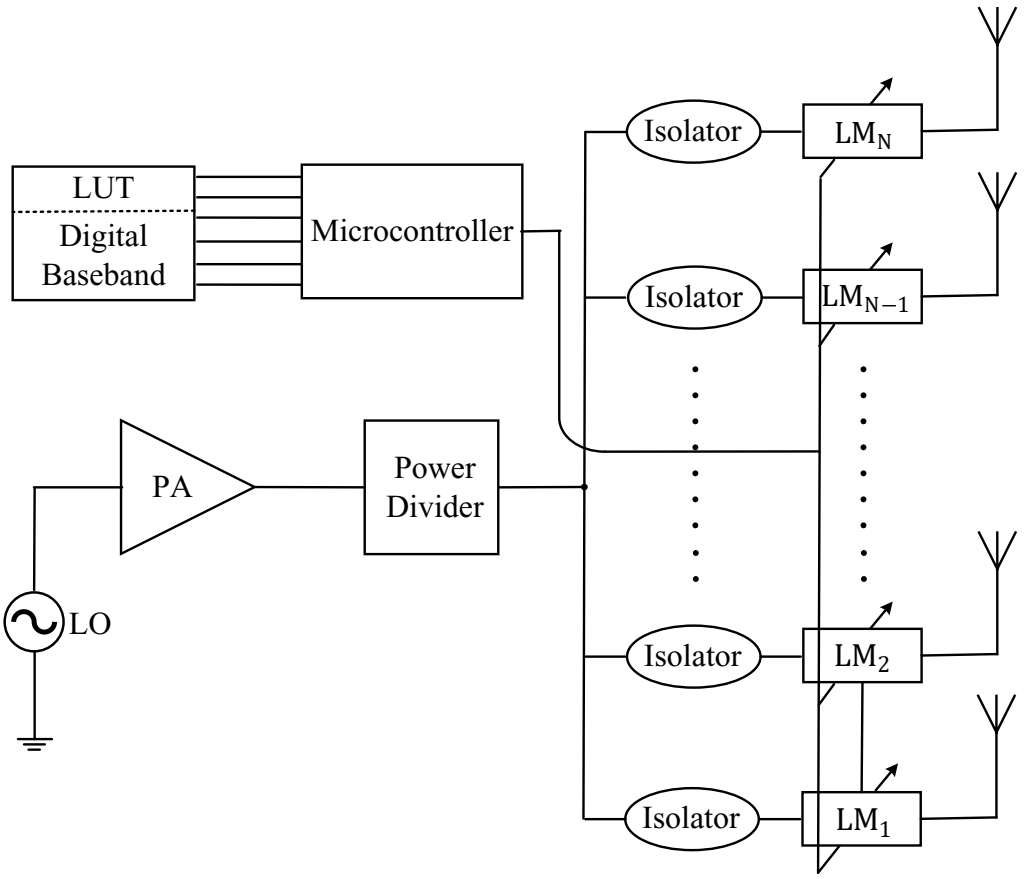

Figure 4.2: Block diagram of a strongly-matched N-branch reduced-complexity load-modulated MIMO transmitter.

dition on all ports [87], [88]. An example of a two-way WPD is illustrated in Fig. 4.3.

Since the 64-QAM load modulator circuit presented in the previous chapter is also a microstrip-based microwave circuit, it is suitable to be connected to WPD. However, there is a problem that the input impedance of the 64-QAM load modulator changes for every constellation point generated at its output. Since the output ports of the WPD are connected to the input ports of the load modulator, the matching at the output ports of the WPD will be impacted, compromising the matching condition at the input port of the WPD. Therefore, it is essential to use an isolator before the input port of the WPD to protect the PA from the reflections coming from the input port of the WPD.

A four-way WPD has been designed to feed the four load modulators of Fig. 4.1. The layout of this four-way WPD is depicted in Fig. 4.4. The four-way power splitter was designed using the ADS software. The WPD resides on a substrate identical to the one used for the design of the 64-QAM load modu-

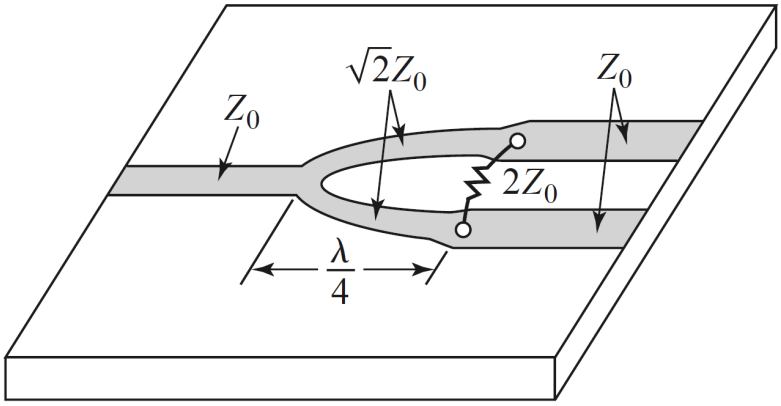

Figure 4.3: Equal-split two-way Wilkinson power divider (WPD). Adapted from [87].

lator. The performance of the designed four-way WPD is shown in Figs. 4.5, 4.6, and 4.7.

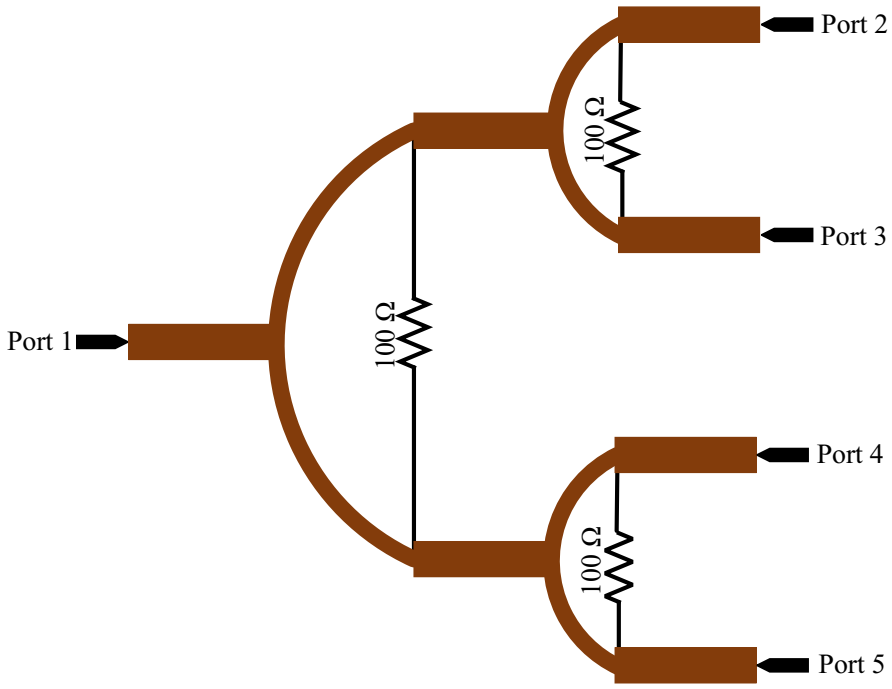

Figure 4.4: Layout of the four-way WPD.

Fig 4.5 shows the reflection coefficient at the input port S_{11} and the output ports S_{22}, S_{33}, S_{44}, and S_{55}. It shows that all ports (input and output) are matched at the frequency of interest, 3 GHz. Fig 4.6 shows the transmission coefficients S_{21} and the output ports S_{31}, S_{41}, and S_{51}. It can be shown that the power is equally split among the output ports. The isolation between output ports is shown in Fig. 4.7. It can be observed that all output ports are isolated from each other.

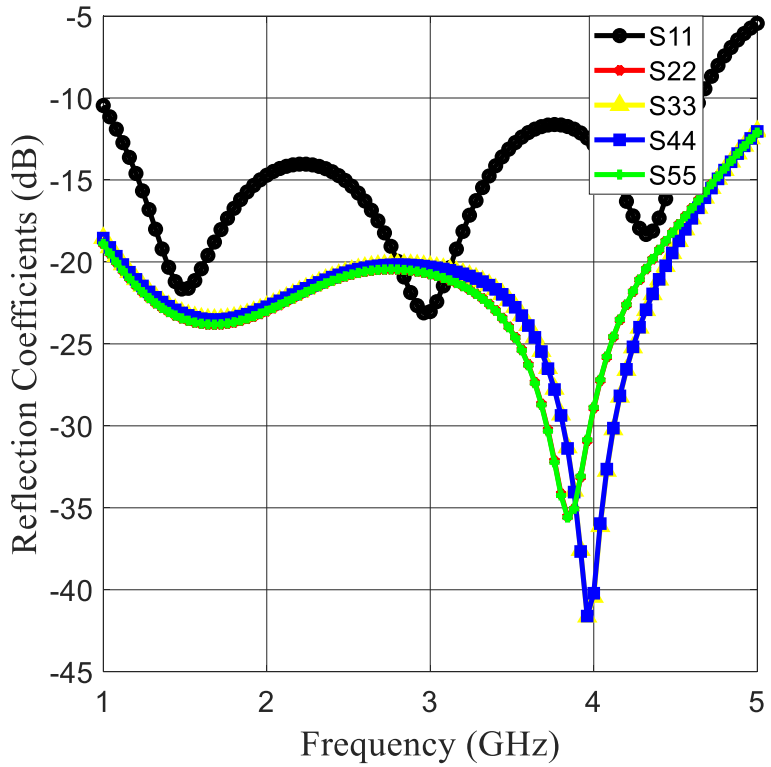

Figure 4.5: S_{ii} at the input and output ports of the proposed WPD.

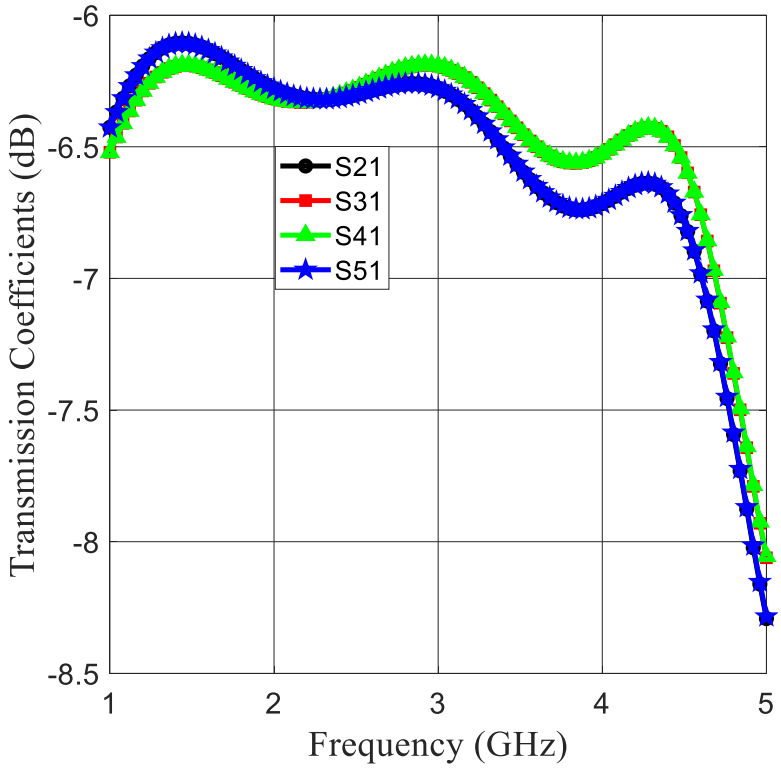

Figure 4.6: S_{ij} of the proposed WPD.

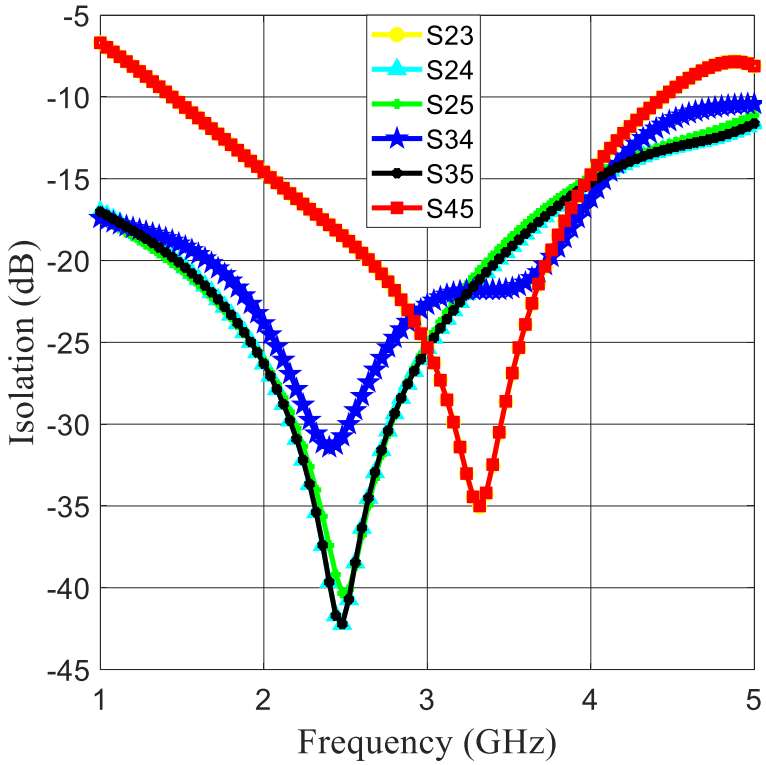

Figure 4.7: Isolation between the output ports of the proposed WPD.

4.2 A Four-Branch Reduced-Complexity Load-Modulated MIMO Transmitter

This section presents the design of four branches of the proposed reduced-complexity load-modulated MIMO transmitter. A four-way WPD is connected to the input ports of four isolators. The outputs of these isolators are connected to four load modulator circuits, the ones presented in [54]. The proposed load-modulated MIMO transmitter generates 64-QAM constellations at the output of the load modulators. Each branch can generate 64-QAM constellations independently from the other branches, while the input port of the transmitter is strongly matched for all 64-QAM outputs. The layout of the proposed load-modulated MIMO transmitter is illustrated in Fig. 4.8. The structure has been simulated using Advanced Design System (ADS). The transmitter has been designed on Rogers TMM 10i laminate with the following properties.

- Substrate Height $H = 1.27mm$
- Dielectric Constant $\epsilon_r = 9.9$
- Conductor Cladding $T = 35\mu m$
- Dielectric Loss $\delta_d = 0.002$

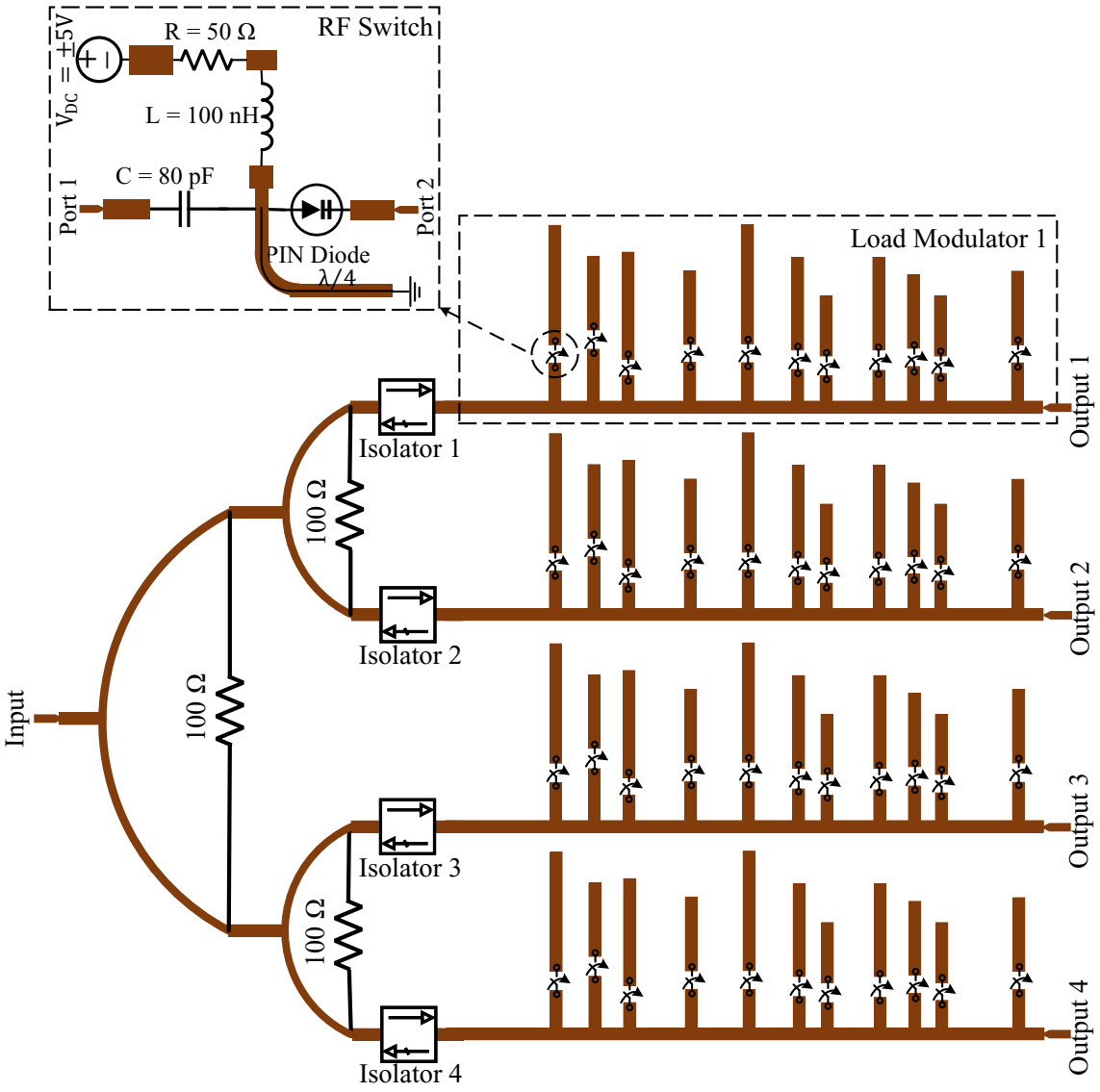

Figure 4.8: Layout of a four-branch load-modulated MIMO transmitter.

The transmission parameters, S_{21}, at the output port of the first branch are depicted in Fig. 4.9. It can be observed that the load modulator circuit of the first branch generates 64-QAM constellations at 3 GHz at its output port. The transmission parameters of the second, third, and fourth branches are identical to the transmission parameters of the first branch.

Fig. 4.10 shows the reflection coefficient S_{11} at the input port of the transmitters at 3GHz. It can be observed that the transmitter is well matched for all 64-QAM possible outputs.

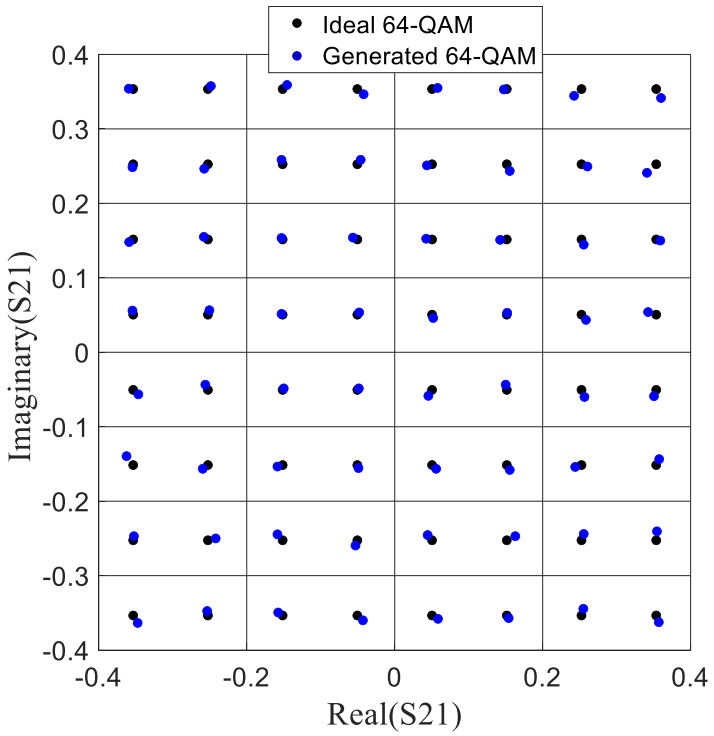

Figure 4.9: Comparison between the reference 64-QAM constellations (black dots) and the simulated constellations generated at the output of each load modulator branch (blue dots).

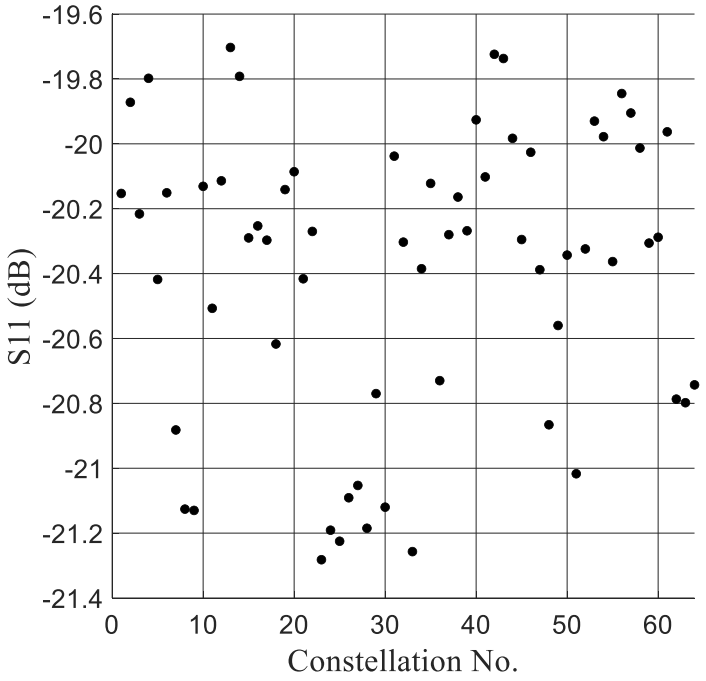

Figure 4.10: S_{11} at the input port of the load-modulated MIMO transmitter with four isolators connected to the outputs of WPD.

4.2.1 Antenna Design

An inset-fed microstrip patch antenna operating at 3 GHz has been designed. This antenna will be connected to the output port of load modulators to transmit the desired 64-QAM constellations. Microstrip patch antennas are low profile, mechanically robust, and cheap to manufacture using Printed-Circuit Board (PCB) technology. Microstrip antennas consist of a very thin metallic trace (patch) residing on a substrate of thickness much less than the free-space wavelength above a ground plane. The proposed single-element rectangular microstrip patch antenna fed by a microstrip line is shown in Fig. 4.11.

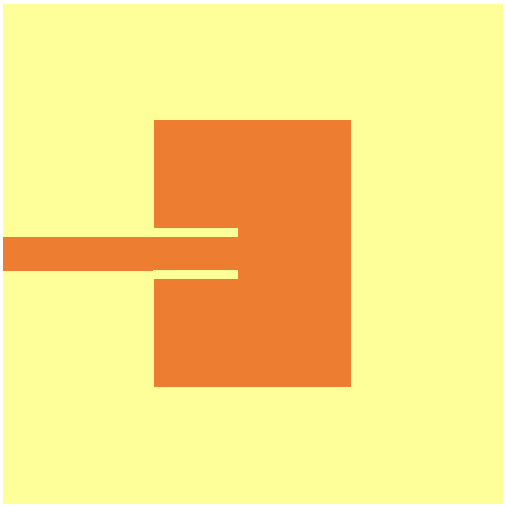

Figure 4.11: Layout design of the proposed microstrip patch antenna.

The same Rogers TMM 10i laminate has been used in the design of the proposed antenna element. The geometric parameters of the antenna in Fig. 4.11 are given as the following:

- **Substrate thickness:** 1.27 mm.
- **Substrate size:** 40 mm $\times$ 40 mm.
- **Dielectric constant (ϵ_r):** 9.9.
- **Patch size:** 21.42 mm (width) $\times$ 15.53 mm (length).
- **Slit size:** 6.4 mm (width) $\times$ 1 mm (length).
- **Feed line size:** 1.19 mm (width) $\times$ 16 mm (length).

ANSYS HFSS, a 3D electromagnetic (EM) simulation software for designing and simulating high-frequency electronic products, was used to design and simulate the proposed antenna. Fig. 4.12 shows that this antenna element is well matched at 3 GHz; however, the bandwidth is very narrow (30 MHz).

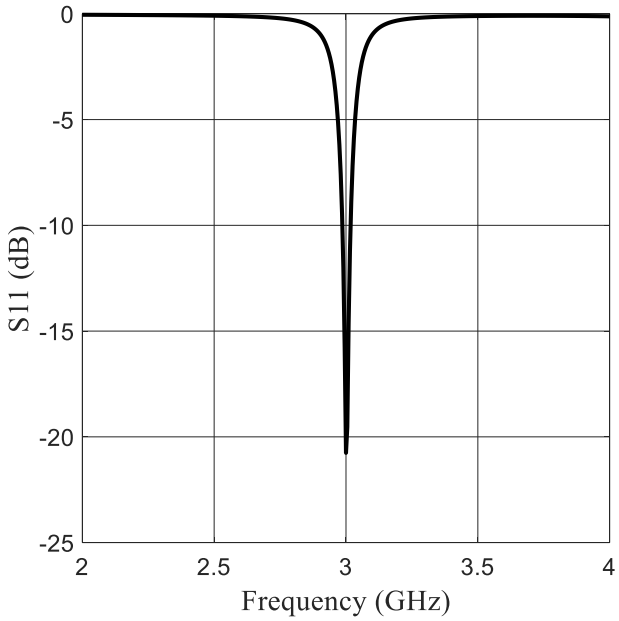

Figure 4.12: Simulated S_{11} of the proposed single microstrip patch antenna.

Many techniques are proposed in the literature for bandwidth enhancement, which will be a future step in further improving the performance of the proposed antenna. The 3D gain pattern of the proposed antenna element is depicted in Fig. 4.13. It shows a 5.5 dBi gain.

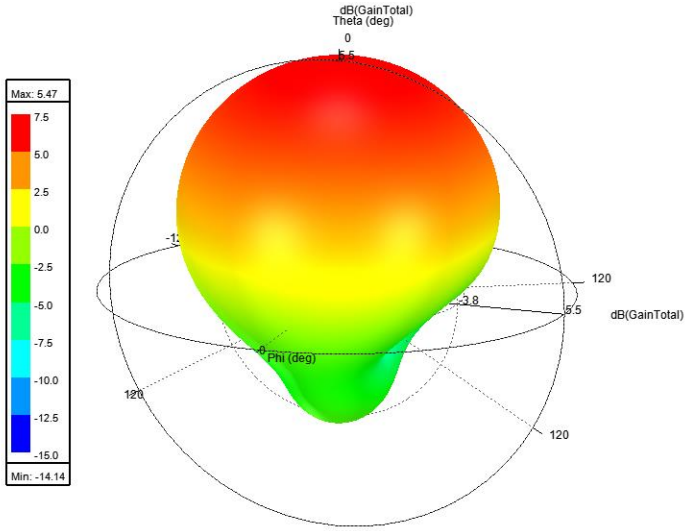

Figure 4.13: 3D gain pattern of the proposed microstrip patch antenna.

There are many techniques to increase the bandwidth of microstrip patch antennas (e.g., aperture coupling, multi-layer substrates, substrate thickness). However, most of these techniques cannot be integrated into the proposed MIMO transmitter since we are limited to having a single-layer laminate and

microstrip feed line. To increase the bandwidth of the proposed patch antenna, a coupling slot has been etched on the radiating patch, as shown in Fig. 4.14.

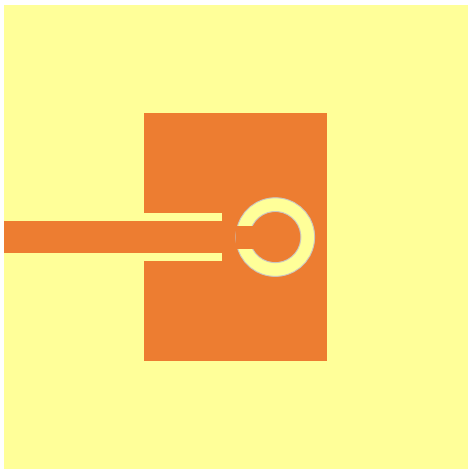

Figure 4.14: Proposed microstrip patch antenna with a coupling slot etched on the radiating patch.

The coupling slot can be optimized to generate a resonance close to the resonance generated by the original patch antenna. Thus, increasing the bandwidth. Fig. 4.15 shows S_{11} at the input of the upgraded microstrip patch at 3 GHz. It can be observed the bandwidth has increased to 115 MHz.

The 3D gain pattern of the bandwidth-enhanced microstrip patch antenna is

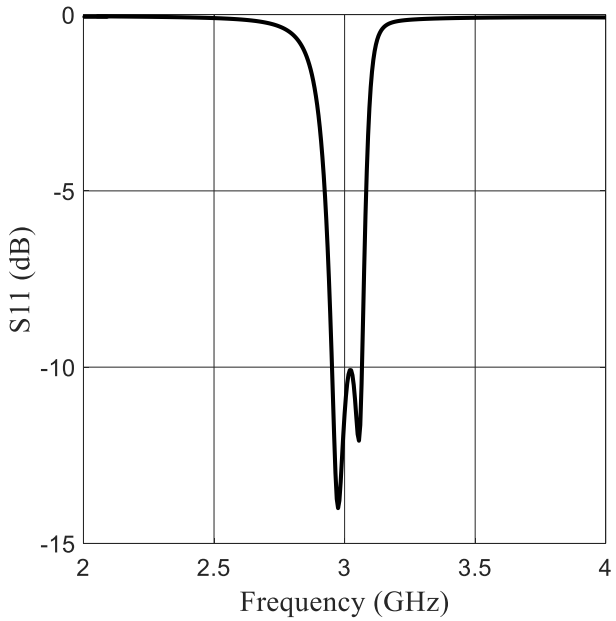

Figure 4.15: Simulated S_{11} of the bandwidth-enhanced patch antenna.

depicted in Fig. 4.16. It shows a 4.93 dBi gain.

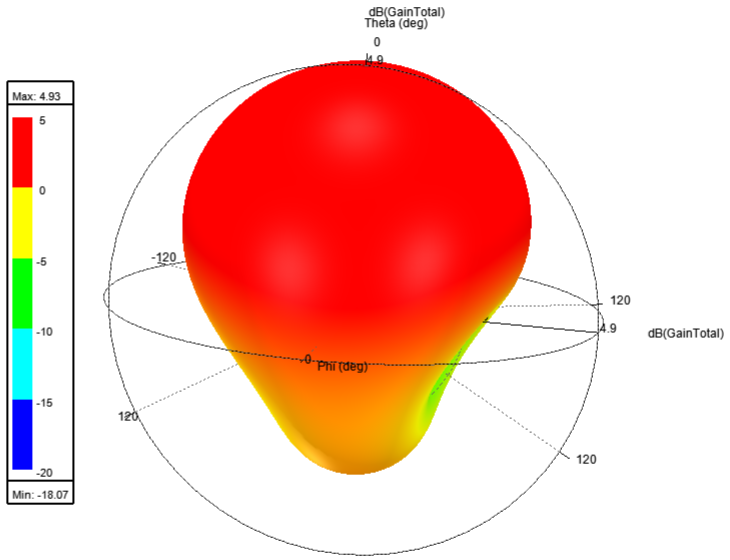

Figure 4.16: 3D gain pattern of the bandwidth-enhanced patch antenna.

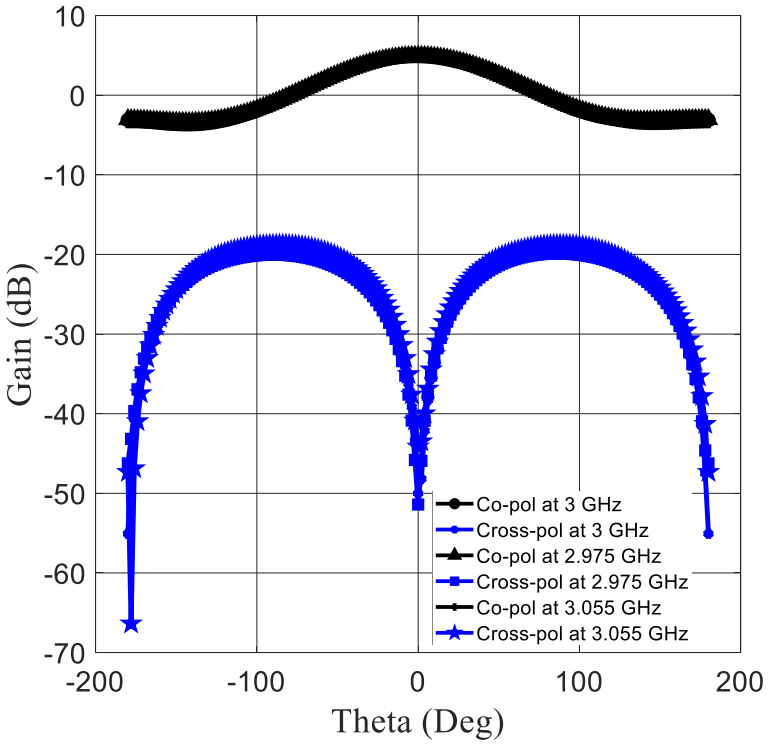

Figure 4.17: Co- and cross-polarization gain patterns.

The co- and cross-polarization gain patterns are shown in Fig. 4.17. It can be observed that there is a good separation (roughly 19 dB in the worst-case scenario) between the co- and the cross-polarization gains at 2.975 GHz, 3.0 GHz, and 3.055.

4.3 Prototype of Four-Branch Load-Modulated MIMO Transmitter

The proposed four-branch load-modulated MIMO transmitter has been fabricated. Four inset-fed microstrip patch antennas have been connected to four load modulators, operating at 3 GHz over nearly 115 MHz. The spacing between the four antenna elements is 0.6λ. A broadband Vivaldi antenna has been used as a receive antenna. The fabricated four-branch load-modulated MIMO transmitter is depicted in Fig. 4.18.

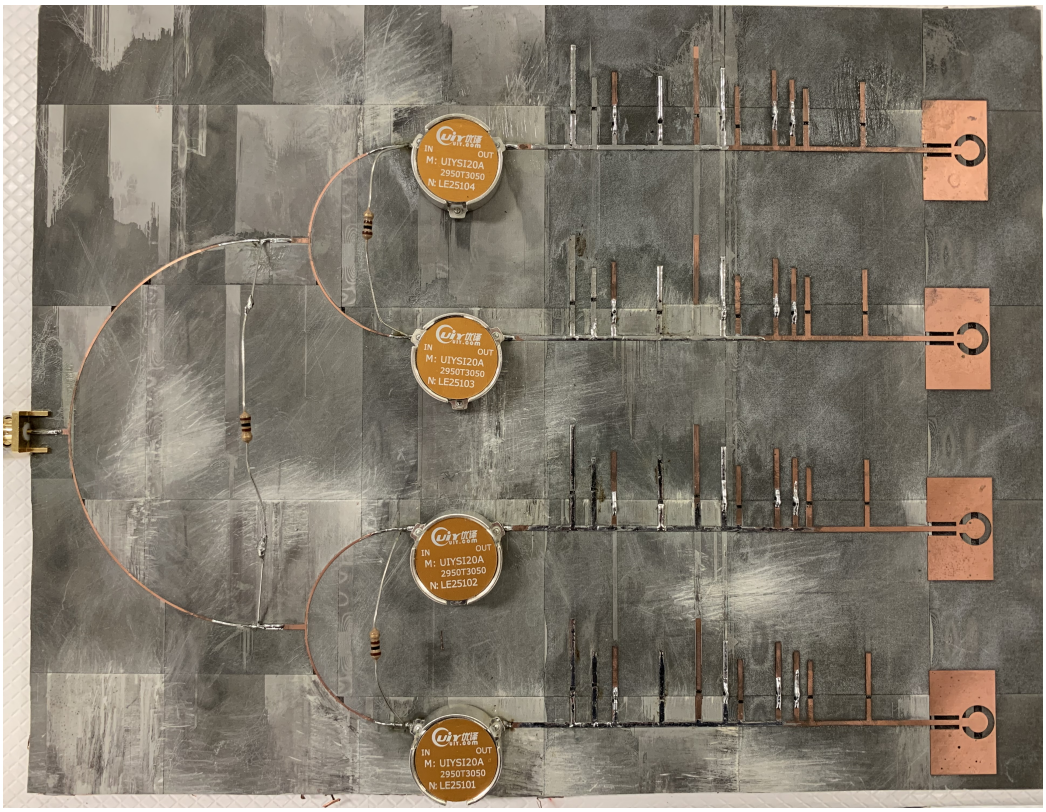

Figure 4.18: Fabricated prototype of the four-branch load-modulated MIMO transmitter.

The distance between the transmitter and the receiver is 50 cm. The desired 64-QAM outputs are generated by controlling the physical length of the stubs in the load modulator circuit. Copper tapes have been used to mimic the switches in their ON states. The transmitter has been adjusted to generate all 64-QAM constellations. In every instance, all four branches have been updated similarly to transmit the same 64-QAM symbol. The same test was carried on until all 64-QAM symbols were transmitted. The normalized received constellations after calibration are shown in Fig. 4.19.

The calibration is needed to compensate for the phase deviation and amplitude degradation that received constellations endured. The phase deviation

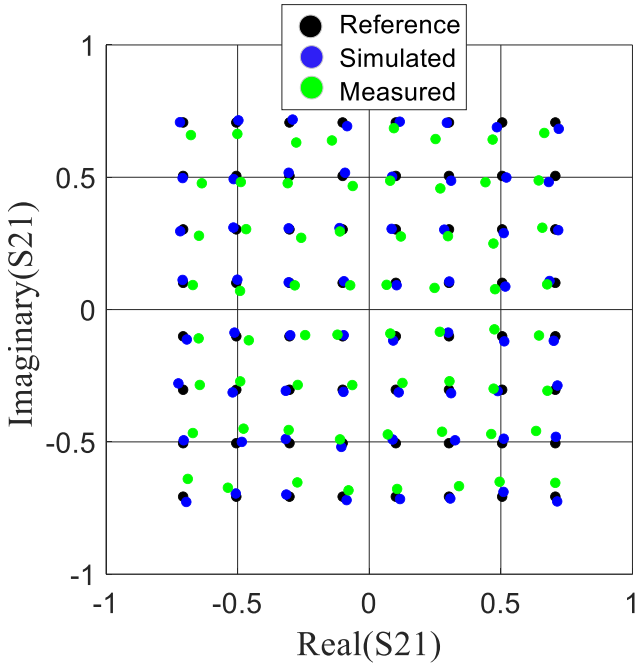

Figure 4.19: Normalized measured 64-QAM constellations (after calibration).

is caused by the additional cable length and distance between the transmitter and the receiver. The amplitude attenuation is due to the cables and path loss. The reference load modulator state is calibrated to eliminate the phase and amplitude errors, and the exact calibration is applied to the remaining 63 load modulator states at a given location. After calibration, the measured error vector magnitude (EVM) is given in Table 4.1.

Table 4.1
Simulated EVM of the 64-QAM constellations.

RMS EVM	7.67%
Maximum EVM	13.23%
90th percentile EVM	10.61%
RMS EVM [dB]	-22.3 dB

The divergence in the generated constellations can be reduced if the distance between the transmitter and receiver increases, where better far-field

conditions can be achieved. A credible agreement has been observed between the measured received constellations and the simulated ones.

4.4 Cost Reduction and Energy Saving

It has been demonstrated in the previous section that four branches of load modulators can be bundled utilizing a single RF chain. This grouping eliminates the need for a dedicated PA, mixer, and DAC in each branch, achieving considerable hardware savings. The load modulator generates the desired outputs by creating the proper reflections that lead to the generation of 64-QAM constellations (specific complex S_{21} values). The outputs with the highest S_{21} amplitudes are in red circles, as shown in Fig. 4.20.

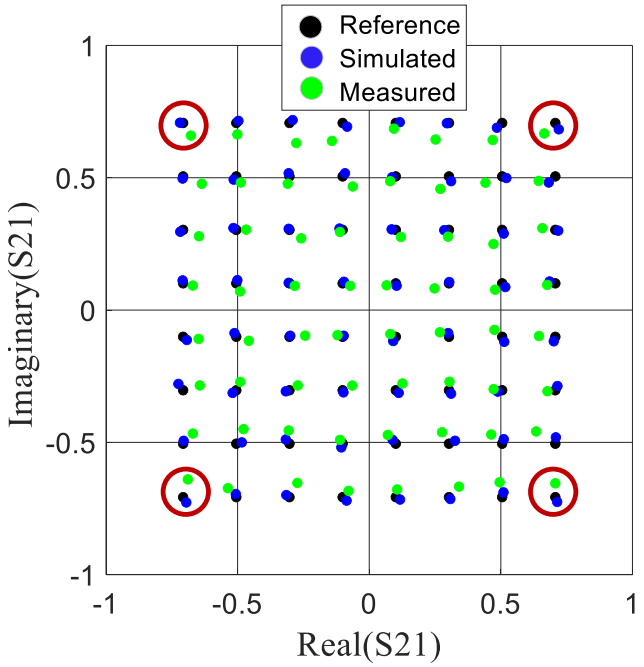

Figure 4.20: 64-QAM constellation points with emphasis on the constellations with the highest amplitudes (circled in red).

In other words, the load modulator is at its highest efficiency when generating the four symbol outputs in red circles. The remaining 60 constellation symbols have lesser amplitudes than the 4 constellations in red circles. Theoretically, the 64-QAM load modulator has an efficiency of 100% when generating the constellations in red circles. In contrast, the 64-QAM load modulator is at its lowest efficiency when generating the constellations in green circles, as shown in Fig. 4.21.

In these four cases, the power efficiency of the load modulator is 14.3%. On average, the power efficiency of the load modulator corresponding to the transmission of all 64-QAM constellation symbols is 61.48%. Hence, the re-

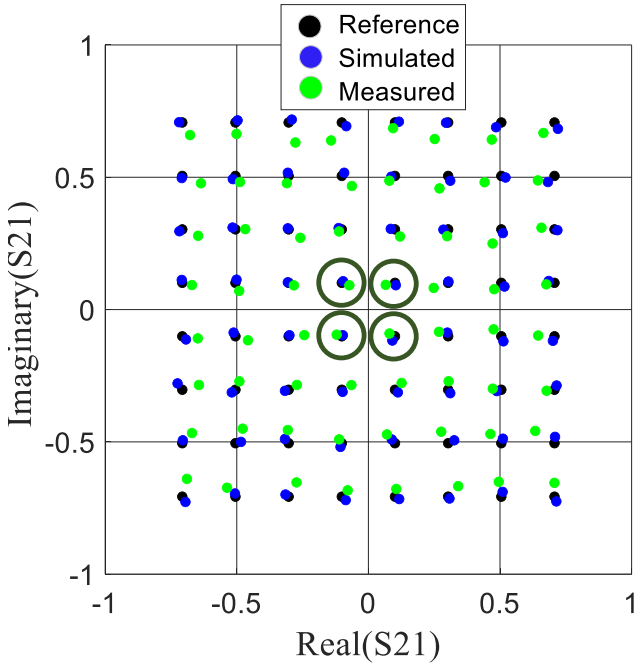

Figure 4.21: 64-QAM constellation points with emphasis on the constellations with the lowest amplitudes (circled in green).

flection at the input of the load modulator caused by the transmission of all 64-QAM constellation symbols is 38.52%.

The mean efficiency of Class-AB PAs used in conventional voltage-modulated MIMO transmitters is 20.7% when an OFDM signal with a PAPR of 10 dB is transmitted [43]. A regular Class-F PA has a peak efficiency of 80% [43]. Consider a MIMO system consisting of $N = 100$ antenna elements and assuming a total radiated power of 2.1 W. A conventional voltage-modulated MIMO transmitter uses a dedicated PA per antenna element. Hence, 100 PAs will be employed in the transmitter, each consumes 101.45 mW to radiate the required 21 mW for voltage modulation (21 mW is 20.7% of 101.45 mW). Alternatively, a single standard Class-F PA has a peak efficiency of 80%. All antenna elements in load modulated MIMO transmitters can be connected to a single Class-F PA that amplifies a source signal with constant amplitude. However, since the generation of the 64-QAM constellations causes on average reflections of 38.52% of power in the isolator, the efficiency of the Class-F PA drops from 80% to 49.18%. Hence, the Class-F PA consumes 4.27 W to radiate the required 2.1 W (2.1 W is 49.18% of 4.27 W). It can be concluded that the proposed load modulation approach consumes 58% less energy (4.27 W) than voltage modulation (101.45 mW*100 = 10.145 W). Additionally, to design a Class-AB PA for 10 dB PAPR, each yields a peak power of 202.9 mW, which is double the rms power of 101.45 mW. The common Class F amplifier operates at peak power and consumes 3.42 W. The peak power is the radiated power (2.1 W) plus the power reflected in the isolator, which is 1.316 W. The power

reflected in the isolator is basically the 38.52% drop from the 80% of the total consumed power by the Class-F PA 4.27 W (4.27*0.8*0.38 = 1.316 W). Even though the Class-F PA can replace $N = 100$ Class-AB PAs, its peak power is not 100 times higher but 16.86 times higher. From that, we can deduce that energy saving is not only achieved due to the selection of a cheaper class of amplifiers but also because of the 6 times lower aggregate peak power.

4.5 Conclusion

The design of a four-branch load-modulated MIMO transmitter is presented. Each branch can generate 64-QAM constellations at their outputs independently. The 64-QAM constellations are generated by changing the impedance parameters of the load modulator. A WPD is used to split the input power to the four branches. The transmitter showed great potential in being scaled up to use massive MIMO systems in terms of cost, complexity, and energy consumption.

Chapter 5

Conclusion

The goal of this dissertation has been the design of a single-RF chain load-modulated MIMO transmitter. Load modulation is an alternative for voltage modulation where RF signals are generated by changing the load impedance of the RF circuit, not by changing the input voltage. The load modulators are connected to a single PA that amplifies a constant-envelope input voltage. Each load modulator circuit controls one of the antennas. The modulated signals are generated on the antennas by changing the internal parameters of the load modulator, eliminating the need for a dedicated RF chain for each branch.

In this dissertation, a 64-QAM load modulator has been analyzed, designed, fabricated, and fully characterized. The same 64-QAM load modulator has been used in the design of a four-branch load-modulated MIMO transmitter. It has been shown that this MIMO transmitter can generate 64-QAM constellations independently while being connected to a single RF chain. The proposed load modulator can be scaled up and used with massive MIMO transmitters. A huge RF-circuitry cost and complexity reduction can be attained when the proposed load modulator is connected to antenna elements.

Many questions can pave the path for future work. The implementation of the branching can be complicated. In this dissertation, a four-branch MIMO transmitter was considered to prove the concept of load modulation in MIMO. Due to the limited number of branches, a WPD was sufficient to split the power to the branches. However, massive MIMO BSs are expected to be equipped with many more antennas; therefore, an efficient, non-lossy power delivery system should be designed. The possibility of bundling each subset of antennas (e.g., four or eight elements) and connecting the subset to a dedicated RF chain or using corporate-fed systems can be investigated in the future.

Moreover, other structures can be considered in the design of the load modulator circuit. In this dissertation, the load modulator has been realized by the serial concatenation of many L-section cells. The advantage of such a struc-

ture is the analysis through its ABCD matrices. However, eleven stages were needed to generate 64-QAM constellations. Other designs that could achieve a 64-QAM constellation with fewer stages are worth investigating. It would be interesting to compare the performance of many different load modulator circuits from the implementation standpoint.

On the other hand, there is also room for performance improvement of the reduced-complexity load-modulated single-RF MIMO transmitter by optimizing the design of the switch circuit. The better the insertion loss and the switching speed, the better the overall performance of the proposed load-modulated MIMO transmitter. In this report, PIN diode-based RF switches have been used in the design of the switching network. Utilizing shunt PIN diode RF switches in the load modulator block and comparing the system performance to the series ones is another interesting endeavor to pursue.

The last issue of the hardware design is considering the design of compact single-RF load-modulated MIMO transmitters (compact arrays with less than a half-wavelength spacing between elements) to reduce the physical size of the system. In this case, mutual coupling among elements arises, and the baseband block must process the effect of this mutual coupling. Therefore, the coupling effect must be accounted for in the impedance matrix model. This model must be designed, tested and verified.

References

[1] P. Cerwall, "Ericsson mobility report," *Ericsson, Sweden*, Jun. 2020.

[2] G. Stüber, *Principles of Mobile Communication*. Springer International Publishing, 2017.

[3] M. Agiwal, A. Roy, and N. Saxena, "Next generation 5G wireless networks: A comprehensive survey," *IEEE Communications Surveys Tutorials*, vol. 18, no. 3, pp. 1617–1655, 2016.

[4] X. Foukas, G. Patounas, A. Elmokashfi, and M. K. Marina, "Network slicing in 5G: Survey and challenges," *IEEE Communications Magazine*, vol. 55, no. 5, pp. 94–100, 2017.

[5] A. Zanella, N. Bui, A. Castellani, L. Vangelista, and M. Zorzi, "Internet of things for smart cities," *IEEE Internet of Things Journal*, vol. 1, no. 1, pp. 22–32, 2014.

[6] A. Ghosh, A. Maeder, M. Baker, and D. Chandramouli, "5G evolution: A view on 5G cellular technology beyond 3GPP release 15," *IEEE Access*, vol. 7, pp. 127 639–127 651, 2019.

[7] J. G. Andrews, S. Buzzi, W. Choi, *et al.*, "What will 5G be?" *IEEE Journal on Selected Areas in Communications*, vol. 32, no. 6, pp. 1065–1082, 2014.

[8] C. Freitag, M. Berners-Lee, K. Widdicks, B. Knowles, G. S. Blair, and A. Friday, "The real climate and transformative impact of ICT: A critique of estimates, trends, and regulations," *Patterns*, vol. 2, no. 9, p. 100 340, 2021.

[9] G. Foschini and M. Gans, "On limits of wireless communications in a fading environment when using multiple antennas," *Wireless Personal Communications*, vol. 6, no. 3, pp. 311–335, 1998.

[10] A. Goldsmith, *Wireless Communications*. Cambridge University Press, 2005.

[11] D. Gesbert, M. Kountouris, R. W. Heath, C.-b. Chae, and T. Salzer, "Shifting the MIMO paradigm," *IEEE Signal Processing Magazine*, vol. 24, no. 5, pp. 36–46, 2007.

[12] T. L. Marzetta, "Noncooperative cellular wireless with unlimited numbers of base station antennas," *IEEE Transactions on Wireless Communications*, vol. 9, no. 11, pp. 3590–3600, 2010.

[13] E. Björnson, E. G. Larsson, and T. L. Marzetta, "Massive MIMO: Ten myths and one critical question," *IEEE Communications Magazine*, vol. 54, no. 2, pp. 114–123, 2016.

[14] J. Lota, S. Sun, T. S. Rappaport, and A. Demosthenous, "5G uniform linear arrays with beamforming and spatial multiplexing at 28, 37, 64, and 71 GHz for outdoor urban communication: A two-level approach," *IEEE Transactions on Vehicular Technology*, vol. 66, no. 11, pp. 9972–9985, 2017.

[15] F. Boccardi, R. W. Heath, A. Lozano, T. L. Marzetta, and P. Popovski, "Five disruptive technology directions for 5G," *IEEE Communications Magazine*, vol. 52, no. 2, pp. 74–80, 2014.

[16] E. G. Larsson, O. Edfors, F. Tufvesson, and T. L. Marzetta, "Massive MIMO for next generation wireless systems," *IEEE Communications Magazine*, vol. 52, no. 2, pp. 186–195, 2014.

[17] S. Malkowsky, J. Vieira, L. Liu, *et al.*, "The world's first real-time testbed for massive MIMO: Design, implementation, and validation," *IEEE Access*, vol. 5, pp. 9073–9088, 2017.

[18] A. F. Molisch, *Wireless communications*. John Wiley & Sons, 2012.

[19] T. S. Rappaport, G. R. MacCartney, M. K. Samimi, and S. Sun, "Wideband millimeter-wave propagation measurements and channel models for future wireless communication system design," *IEEE Transactions on Communications*, vol. 63, no. 9, pp. 3029–3056, 2015.

[20] H. Friis, "A note on a simple transmission formula," *Proceedings of the IRE*, vol. 34, no. 5, pp. 254–256, 1946.

[21] I. A. Hemadeh, K. Satyanarayana, M. El-Hajjar, and L. Hanzo, "Millimeter-wave communications: Physical channel models, design considerations, antenna constructions, and link-budget," *IEEE Communications Surveys Tutorials*, vol. 20, no. 2, pp. 870–913, 2018.

[22] T. S. Rappaport, S. Sun, R. Mayzus, *et al.*, "Millimeter wave mobile communications for 5G cellular: It will work!" *IEEE Access*, vol. 1, pp. 335–349, 2013.

[23] Y. Azar, G. N. Wong, K. Wang, *et al.*, "28 GHz propagation measurements for outdoor cellular communications using steerable beam antennas in new york city," in *2013 IEEE International Conference on Communications (ICC)*, 2013, pp. 5143–5147.

[24] N. Bhushan, J. Li, D. Malladi, *et al.*, "Network densification: The dominant theme for wireless evolution into 5G," *IEEE Communications Magazine*, vol. 52, no. 2, pp. 82–89, 2014.

[25] J. G. Andrews, H. Claussen, M. Dohler, S. Rangan, and M. C. Reed, "Femtocells: Past, present, and future," *IEEE Journal on Selected Areas in Communications*, vol. 30, no. 3, pp. 497–508, 2012.

[26] P. K. Verma, V. Kishan, S. P. Singh, and M. Lakshmanan, "Capacity enhancement of femtocell," in *2019 4th International Conference on Information Systems and Computer Networks (ISCON)*, 2019, pp. 473–476.

[27] H. S. Dhillon, R. K. Ganti, and J. G. Andrews, "Load-aware modeling and analysis of heterogeneous cellular networks," *IEEE Transactions on Wireless Communications*, vol. 12, no. 4, pp. 1666–1677, 2013.

[28] L. M. Correia, D. Zeller, O. Blume, *et al.*, "Challenges and enabling technologies for energy aware mobile radio networks," *IEEE Communications Magazine*, vol. 48, no. 11, pp. 66–72, 2010.

[29] C. A. Balanis, *Antenna theory: analysis and design*. Wiley-Interscience, 2005.

[30] E. Telatar, "Capacity of multi-antenna Gaussian channels," *European Transactions on Telecommunications*, vol. 10, no. 6, pp. 585–595, 1999.

[31] T. L. Marzetta, "How much training is required for multiuser mimo?" In *2006 Fortieth Asilomar Conference on Signals, Systems and Computers*, 2006, pp. 359–363.

[32] L. Zheng and D. Tse, "Diversity and multiplexing: A fundamental tradeoff in multiple-antenna channels," *IEEE Transactions on Information Theory*, vol. 49, no. 5, pp. 1073–1096, 2003.

[33] K. V. Vardhan, S. K. Mohammed, A. Chockalingam, and B. S. Rajan, "A low-complexity detector for large MIMO systems and multicarrier CDMA systems," *IEEE Journal on Selected Areas in Communications*, vol. 26, no. 3, pp. 473–485, 2008.

[34] P. Švač, F. Meyer, E. Riegler, and F. Hlawatsch, "Soft-heuristic detectors for large MIMO systems," *IEEE Transactions on Signal Processing*, vol. 61, no. 18, pp. 4573–4586, 2013.

[35] F. Rusek, D. Persson, B. K. Lau, *et al.*, "Scaling up MIMO: Opportunities and challenges with very large arrays," *IEEE Signal Processing Magazine*, vol. 30, no. 1, pp. 40–60, 2013.

[36] O. Elijah, C. Y. Leow, T. A. Rahman, S. Nunoo, and S. Z. Iliya, "A comprehensive survey of pilot contamination in massive MIMO—5G system," *IEEE Communications Surveys Tutorials*, vol. 18, no. 2, pp. 905–923, 2016.

[37] R. R. Müller, L. Cottatellucci, and M. Vehkaperä, "Blind pilot decontamination," *IEEE Journal of Selected Topics in Signal Processing*, vol. 8, no. 5, pp. 773–786, 2014.

[38] H. Xie, F. Gao, S. Zhang, and S. Jin, "A unified transmission strategy for TDD/FDD massive MIMO systems with spatial basis expansion model," *IEEE Transactions on Vehicular Technology*, vol. 66, no. 4, pp. 3170–3184, 2017.

[39] H. Xie, F. Gao, S. Zhang, and S. Jin, "A unified transmission strategy for TDD/FDD massive MIMO systems with spatial basis expansion model," *IEEE Transactions on Vehicular Technology*, vol. 66, no. 4, pp. 3170–3184, 2017.

[40] Y. Pei, T.-H. Pham, and Y.-C. Liang, "How many RF chains are optimal for large-scale MIMO systems when circuit power is considered?" In *2012 IEEE Global Communications Conference (GLOBECOM)*, 2012, pp. 3868–3873.

[41] H. Ochiai and H. Imai, "On the distribution of the peak-to-average power ratio in OFDM signals," *IEEE Transactions on Communications*, vol. 49, no. 2, pp. 282–289, 2001.

[42] F. H. Raab, P. Asbeck, S. Cripps, *et al.*, "RF and microwave power amplifier and transmitter technologies - part 1," *High Frequency Electronics*, vol. 2, no. 3, pp. 22–36, May 2003.

[43] S. C. Cripps, *RF power amplifiers for wireless communications* (2nd ed.). Artech House Publishers, 2006.

[44] V. Vorapipat, "Active load modulation for high efficiency RF transmitters," Ph.D. dissertation, University of California San Diego, 2018.

[45] C. K. Musoloff, "Wideband active load modulation in RF power amplifiers," Ph.D. dissertation, Friedrich-Alexander University Erlangen-Nürnberg, 2019.

[46] Y.-h. Xu, J.-Y. Oh, Z.-h. Sun, and M.-S. Lim, "A novel method for PAPR reduction of the OFDM signal using nonlinear scaling and FM," *Frontiers of Information Technology & Electronic Engineering*, vol. 20, pp. 1587–1594, 2019.

[47] T. Jiang and Y. Wu, "An overview: Peak-to-average power ratio reduction techniques for OFDM signals," *IEEE Transactions on Broadcasting*, vol. 54, no. 2, pp. 257–268, 2008.

[48] S. H. Han and J. H. Lee, "An overview of peak-to-average power ratio reduction techniques for multicarrier transmission," *IEEE Wireless Communications*, vol. 12, no. 2, pp. 56–65, 2005.

[49] Y. Rahmatallah and S. Mohan, "Peak-to-average power ratio reduction in OFDM systems: A survey and taxonomy," *IEEE Communications Surveys Tutorials*, vol. 15, no. 4, pp. 1567–1592, 2013.

[50] F. H. Raab, "High-efficiency linear amplification by dynamic load modulation," *IEEE MTT-S International Microwave Symposium Digest, 2003*, vol. 3, pp. 1717–1720, 2003.

[51] A. S. Tehrani, H. M. Nemati, H. Cao, T. Eriksson, and C. Fager, "Dynamic load modulation of high power amplifiers with varactor-based matching networks," *IEEE MTT-S International Microwave Symposium Digest*, pp. 1537–1540, 2009.

[52] H. M. Nemati, C. Fager, U. Gustavsson, R. Jos, and H. Zirath, "Design of varactor-based tunable matching networks for dynamic load modulation of high power amplifiers," *IEEE Trans. Microw. Theory Techn.*, vol. 57, no. 5, pp. 1110–1118, 2009.

[53] C. M. Andersson, M. Özen, D. Gustafsson, *et al.*, "A packaged 86 W GaN transmitter with SiC varactor-based dynamic load modulation," *2013 European Microwave Conference*, pp. 283–286, 2013.

[54] F. Kasem, R. Winter, R. Feghhi, K. Rambabu, and W. A. Krzymień, "Design of a low-cost low-profile energy efficient 64-QAM load modulator," *IEEE Transactions on Microwave Theory and Techniques*, vol. 70, no. 4, pp. 2246–2257, 2022.

[55] A. Kalis, A. G. Kanatas, and C. B. Papadias, "A novel approach to MIMO transmission using a single RF front end," *IEEE Journal on Selected Areas in Communications*, vol. 26, no. 6, pp. 972–980, 2008.

[56] T. Ohira and K. Gyoda, "Electronically steerable passive array radiator antennas for low-cost analog adaptive beamforming," *In Proceedings 2000 of IEEE International Conference on Phased Array Systems and Technology (Cat. No.00TH8510)*, pp. 101–104, 2000.

[57] B. Han, V. I. Barousis, C. B. Papadias, A. Kalis, and R. Prasad, "MIMO over ESPAR with 16-QAM modulation," *IEEE Wireless Communications Letters*, vol. 2, no. 6, pp. 687–690, 2013.

[58] A. Kalis, A. G. Kanatas, and C. B. Constantinos, *Parasitic antenna arrays for wireless MIMO systems*. Springer, New York, NY, 2014.

[59] B. Schaer, K. Rambabu, J. Bornemann, and R. Vahldieck, "Design of reactive parasitic elements in electronic beam steering arrays," *IEEE Transactions on Antennas and Propagation*, vol. 53, no. 6, pp. 1998–2003, 2005.

[60] O. N. Alrabadi, C. B. Papadias, A. Kalis, and R. Prasad, "A universal encoding scheme for MIMO transmission using a single active element for PSK modulation schemes," *IEEE Transactions on Wireless Communications*, vol. 8, no. 10, pp. 5133–5142, 2009.

[61] O. N. Alrabadi, J. Perruisseau-Carrier, and A. Kalis, "MIMO transmission using a single RF source: Theory and antenna design," *IEEE Transactions on Antennas and Propagation*, vol. 60, no. 2, pp. 654–664, 2012.

[62] B. Han, V. I. Barousis, A. Kalis, C. B. Papadias, A. G. Kanatas, and R. Prasad, "A single RF MIMO loading network for high-order modulation schemes," *International Journal of Antennas and Propagation*, vol. 2014, pp. 1–10, Jul. 2014.

[63] V. I. Barousis and C. B. Papadias, "Arbitrary precoding with single-fed parasitic arrays: Closed-form expressions and design guidelines," *IEEE Wireless Communications Letters*, vol. 3, no. 2, pp. 229–232, 2014.

[64] O. N. Alrabadi, C. Divarathne, P. Tragas, *et al.*, "Spatial multiplexing with a single radio: Proof-of-concept experiments in an indoor environment with a 2.6-GHz prototype," *IEEE Communications Letters*, vol. 15, no. 2, pp. 178–180, 2011.

[65] M. Yousefbeiki and J.Perruisseau-Carrier, "Towards compact and frequency-tunable antenna solutions for MIMO transmission with a single RF chain," *IEEE Transactions on Antennas and Propagation*, vol. 62, no. 3, pp. 1065–1073, 2014.

[66] S. Hong and K. Oh, "A comparison of ESPAR-MIMO and LMA-MIMO for single-RF transmission of spatially multiplexed QAM signals," in *2017 IEEE International Conference on Consumer Electronics (ICCE)*, 2017, pp. 133–134.

[67] J. Östh, Owais, M. Karlsson, A. Serban, and S. Gong, "Schottky diode as high-speed variable impedance load in six-port modulators," *IEEE International Conference on Ultra-Wideband (ICUWB)*, pp. 68–71, 2011.

[68] A. Serban, J. Östh, O. Owais, *et al.*, "Six-port transceiver for 6–9 GHz ultra-wideband systems," *Microwave and Optical Technology Letters*, vol. 52, no. 3, pp. 740–746, 2010.

[69] B. Luo and M. Y. Chia, "Performance analysis of serial and parallel six-port modulators," *IEEE Trans. Microw. Theory Techn*, vol. 56, no. 9, pp. 2062–2068, 2008.

[70] B. Luo and M. Y. W. Chia, "Direct 16-QAM six-port modulator," *Electronics Letters*, vol. 44, no. 15, pp. 910–911, 2008.

[71] Y. Zhao, C. Viereck, J. F. Frigon, R. G. Bosisio, and K. Wu, "Direct quadrature phase shift keying modulator using six-port technology," *Electronics Letters*, vol. 41, no. 21, pp. 1180–1181, 2005.

[72] J. Östh, M. Karlsson, A. Serban, and S. Gong, "M-QAM six-port modulator using only binary baseband data, electrical or optical," *IEEE Trans. Microw. Theory Techn.*, vol. 61, no. 6, pp. 2506–2513, 2013.

[73] C. Sánchez-Pérez, J. de Mingo, P. L. Carro, and P. García-Dúcar, "Design and applications of a 300–800 MHz tunable matching network," *IEEE Journal on Emerging and Selected Topics in Circuits and Systems*, vol. 3, no. 4, pp. 531–540, 2013.

[74] M. A. Sedaghat, V. I. Barousis, R. R. Müller, and C. B. Papadias, "Load modulated arrays: A low-complexity antenna," *IEEE Communications Magazine*, vol. 54, no. 3, pp. 46–52, 2016.

[75] R. R. Müller, M. A. Sedaghat, and G. Fischer, "Load modulated massive MIMO," *2014 IEEE Global Conference on Signal and Information Processing (GlobalSIP)*, pp. 622–626, 2014.

[76] V. I. Barousis, M. A. Sedeghat, R. R. Müller, and C. B. Papadias, "Massive antenna arrays with low front-end hardware complexity: An enabling technology for the emerging small cell and distributed network architectures," *arXiv:1407.7733*, 2014.

[77] M. A. Sedaghat, R. R. Mueller, R. R. Mueller, and G. Fischer, "A novel single-RF transmitter for massive MIMO," *WSA 2014; 18th International ITG Workshop on Smart Antennas*, pp. 1–8, 2014.

[78] M. A. Sedaghat, R. R. Mueller, G. Fischer, and A. Ali, "Discrete load-modulated single-RF MIMO transmitters," *Proc. 20th International ITG Workshop on Smart Antennas (WSA)*, pp. 1–7, Mar. 2016.

[79] S. Bhat and A. Chockalingam, "Random phase modulation in load modulated arrays," in *2017 IEEE 28th Annual International Symposium on Personal, Indoor, and Mobile Radio Communications (PIMRC)*, 2017, pp. 1–7.

[80] S. Bhat and A. Chockalingam, "MCMC sampling based signal detection in multiuser load modulated arrays," in *2018 IEEE 87th Vehicular Technology Conference (VTC Spring)*, 2018, pp. 1–5.

[81] S. Bhat and A. Chockalingam, "LSE precoder for load modulated arrays with channel modulation," *IEEE Wireless Communications Letters*, vol. 9, no. 8, pp. 1295–1299, 2020.

[82] S. Bhat and A. Chockalingam, "Detection of load-modulated multiuser MIMO signals," *IEEE Wireless Communications Letters*, vol. 7, no. 2, pp. 266–269, 2018.

[83] S. Bhat and A. Chockalingam, "Load modulated arrays using channel modulation with RF mirrors," in *2019 IEEE 89th Vehicular Technology Conference (VTC2019-Spring)*, 2019, pp. 1–5.

[84] D. A. Frickey, "Conversions between S, Z, Y, H, ABCD, and T parameters which are valid for complex source and load impedances," *IEEE Trans. Microw. Theory Techn.*, vol. 42, no. 2, pp. 205–211, 1994.

[85] R. Storn and K. Price, "Differential evolution – a simple and efficient heuristic for global optimization over continuous spaces," *Journal of Global Optimization*, vol. 11, pp. 341–395, Dec. 1997.

[86] A. K. Qin, V. L. Huang, and P. N. Suganthan, "Differential evolution algorithm with strategy adaptation for global numerical optimization," *IEEE Transactions on Evolutionary Computation*, vol. 13, no. 2, pp. 398–417, 2009.

[87] D. Pozar, *Microwave Engineering, 4th Edition*. Wiley, 2011.

[88] E. Wilkinson, "An n-way hybrid power divider," *IRE Transactions on Microwave Theory and Techniques*, vol. 8, no. 1, pp. 116–118, 1960.